2018

Fluid Dynamics Modeling and Sound Analysis of a Bileaflet Mechanical Heart Valve

Fardin Khalili
University of Central Florida

FLUID DYNAMICS MODELING AND SOUND ANALYSIS OF A BILEAFLET MECHANICAL HEART VALVE

by

FARDIN KHALILI
B.S Islamic Azad University of Mashhad, 2012
M.S Northern Illinois University, 2014

A dissertation submitted in partial fulfillment of the requirements
for the degree of Doctor of Philosophy
in the Department of Mechanical and Aerospace Engineering
in the College of Engineering and Computer Science
at the University of Central Florida
Orlando, Florida

Spring Term

2018

Major Professor: Hansen A. Mansy

ABSTRACT

Cardiovascular disease (CVD) is one of the main causes of death in the world. Some CVD involve severe heart valve disease that require valve replacement. There are more than 300,000 heart valves implanted worldwide, and about 85,000 heart valve replacements in the US. Approximately half of these valves are mechanical. Artificial valves may dysfunction leading to adverse hemodynamic conditions. Understanding the normal and abnormal valve function is important as it help improve valve designs. Modeling of heart valve hemodynamics using computational fluid dynamics (CFD) provides a comprehensive analysis of flow, which can potentially help explain clinical observations and support therapeutic decision-making. This detailed information might not be accessible with in-vivo measurements. On the other hand, finite element analysis (FEA), is an efficient way to analyze the interactions of blood flow with blood vessel and tissue layers. In this project both CFD and FEA simulations were performed to investigate the flow-induced sound generation and propagation of sound waves through a tissue-like material. This method is based on mapping the transient pressure (force) fluctuations on the vessel wall and solving for the structural vibrations in the frequency domain. These vibrations would then be detected as sound on the epidermal surface. Advantages of the methods used in the current study include: (a) capability of providing accurate solution with a faster solution time; (b) inclusion of the fluid–structure interaction between blood flow and the arterial wall; and (c) accurately capturing some of the spectral features of the velocity fluctuation measured over the epidermal surface.

KEYWORDS: Bileaflet mechanical heart valve; computational fluid dynamics (CFD); finite element methods (FEM); Turbulence; cardiovascular disease; hemodynamics; hemoacoustics.

I dedicate this dissertation to my better half, my brilliant and appreciably loving fiance, Afsaneh Tasavvori whose unconditional encouragement and support made it possible for me to complete this work.

ACKNOWLEDGMENTS

I am mostly grateful to Dr. Hansen Mansy, my supervisor, who has introduced me to field of bioacoustics engineering. I would also like to thank Dr. Alain Kassab, Ricardo Zaurin, and Dr. Robert L. Steward, Jr., who have supported me by their valuable feedback.

I am also thankful to all my colleagues in biomedical acoustics research lab (BARL), especially Peshala Gamage and Andrew Spiewak who helped me a lot along this path, and Amirtaha Taebi and Khurshid Azad who have been great friends to me.

TABLE OF CONTENTS

LIST OF FIGURES ix

LIST OF TABLES xv

LIST OF ABBREVIATIONS xvi

CHAPTER 1: INTRODUCTION 1

1.1 Brief History of Heart Valves 1

1.2 Understanding of Blood Flow and Complications 2

1.3 Hemoacoustic Analysis 6

1.4 Research Objective 8

CHAPTER 2: METHODS 11

2.1 Flow Modelling 12

2.1.1 Reynolds-Averaged Navier-Stokes (RANS) Models 13

2.1.1.1 RANS k-ω Model 14

2.1.1.2 RANS shear stress transport (SST) k-ω model 15

2.1.1.3 RANS Reynolds Stress Transport (RST) model 16

2.1.2 Large Eddy Simulation (LES) 17

2.1.3 Detached Eddy Simulation (DES) 20

2.2 Verification of Turbulence Models 21

2.2.1 CFD Modelling 21

2.2.2 Mesh/Grid Configuration 22

2.2.3 Experimental Setup and Procedure 23

2.2.4 Results and Discussions 26

2.2.5 Limitation 36

2.2.6 Conclusions 37
2.3 Development of a Programmable Pulsatile Heart Pump 37
2.3.1 Experimental Setup 38
2.3.2 Flow Waveform Modeling 40
2.3.3 Limitations 43
2.4 Modelling of Flow-Generated Sound 44
2.4.1 Direct Method 45
2.4.2 Hybrid Method 46
CHAPTER 3: HEMODYNAMICS OF A BILEAFLET MECHANICAL HEART VALVE 47
3.1 Valve Modeling 47
3.2 Fluid Dynamics of the Bileaflet Mechanical Heart Valves 49
3.3 Heart Valve Dysfunction (Patient-Specific Condition I) 54
3.3.1 Simulation Setup 54
3.3.2 Numerical Uncertainty 56
3.3.3 Validation 58
3.3.4 Velocity and Turbulent Kinetic Energy 60
3.3.5 Streamline and Vorticity 61
3.3.6 Wall Shear Stresses 63
3.3.7 Helicity 66
3.3.8 Maximum Velocity and Pressure Drop 67
3.3.9 Blood Complications 68
3.3.10 Pressure Distribution 71
3.3.11 Applied Forces and Moments on Leaflets 72
3.3.12 Conclusion 74

3.4 Different Geometry of Aortic Sinuses (Patient-Specific Condition II) 75
3.4.1 Velocity Distribution 78
3.4.2 Wall Shear Stresses 79
3.4.3 Principal Shear Stresses 80
3.4.4 Conclusion 82
3.5 Limitations 82
CHAPTER 4: SOUND ANALYSIS 83
4.1 Validation of Hydro-Vibroacoustics Approach 85
4.1.1 Geometry 85
4.1.2 Hemodynamics 86
4.1.3 Acoustics 87
4.1.4 Instantaneous Vorticity 89
4.1.5 Sound Analysis 91
4.1.6 Advantages and Limitations 92
4.1.7 Conclusion 93
4.2 Future Work 93
CHAPTER 5: SUMMARY 96
APPENDIX I: PUBLICATIONS 97
APPENDIX II: SIMPLIFIED BERNOULLI EQUATION 100
APPENDIX III: ARDUINO CODE 103
REFERENCES 106

LIST OF FIGURES

Figure 1-1 Three-dimensional model of a BMHV at fully-opened position, implanted at aortic sinuses. Arrows show the three jets which form through the orifices. 3

Figure 2-1 Schematic of the stenosed artery (pipe with constriction). Points P1 to P7 denote velocity measurement locations in the tube. 22

Figure 2-2 Polyhedral mesh generation with prism layers and a refined mesh at and downstream of the constriction. 23

Figure 2-3 Grid independent analysis for the stenosed artery (pipe with constriction). 23

Figure 2-4: The operation procedure of a laser Doppler anemometry (LDA) unit [143]. 24

Figure 2-5 Laser Doppler anemometry (LDA) experiment setup for the stenosed artery (pipe with constriction). 24

Figure 2-6 Measured axial mean velocities along the centerline of the stenosed artery (pipe with constriction). 27

Figure 2-7 Comparison of experimental and computational results for axial mean velocities along the centerline of the stenosed artery (pipe with constriction) for different turbulence models. 28

Figure 2-8 Comparison of experimental and computational results for axial mean velocities at the outlet of the stenosed artery (pipe with constriction) for different turbulence models. 29

Figure 2-9 Axial mean velocity on the cross-sectional view of the stenosed artery (pipe with constriction) for different turbulence models. 30

Figure 2-10: Instantaneous vorticity on the cross-sectional view of the stenosed artery (pipe with constriction) for different turbulence models. 31

Figure 2-11 Instantaneous velocity fluctuations for LES Smagorinsky and dynamic Smagorinsky turbulence models and LDA measurements. .....**Error! Bookmark not defined.**

Figure 2-12 Mean axial velocity along the diameter of the stenosed artery (constricted pipe) at 5 cm and 7 cm downstream of the constriction for LES Smagorinsky and dynamic Smagorinsky turbulence models and LDA measurements. 33

Figure 2-13 RMS axial velocity fluctuation profiles along the diameter of the stenosed artery (constricted pipe) at 5 cm and 7 cm downstream of the constriction for LES Smagorinsky and dynamic Smagorinsky turbulence models and LDA measurements.....35

Figure 2-14: Distribution of axial velocity and streamlines (LES Dynamic Smagorinky Subgrid Scale) inside the tube with region classification.....36

Figure 2-15 (a) Pulsatile pump setup including the linear actuator and pump control box; (b) Explode view of the main devices. 39

Figure 2-16 Main pipe and the test section of the experimental setup. 40

Figure 2-17 (a) Blood velocity and displacement profiles through aortic valve; (b) Desired velocity and displacement for the linear actuator. 41

Figure 2-18 (a) Comparison of the actual and desired linear actuator movements. Dashed line shows the end of systole; (b) Difference between the actual and desired linear actuator movements till the end of systole.....42

Figure 2-19 Velocity waveform upstream of the heart valve 43

Figure 3-1 (a) A bileaflet mechanical heart valve modelled based on St. Jude Medical and Regent Medical heart valves [7,25]; (b) Front view of the aortic root sinuses similar to the geometry which was extracted from angiograms [57].....47

Figure 3-2 Heart valve hinge dimensions characterized by its butterfly shape; (a) Hinge recess and the gap in the hinge region; (b) St. Jude Regent Medical heart valve hinge design with smooth contours; (c) Simplified heart valve hinge design with less smooth contours. 48

Figure 3-3 Dynamic fluid body interaction (DFBI) and overset mesh around the moving leaflets, (a) 3D prospective view; (b) cross-sectional view.....50

Figure 3-4 Mass flow rate and leaflet opening angle for a cardiac cycle of 0.860 s. 51

Figure 3-5 Valve leaflet opening phase during the systole (0-0.3 s). 52

Figure 3-6 Valve leaflet closing phase during the diastole.....53

Figure 3-7 (a) High-velocity blood Regurgitation through the gaps between the leaflets and the valve housing; (b) Leakage driven through the narrow hinge regions by a large cross-valvular pressure gradient which produces turbulent shear stresses with high exposure time. 54

Figure 3-8 (a) Degrees of bottom leaflet dysfunction; and (b) Sign conventions for forces acting on the leaflets. 55

Figure 3-9 High quality polyhedral mesh generated (a) close to the wall and leaflet surfaces and, (b) in the flow domain.....56

Figure 3-10 (a) Velocity profile at the entrance of the aortic sinuses for different grid solution; (b) Fine-grid solution with discretization error bars. 57

Figure 3-11 (a) Normalized velocity profiles at 7 mm downstream of the valve (at the peak systole) in the current study compared to previous experimental [158] and computational [90] studies. More agreement can be seen between the current and the experimental study; (b) Normalized velocity profiles at the trailing edge of the leaflets (105 ms after the peak

systole) in the current study compared to previous experimental [88] and computational [31] studies.....59

Figure 3-12 Velocity and turbulent kinetic energy at 90 ms for different degrees of lower leaflet dysfunction. There was a general trend of increased maximum velocity and TKE with increased dysfunction. (Note that the scale for TKE increased with dysfunction).....61

Figure 3-13 Flow field around the valve: (a) Streamlines; (b) Vorticity.....63

Figure 3-14 Wall shear stress distribution on aortic sinuses at the peak systolic velocity and different degrees of dysfunction: a) 0%; b) 25%; c) 50%; d) 75%; and e) 100%. Highest wall sheer stresses occurred around 50% dysfunction.....64

Figure 3-15 Wall shear stresses on valve frame; (a) Newtonian flow; (b) non-Newtonian flow. (1: 0%; 2: 25%; 3: 50%; 4:75% and 5: 100% dysfunction).....65

Figure 3-16 Helicity isosurfaces (isovalue = 414m/s2) at different times and dysfunctions. A general increase in helicity was observed with dysfunction.....67

Figure 3-17 Comparison of the current study results with available data from a previous computational study (Smadi et al. 2010 [3]): (a) Maximum velocity at the entrance of the aortic sinuses, and (b) maximum pressure gradients across the valve computed from simplified Bernoulli equation. Both quantities continuously increased with dysfunction. While the trends were similar, differences may be due to the geometrical variations and the fact that the current study performed 3D compared to 2D simulation in [3].....68

Figure 3-18 Principal shear stresses for different levels of dysfunction at the peak systole. Elevated levels of principal stresses were observed with dysfunction, which increase blood damage risks. Published cutoff stress value for damage is above 400 N/m2 [41].....70

Figure 3-19 a) 0%; b) 25%; c) 50%; d) 75%; and e) 100%. For dysfunction ≥ 75%, a region of high pressure developed at the bottom surface of the functional leaflet upstream of the hinge, which would generate moments that tend to keep that leaflet open. 71

Figure 3-20 Net pressure and shear forces on leaflets: a) F_p on top leaflet; b) F_p on bottom leaflet; c) F_τ on top leaflet; and d) F_τ on bottom leaflet. The sign of some forces started to reverse at high levels of dysfunction. 73

Figure 3-21 Net moments on: a) Top leaflet, and b) Bottom leaflet. The moments tended to be in the directions of leaflet opening. All moments increased with dysfunction. In most cases of dysfunction, the moments on the dysfunctional leaflet were higher (note the different scale for the dysfunctional leaflet). 73

Figure 3-22 (a) Bileaflet mechanical heart valve; (b) Cross-sectional view of aortic root sinuses. 77

Figure 3-23 Velocity distribution through a bileaflet mechanical heart valve for different geometries of aortic root sinuses: (a) normal sinuses; (b) severe insufficiency; (c) severe stenosis. 79

Figure 3-24 Wall shear stress distribution on different geometries of aortic root sinuses: (a) normal sinuses; (b) severe insufficiency; (c) severe stenosis. 81

Figure 3-25 Turbulent shear stresses (TSS) through a bileaflet mechanical heart valve for different geometries of aortic root sinuses: (a) normal sinuses; (b) severe insufficiency; (c) severe stenosis. 81

Figure 4-1 Schematic of the constricted channel model and acoustic domain; D arterial diameter, h_w arterial wall thickness; h_t tissue layer thickness. 85

Figure 4-2 Non-dimensional pulsatile pressure drop between inlet and outlet. 86

Figure 4-3 Hydro-vibroacoustic Simulation methodology of the current study using ANSYS Fluent and FEA Harmonic Response. 88

Figure 4-4 Time evolution of vorticity field; 0/8T maximum flow rate, 4/8T minimum flow rate phase. (The vorticity contours shown were normalized by time scale D/U_{max}).....90

Figure 4-5 Frequency spectrum of vertical velocity fluctuations (v′) on the epidermal surface monitored 6D downstream from the center of the stenosis. The frequency was (y-axis) was normalized (from 0.1 to 10). 91

Figure 4-6 (a) Cross-sectional view of the computational model; Mapped pressure forces on the top wall and stress distribution on the tissue at (b) 125 Hz; (c) 250 Hz. 94

Figure 4-7 Stress distribution through the tissue layer at the fully-closed position where the top leaflet hits the valve housing.....95

LIST OF TABLES

Table 2-1: Mean and RMS values of measured velocities 27

Table 2-2 Mean axial velocity (m/s) at 5 cm and 7 cm downstream of the constriction for LES Smagorinsky and dynamic Smagorinsky turbulence models and LDA measurements 34

Table 2-3 Mean axial velocity (m/s) at 5 cm and 7 cm downstream of the constriction for LES Smagorinsky and dynamic Smagorinsky turbulence models and LDA measurements 35

Table 3-1 Calculation of discretization error 56

Table 3-2 Averaged and maximum wall shear stresses (WSSs) on the valve frame, location of the highest WSSs in the flow domain and the maximum helicity in the aortic sinuses at peak systole. 66

Table 3-3 Maximum Principal Shear Stresses 71

Table 3-4 Parameters for the geometrical characterization of the aortic root.....77

LIST OF ABBREVIATIONS

BMHV	Bileaflet mechanical heart valve
CAA	Computational aeroacoustics
CFD	Computational fluid dynamics
CGNS	CFD general notation system
CVDs	Cardiovascular diseases
DES	Detached Eddy Simulation
ECHO	Echocardiography
EOA	Effective orifice area
FEA	Finite element analysis
FEM	Finite element method
FFT	Fast Fourier Transformation
GCI_{fine}	Fine-grid convergence index
HRA	Harmonic response analysis
LDV	Laser Doppler velocimetry
LES	Large Eddy Simulation
LVDT	Linear variable displacement transducer
M	Mach number
MHV	Mechanical heart valve
PCG	Phonocardiography
RANS	Reynolds-Averaged Navier-Stokes
Re	Reynolds number
RMS	Root-mean-square
RST	Reynolds Stress Transport
SGS	Subgrid scale
SJM	St. Jude Medical
SST	Shear stress transport
St	Strouhal number
TEE	Transesophageal echocardiography
TKE	Turbulent kinetic energy
TPG_{max}	Maximum transvalvular pressure gradient
TSS	Turbulent shear stress
URANS	Unsteady Reynolds-Averaged Navier-Stokes
WSS	Wall shear stresses

CHAPTER 1: INTRODUCTION

The heart is a vital impellent of cardiovascular system and responsible for body viability. Heart valves (Mitral, Pulmonary, Aortic and Tricuspid valves), are important components of the heart, operate to keep the unidirectional blood flow in systemic and pulmonary circulation systems. Normal performance of the four heart valves indicates a healthy pathophysiological functionality of the cardiovascular system; however, they can be subject to valve malfunction. Cardiovascular diseases (CVDs) are a leading cause of death in the world [1]. There are, annually, more than 300,000 heart valves implanted worldwide [2], and about 85,000 heart valve replacements in the US, while approximately half of them are mechanical valves [3]. Hence, understanding of normal cardiac functions and diseases is vital for diagnostics and treatments. Computational fluid dynamics (CFD) has the potential to serve as decision-making aid and can support, enhance and explain clinical observations by providing detailed information of the blood flow. On the other hand, finite element method (FEM), also called finite element analysis (FEA), is an efficient way to analyze the interactions of blood flow with blood vessel and tissue layers. The detailed information that can be provided by CFD and FEA might not be accessible with in-vivo measurements [4].

1.1 Brief History of Heart Valves

The necessity of the prosthetic heart valves was long noticed, but seemed an impossible accomplishment before Dr. Charles Hufnagel [5], in 1952, clinically presented a mechanical ball valve that he implanted into a descending thoracic aorta for treatment of aortic valvular failure. Improvement of both Bioprosthetic and mechanical heart valves requires the union of two factors, which are: (a) biologically compatible materials, and (b) hemologically tolerant designs. Lasting

valve function would not be achieved without these features [6]. Mechanical heart valves (MHV), in particular, have gone through several design enhancements and proven durable with desirable hemodynamics [7]. Among different types of MHVs, bileaflet mechanical heart valve (BMHV) is the most common valve design. In 1977, Dr. Demetre M. Nicoloff [7] implanted the first St. Jude Medical (SJM) valve, which is, now, one of the practicable and durable BMHVs with a low incident rates of 0.2-6% patients/year [3]. In addition, More than one million of SJM valves have been implanted worldwide with virtually no related body destruction of the leaflets or housings [8]. Accordingly, this valve represents a remarkable progress in clinically existing heart valves and the most widely used prosthetic one [9]. In spite of the fact that the ideal hemodynamic performance of prosthetic heart valves has not yet achieved, patients with implanted valves attain a relatively normal life [10,11].

1.2 Understanding of Blood Flow and Complications

The heart cycle of the left ventricle can be divided into systole and diastole. At the beginning of the systolic stage, when the ventricular pressure rises above the aortic pressure, the aortic valve opens, and the blood is ejected from the left ventricle into the aorta. Afterwards, the ventricular pressure declines slightly under the aortic pressure. At the very end of systole, a small amount of aortic backflow can be observed before the valve closes at the beginning of diastole [4].

Figure 1-1 is a schematic representation of the valve showing the leaflets, valve ring (also called housing), the hinge regions, and the main three orifice jets. During the fully opening period of the valve operation, a BMHV has three orifices (superior, central and inferior orifices), which is typically from 60 ms to 250 ms of a cardiac cycle [12]. As the blood flows through the valve, three high-velocity jets form at the orifices and can result in high shear stress levels [13,14].

Analysis of blood flow around BMHV may help identify flow patterns with higher shear and normal stresses [15,16], which may therefore help improve mechanical heart valve designs.

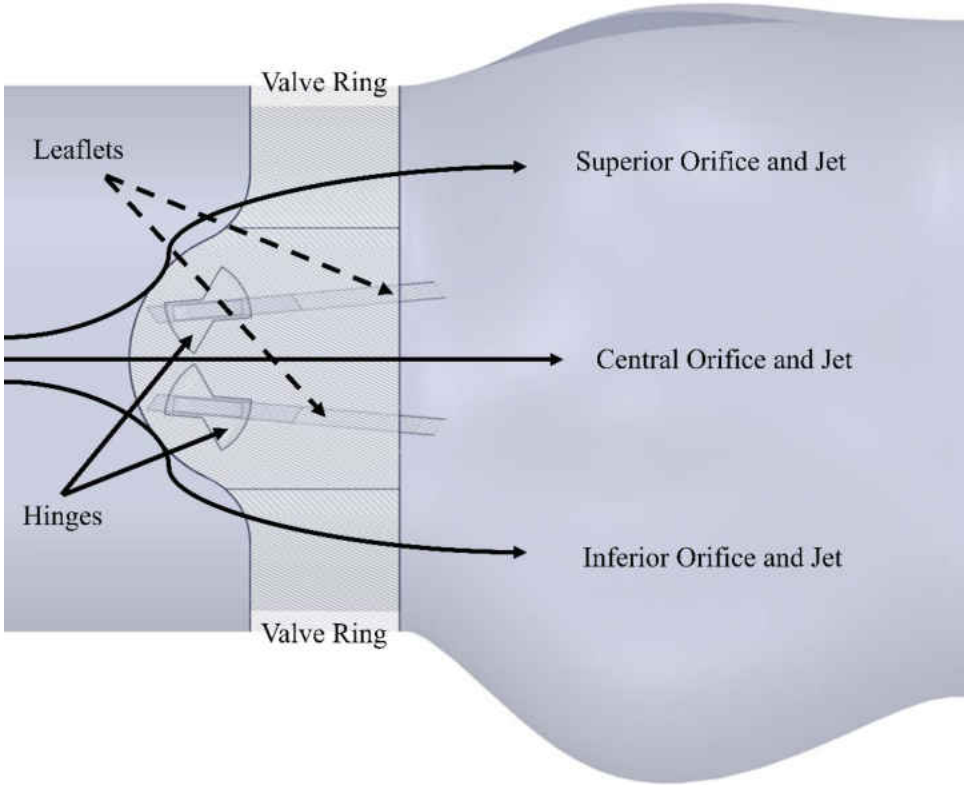

Figure 1-1 Three-dimensional model of a BMHV at fully-opened position, implanted at aortic sinuses. Arrows show the three jets which form through the orifices.

The leaflets of the modelled BMHV (based on SJM Regent™ Mechanical Valve [17,18]) span 54.2° from its fully-closed position to its fully-open position [19]. It should be noted that, in this study, the fully-open leaflets make an angle of 5° with the main flow direction. The effect of different leaflet opening angles on the blood flow was investigated using a two-dimensional experimental model of the valve for a steady laminar flow [20,21]. This study suggested that the opening angle can highly affect the flow downstream of BMHV and that opening angles > 80 degrees would be more effective in reducing flow resistance and vortical structures. Shipkowitz et. Al. [22] exploited PIV, video analysis, and CFD to evaluate two commercially available BMHVs. They found that leaflet position, pivot location and orifice size affect pressure

distribution through the leaflets and, thereby, affecting the opening angle. Bluestein et. al. [23] investigated the motion of the leaflets for the last few degrees of valve closure in cardiac cycle and found that the velocity of the leaflets in the closing phase is another key parameter affecting the blood flow and heart valve cavitation.

Experimental studies were performed using different measurement methods to help in better understanding of the flow around BMHVs [24,25]. Some of these methods are echocardiography [26], particle image velocimetry (PIV) [27], laser Doppler velocimetry (LDV) [28], and hot film anemometry (HFA) [24,29]. While experimental studies have provided a wealth of information, practical limitations of the measurement methods often make it time-consuming or impractical to extract detailed information and perform parametric studies. Computational fluid dynamic (CFD) offers a complementary approach that is capable to overcome some of these potential limitations. When compared with other mechanical heart valves bileaflet mechanical heart valves exhibit superior bulk flow hemodynamics, a larger orifice area, a lower transvalvular pressure drop, and fewer regions of flow stasis [7,30]. Nevertheless, implantation of bileaflet mechanical heart valves may cause major complications including hemolysis, platelet activation, and thromboembolic events [31,32]. These complications may raise due to the difference between blood flow pattern through mechanical and human natural heart valves. Analysis of blood flow characteristics through a BMHV (such as velocity, vortex formation, and turbulent stresses, especially around the valve hinge regions [33,34]) can help identify conditions that may increase the risk of blood cell damage [16,35]. High and low shear stresses can have influence on blood components; for example, they can damage red blood cells and activate platelets leading to thrombus formation on the valve and thromboembolism, respectively [36]. Lethal and sublethal damages of red cells can occur with turbulent shear stresses as low as 150 and 50 $N.m^{-2}$, respectively [37,38]. These levels can be

significantly lower (1-10 $N.m^{-2}$) in the presence of foreign surfaces such as valve prostheses [39,40]. Reported critical turbulent shear stress levels can also be as high as 400 $N.m^{-2}$ [41] and 800 $N.m^{-2}$ [42]. In addition, platelet activation can occur for turbulent shear stresses in the range of 10-50 $N.m^{-2}$ [36,37]. Studies also showed that high turbulent shear stress levels at the valve hinges and downstream of the valve can lead to thrombus formation and the leaflets' motion restriction [14,43]. This, in turn, may lead to a life-threatening dysfunction of one or both leaflets of BMHVs [44]. McQueen and Peskin [45] investigated a mitral bileaflet valve design using CFD and suggested that valves with curved leaflets reduces the peak velocities in the orifices.

Dysfunction of the heart valves is a serious and potentially fatal complication; hence, analysis of flow dynamics and the resulting turbulence [46,47] and sounds [48,49] has been an active area of research. On the other hand, structural failures of mechanical heart valves implanted in hearts, such as restriction of leaflets' motion [50,51] in addition to failures due to cavitation or calcification [52] were reported as the mechanisms that lead to heart valve dysfunction. Several studies investigated the etiology of insidious prosthetic valve dysfunction. Previous studies [53–55] showed that the structural failure of mechanical heart valves is usually related to thrombus formation and tissue overgrowth. These complications, in overall, mostly occurred at the valve ring and hinge area and impaired the movement of one or both leaflets. Montorsi et al. [56] investigated the role of fluoroscopy to predict the success of thrombolysis in patients with mitral prosthetic valve thrombosis. They found that 35% of patients had normal Doppler study despite fluoroscopy showing significant restriction in one of the leaflets. They also concluded that the distinction between blocked and hypomobile leaflet is vital. Pibarot et al. [54] showed that transesophageal echocardiography (TEE) can provide improved image quality and thereby better detection of valve complications which reduces leaflet mobility. On the other hand, the peak

velocity and the position of the maximal velocity at valve orifices were determined as the best predictors of dysfunctional valve leaflets [3,57]. Prompt recognition of valve dysfunction allows early treatment [54]. For example, blocked leaflets could be fully recovered when valve thrombosis is detected early [56]. Fortunately, many of these complications can be prevented or minimized with careful medical management and periodic monitoring of valve function. Also, analysis of blood flow around the valve and identification of flow disturbance may therefore direct to improvements in mechanical heart valves which result in blood cell damage reduction and platelet activation, and hence decrease the anticoagulation therapy level required by the patient.

1.3 Hemoacoustic Analysis

Cardiac Echocardiography employs Doppler ultrasound for the assessment of intracardiac flows, and phonocardiography employs recording and analysis of heart sounds at the skin surface [48,58–60]. Manual auscultation has been used for many decades for cardiovascular disease diagnostics [61–64]. Blood flows associated with many abnormal cardiovascular conditions generate characteristic sounds called “murmurs” or “bruits” [65]. These sounds can be measured on the skin surface using a stethoscope [66,67]. However, the physical mechanisms that generate these sounds, as well as the physics of sound transmission through the body, are still not fully understood [68]. It has long been accepted that the source of most murmurs are disturbances in blood flow caused by obstruction in the vessels. Modeling of these structures would be helpful when more detailed flow behavior such as in studies of acoustic sources is needed [69]. Hence, there have been many previous studies on the dynamics of flows through stenosed or partially obstructed vessels [70–72]. In addition, there have been a few modeling studies employing finite-element [73] or boundary-element based methods [74] on wave propagation in tissue-like materials, but these studies were conducted for highly simplified cases with prescribed sources. In

order to more fully understand the relationship between cause (disease) and effect (sound measured on the skin surface), the hemodynamics associated with the murmur must be investigated concurrently, while considering the complete elastic wave dynamics including compression and shear waves propagation, and wave scattering and dissipation. The direct simulation of blood flow-induced sounds has the potential to provide an additional understanding of heart murmurs, and this forms the primary motivation for the present study. Similar investigations has been done in computational aeroacoustics (CAA) [75,76] and hydroacoustics fields [77,78].

Several studies were performed to understand the source and mechanism of the bruit generation. Bruns [65] argued that arterial bruits were generated by the 'nearly periodic fluctuation in the wake found downstream of any appropriate obstacle' and not by post-stenotic turbulence. Lees and Dewey [66] recorded the spectrum of actual bruit sounds (a technique called phonoangiography), and suggested a significant similarity between the bruit sound spectrum and the wall pressure spectrum of a fully developed turbulent pipe flow. Duncan [79] developed a relationship to estimate the residual lumen diameter of a stenosed area based on the break frequency observed in the measured bruit spectra. Fredberg [80] derived a theoretical model for the transfer function between wall pressure spectrum and sensed sound using the Green's function and a stochastic analysis of turbulent boundary layer. Wang et al. [81] modeled the sound generation in a stenosed coronary artery using an electrical network analog model, and Borisyuk [82] modeled the sound propagation through the tissues (thorax) theoretically for a simple cylindrical geometry. In a recent study, the blood flow-induced arterial ''bruits'' were computed directly using a hybrid approach wherein the hemodynamic flow field is solved by an immersed boundary, incompressible flow solver, and the sound generation is modeled based on the linearized compressible perturbation equations [68,83]. The transmission and propagation of the sound

through the surrounding biological tissues is also modeled with a simplified, linear structural wave equation.

Computational modeling offers a promising modality for exploring the physics of heart murmurs. Thus, virtual Echocardiography (ECHO) and Phonocardiography (PCG) can serve as a bridge between clinical data and computational hemodynamic results [84,85]. These virtual ECHO and PCG can be used for rapid validation of computational results by comparing to the actual cardiographic data, and furthermore, such comparisons will allow us to calibrate a given patient-specific, computational heart model.

1.4 Research Objective

The current computational study investigated the hemodynamic effects of mechanical heart valve leaflet dysfunction using 3-D valve geometry. Model improvements compared to previous studies include: a more realistic aortic sinuses geometry compared to [86,87], addition of the valve ring to the model compared to [88,89], and creation of a 3-D model instead of a 2-D model compared to [3,90,91].

The study quantified important hemodynamic characteristics (such as principle stresses) that are not measurable using standard diagnostic tools. This approach can provide a patient-specific tool for identification of adverse conditions that are associated with an increased risk of hemolysis and thrombus formation [36,37]. This information can provide a potentially more complete picture of the valve status and hence may be useful in clinical management of patients with dysfunctional valves. For example, the principal stresses increase with leaflet dysfunction was found to be initially slow, then significantly accelerate, suggesting a possible need for closer monitoring of the patients with > 50% of leaflet dysfunction. In addition, results identified locations of high velocities downstream of the valve. This knowledge may prove useful for choosing measurement

location of Doppler studies that are carried out to assess severity of velocity and pressure gradients, and hence valve dysfunction. Furthermore, new quantitative information about forces and moments acting on the leaflets were extracted. These forces can affect reaction forces and stresses at the hinges, where thrombus and clotting tend to form. When detached, the resulting free-floating clot can block arteries leading to serious consequences such as embolism and stroke [91].

On the other hand, we present a new computational method for investigating the flow-induced sound generation and propagation of these waves through a tissue-like material and simulate solid-induced sound transmission in surrounding tissue due to the contact of heart valve leaflets (solid-solid interaction). These analyses could be done using computational fluid dynamics in ANSYS Fluent [92], and finite element methods in ANSYS Transient Structural Analysis and Harmonic Response [92]. Blood flow in the vessel was simulated by solving the incompressible Navier–Stokes equations and propagation through the surrounding vessel wall and tissue is resolved with a "harmonic response" finite element analysis (FEA). The pressure fluctuations causing vibrations in the solid domain were investigated to resolve wave propagation and scattering accurately. The flow field inside the artery and the bruit sound signal at the epidermal surface were examined to delineate the source of the arterial bruit and the correlation between the bruit and the arterial wall pressure fluctuations. A new computational approach for simulating the blood flow-induced sound generation and propagation in a stenosed artery with one-sided constriction was investigated. This computational hemoacoustic method is based on mapping the transient pressure (force) fluctuations on the vessel wall and solving for the structural vibrations in frequency domain. These vibrations were detected as sound on the epidermal surface. The current method employs a two-step, one-way coupled approach for the sound generation in the flow domain and its propagation through the tissue layers. The results were validated by comparing with previous analytical and

computational solutions. It was found that the bruits (generated from the flow around the stenosis) are related primarily to the time-derivative of the integrated pressure force on the arterial wall downstream of the stenosis. Advantages of the methods used in the current study include: (a) capability of providing accurate solution with a faster solution time; (b) accurately capturing the break frequency of the velocity fluctuation measured on epidermal surface; (c) inclusion of the fluid–structure interaction between blood flow and the arterial wall.

CHAPTER 2: METHODS

Computational fluid dynamics (CFD) is a useful tool for prediction of turbulence in aerodynamic and biomedical applications. The choice of appropriate physics is the key to reaching accurate predictions of flow behavior. One of the most important and least understood aspects of flow is when the local Reynolds number of the turbulent flow is relatively low [93]. Effects of turbulence is of interest in various industrial [94–96] and biomedical [97–104] applications. Most fluid flows are characterized by irregularly fluctuating flow quantities that often occur at small scales and high frequencies. Hence, resolving these fluctuations in time and space requires excessive computational costs. Optimum modeling of these structures is of interest for the acoustic investigations including biomedical applications, which are active areas of research [48,105,106]. Some basic knowledge of turbulence and an understanding of how turbulence models are developed can help provide insight into choosing and applying these models to obtain reasonable engineering simulations of turbulent flows. Turbulence models from three different categories: Reynolds-Averaged Navier-Stokes (RANS) models and scale-resolving simulation (SRS) methods, namely, Large Eddy Simulation (LES) and Detached Eddy Simulation (DES), were included in the current study. RANS turbulence models (here, RANS SST k-ω and RANS Reynolds Stress models) solve for mean flow quantities where fluctuations are represented by ensemble averaging. On the other hand, LES simulates transitional flow with appropriate subgrid scale modeling, and was included here using dynamic and normal Smagorinsky subgrid scale formulations. In addition, DES hybrid models (here, DES SST k-ω model) incorporate LES modeling of free stream flow with unsteady RANS simulation of near wall flow and are therefore less computationally expensive than LES. The main concern about the initial form of DES model

was its inability to predict the behavior of the flow downstream of the separation region and improper simulation of laminar-turbulent transition [107,108]. In the last decade, significant developments in the DES modeling have resulted in improvements especially in solving the external flows in separation and strong circulation zones [109–111]. To highlight the main differences between these approaches, a brief description of each turbulence model used in the current study is below.

2.1 Flow Modelling

For the current application, flow can be considered as incompressible due to the low Mach number flow and it's also assumed that flow is isothermal due to negligible changes in temperature of the flow. Based on the above assumptions, the governing equations for the flow are presented as,

$$\frac{\partial u_i}{\partial x_i} = 0 \tag{2-1}$$

$$\rho \frac{\partial u_i}{\partial t} + \rho u_j \frac{\partial u_i}{\partial x_j} = -\frac{\partial p}{\partial x_i} + \mu \frac{\partial^2 u_i}{\partial x_j \partial x_j} \tag{2-2}$$

Here, Equations 2.1 and 2.2 represent the mass conservation (or continuity) and momentum conservation, respectively. Subscripts *i* and *j* denote the Cartesian tensor notations. In the above equations, *u*, *p* and *t* are the three-dimensional velocity vector, static pressure and time, respectively. As one of the objectives of the current study is to model flow generated sound, the choice of turbulence model is very important. Hence, different turbulent models were used to validate the CFD results comparing with the velocity measurements using Laser Doppler Anemometry (LDA). The selected models are appropriate to be utilized for the simulations, in which capturing the flow fluctuations are important for sound analysis. The fluctuations of the flow parameters (such as, pressure and velocity fluctuations) are known as sound sources [112].

2.1.1 Reynolds-Averaged Navier-Stokes (RANS) Models

RANS equations are derived by applying the Reynolds decomposition to the flow variables in Navier-Stokes equations. For a flow quantity, Reynolds decomposition is applied as following.

$$\varphi = \langle\varphi\rangle + \varphi' \tag{2-3}$$

here, $\langle\varphi\rangle$ represents the mean value or the ensembled average of the flow quantity while φ' and φ represents the fluctuating and instantaneous terms, respectively. After applying the Reynolds decomposition to flow variables and the assumption of the incompressibility of the flow, RANS equations are obtained as,

$$\frac{\partial\langle u_i\rangle}{\partial x_i} = 0 \tag{2-4}$$

$$\frac{\partial\langle u_i\rangle}{\partial t} + \frac{\partial\langle u_i\rangle\langle u_j\rangle}{\partial x_j} = -\frac{1}{\rho}\frac{\partial\langle p\rangle}{\partial x_i} + \upsilon\frac{\partial^2\langle u_i\rangle}{\partial x_j\partial x_j} - \frac{\partial\langle u_i{}'u_j{}'\rangle}{\partial x_j} \tag{2-5}$$

where, υ is the kinematic viscosity. In Equation 2-5, the first term in left-hand side represents the mean momentum change in a fluid element due to the unsteadiness in the mean flow while the second term describes the mean momentum change due to convection by the mean flow. These momentum changes are balanced by the source terms in the right-hand side which consist of mean pressure, viscous stresses, and the third source term which contains the fluctuating velocity components. The term $\langle u_i{}'u_j{}'\rangle$ is known as "Reynolds stress" and requires additional modelling to solve RANS equations.

Equation 2-5 can be further simplified using the turbulent viscosity relation introduced by Boussinesq [113], also known as Boussinesq approximation. Boussinesq described that the momentum transfer due to turbulence eddies can be modeled using turbulent viscosity (or eddy viscosity), υ_t, which relates turbulent stresses to the mean flow velocities as,

$$-\langle u_i{}'u_j{}'\rangle + \frac{2}{3}k\delta_{ij} = \upsilon_t\left(\frac{\partial\langle u_i\rangle}{\partial x_j} + \frac{\partial\langle u_j\rangle}{\partial x_i}\right) \tag{2-6}$$

$$k \equiv \frac{1}{2}\langle u_i' u_i' \rangle \tag{2-7}$$

where, δ_{ij} is the Kronecker delta function and k is the turbulent kinetic energy. The following equation can be derived by substituting Equations 6 and 7 in Equation 5,

$$\frac{\partial \langle u_i \rangle}{\partial t} + \frac{\partial \langle u_i \rangle \langle u_j \rangle}{\partial x_j} = -\frac{1}{\rho}\frac{\partial (\langle p \rangle + \frac{2}{3}k\rho)}{\partial x_i} + (\upsilon + \upsilon_t)\frac{\partial^2 \langle u_i \rangle}{\partial x_j \partial x_j} \tag{2-8}$$

where, $\upsilon_{effective} = (\upsilon + \upsilon_T)$ is known as the effective viscosity. However, to solve RANS equations (Equations 2-4 and 2-8), turbulent viscosity υ_t should be determined. Many turbulence models are available for determining turbulent viscosity while some of the most common models are described in the following sections.

2.1.1.1 RANS k-ω Model

The RANS *k-ω* turbulence model is a two-equation model that solves transport equations for the turbulent kinetic energy (*k*) and the specific dissipation rate (*ω*), which is the turbulent dissipation rate (*ε*) per unit turbulent kinetic energy ($\omega \propto \varepsilon/k$),

$$\frac{\partial k}{\partial t} + \langle u_j \rangle \frac{\partial k}{\partial x_j} = \tau_{ij}\frac{\partial u_i}{\partial x_j} - \beta^* k\omega + \frac{\partial\left[(\upsilon + \sigma_k \upsilon_t)\frac{\partial k}{\partial x_j}\right]}{\partial x_j} \tag{2-9}$$

$$\frac{\partial \omega}{\partial t} + \langle u_j \rangle \frac{\partial \omega}{\partial x_j} = \alpha\frac{\omega}{k}\tau_{ij}\frac{\partial u_i}{\partial x_j} - \beta\omega^2 + \frac{\partial\left[(\upsilon + \sigma_\omega \upsilon_t)\frac{\partial \omega}{\partial x_j}\right]}{\partial x_j} \tag{2-10}$$

where, turbulent viscosity is defined as,

$$\upsilon_t = \frac{k}{\omega} \tag{2-11}$$

In the above equations: τ_{ij} is the mean stress tensor. The terms $\alpha, \beta, \beta^*, \sigma_k, \sigma_\omega$ are closure coefficients which can be found in detail in [114,115]. The *k-ω* two-equation model for low-Reynolds number flows was first proposed by Wilcox [114] and revised to better predict low-Reynolds number and transitional flows [115].

2.1.1.2 RANS shear stress transport (SST) k-ω model

The revised model of RANS *k-ω* accounted for several perceived deficiencies of the original version such as extreme sensitivity to inlet boundary conditions for internal flows [115]. The advantage of this model over the *k-ε* model is its improved performance for boundary layers under adverse pressure gradients [114,116]. On the other hand, the *k-ε* two-equation turbulence model, which solves transport equations for the turbulent kinetic energy and turbulent dissipation rate to calculate the turbulent viscosity, is more robust in wake regions and free shear flows [117]. These distinct capabilities led to the development of an integrated model that takes advantages of both models. This revised model was developed by Menter [118]. Transport equations for k and ω are shown in Equation 2-12 and 2-13,

$$\frac{\partial k}{\partial t} + \langle u_j \rangle \frac{\partial k}{\partial x_j} = 2v_t \overline{S_{\iota J} S_{\iota J}} - \beta^* k\omega + \frac{\partial \left[(\upsilon + \sigma_k \upsilon_t) \frac{\partial k}{\partial x_j} \right]}{\partial x_j} \tag{2-12}$$

$$\frac{\partial \omega}{\partial t} + \langle u_j \rangle \frac{\partial \omega}{\partial x_j} = \alpha \overline{S_{\iota J} S_{\iota J}} - \beta \omega^2 + \frac{\partial \left[(\upsilon + \sigma_\omega \upsilon_t) \frac{\partial \omega}{\partial x_j} \right]}{\partial x_j} + 2(1 - F_1)\sigma_{\omega 2} \frac{1}{\omega} \frac{\partial k}{\partial x_i} \frac{\partial \omega}{\partial x_i} \tag{2-13}$$

In above equations: k is turbulent kinetic energy, ω is turbulent dissipation rate, and $\overline{S_{\iota J}}$, is the mean strain rate tensor. The SST *k-ω* model is essentially a *k-ω* model near wall boundaries and is equivalent to a transformed *k-ε* model in regions far from walls controlled by blending function (F_1), (see, Equation 2-17). In this model, the turbulent viscosity (v_t) is calculated as,

$$v_t = \rho k T \tag{2-14}$$

where, ρ is density, k is turbulent kinetic energy, and T is the turbulent time scale. The turbulent kinetic energy can be defined as,

$$k = \frac{3}{2}(UI)^2 \tag{2-15}$$

where, U is the initial velocity magnitude, and I is initial turbulence intensity. In addition, the turbulent time scale in Equation 2-14 can be calculated using Durbin's realizability constraint as,

$$T = min\left(\frac{\alpha^*}{\omega}, \frac{\alpha}{S\,F_1}\right) \tag{2-16}$$

where, S is the mean strain rate tensor. In this equation, α^* and α are model coefficients equal to 1 and 0.3, respectively [118]. F_1 can also be defined as,

$$F_1 = tanh((max\left(\frac{2\sqrt{k}}{\beta^*\omega d}, \frac{500v_k}{d^2\omega}\right))^2) \tag{2-17}$$

where, $k, \omega, v_t,$ and d are turbulent kinetic energy, specific dissipation rate, kinetic viscosity, and distance to wall, respectively [118]. β^* is the model coefficient,

$$\beta^* = F_1\beta_1^* + (1 - F_2)\beta_2^* \tag{2-18}$$

where, β_1^* and β_2^* are equal to 0.09, and F_2 can be illustrated as,

$$F_2 = tanh([min(max\left(\frac{\sqrt{k}}{0.09\omega d}, \frac{500v}{d^2\omega}\right), \frac{2\sqrt{k}}{d^2 CD_{k\omega}})]^4) \tag{2-19}$$

where, $CD_{k\omega} = max(\frac{1}{\omega}\nabla k.\nabla\omega, 10^{-20})$ is cross-diffusion coefficient.

2.1.1.3 RANS Reynolds Stress Transport (RST) model

The development and application of Reynolds stress models can be traced back to the 1970s [119,120]. This model, also known as the second-moment closure model, directly calculates all components of the specific Reynolds stress tensor by solving governing transport equations, instead of calculating turbulence eddy viscosity,

$$\frac{D\langle u_i'u_j'\rangle}{Dt} = -\left(\langle u_i'u_k'\rangle\frac{\partial U_j}{\partial x_k} + \langle u_j'u_k'\rangle\frac{\partial U_i}{\partial x_k}\right) - 2\nu\frac{\partial\langle u_i'\rangle}{\partial x_k}\frac{\partial\langle u_j'\rangle}{\partial x_k} + \frac{\langle p\rangle}{\rho}\left(\frac{\partial\langle u_i'\rangle}{\partial x_j} + \frac{\partial\langle u_j'\rangle}{\partial x_i}\right) -$$

$$\frac{\partial}{\partial x_k}(\langle u_i'u_j'u_k'\rangle + \frac{\langle pu_i'\rangle}{\rho\delta_{jk}} + \frac{\langle pu_j'\rangle}{\rho\delta_{ik}} - \nu\frac{\partial\langle u_i'u_j'\rangle}{\partial x_k}) \tag{2-20}$$

Solving the Reynold stress transport equations requires closure models to compute second, third and fourth terms in the right hand side of Equation 2-20 [121]. Reynold stress transport model

is computationally more expensive than eddy viscosity models (such as $k-\omega, k-\varepsilon$). This model also has the potential of predicting complex flows more accurately than two-equation models. These are due to the facts that the transport equations or the Reynolds stress model naturally account for the effects of turbulence anisotropy, streamline curvature, swirl rotation and high strain rates [122–124]. In this model, the turbulent viscosity is computed as,

$$v_t = \rho C_\mu \frac{k^2}{\varepsilon} \tag{2-21}$$

where, ρ is density, ε is isotropic turbulent dissipation, and C_μ is the model coefficient equal to 0.09. The turbulent kinetic energy (k) can be defined as,

$$k = \frac{1}{2} tr(R) \tag{2-22}$$

where, tr(R) represents the trace of Reynolds stress tensor (R). The tensor R can be written as,

$$R = \begin{bmatrix} \sigma_{xx} & \tau_{xy} & \tau_{xz} \\ \tau_{yx} & \sigma_{yy} & \tau_{yz} \\ \tau_{zx} & \tau_{zy} & \sigma_{zz} \end{bmatrix} = \rho \begin{bmatrix} \overline{u'u'} & \overline{u'v'} & \overline{u'w'} \\ \overline{v'u'} & \overline{v'v'} & \overline{v'w'} \\ \overline{w'u'} & \overline{w'v'} & \overline{w'w'} \end{bmatrix} \tag{2-23}$$

here, u', v', and w' are the velocity fluctuation components and, σ and τ represent normal and shear stresses, respectively

2.1.2 Large Eddy Simulation (LES)

Based on Kolmogorov theory [125,126], large scale eddies contain most of the turbulence energy. LES directly calculates the large-scale motions while smaller scales are modeled under the assumption that they behave isotopically as stated in Kolmogorov theory [127]. To differentiate between the larger scale and smaller scale motions, LES uses a low-pass filter to decompose flow velocity as well as other flow variables. This filtering is a mathematical operation intended to remove a range of small scales from the solution to the Navier-Stokes equations. Due to the principal difficulty in simulating turbulent flows comes from the wide range of length and time scales, this operation makes turbulent flow simulation cheaper by reducing the range of scales that

must be resolved. The low-pass filtering operation used in LES can be applied to a spatial and temporal field, and it removes scales associated with high frequencies

In Equation 2-24, $\bar{u}$ represents the larger resolved scales while u' is the smaller unresolved scale, which is also known as the subgrid-scale component,

$$\bar{u} = u - u' \tag{2-24}$$

This is achieved by applying the following filtering operation,

$$\bar{u} = \oint u(x')G(x, x'; \Delta)dx' \tag{2-25}$$

where the filter function $\mathrm{G}(\mathrm{x}, \mathrm{x}'; \Delta)$ satisfies,

$$\oint G(x, x'; \Delta)dx' = 1 \tag{2-26}$$

The filtered Navier-stokes equations are,

$$\frac{\partial \overline{u_i}}{\partial x_i} = 0 \tag{2-27}$$

$$\frac{\partial \overline{u_i}}{\partial t} + \frac{\partial\, \overline{u_i u_j}}{\partial x_j} = -\frac{1}{\rho}\frac{\partial \bar{p}}{\partial x_i} + \upsilon \frac{\partial^2 \overline{u_i}}{\partial x_j \partial x_j} \tag{2-28}$$

where in this equation, $\bar{p}$ is the filtered pressure term and $\overline{u_i u_j}$ is a nonlinear convective term which links the resolved (larger eddies) and unresolved (smaller eddies) as following,

$$\tau_{ij}^R = \overline{u_i u_j} - \overline{u_i}\,\overline{u_j} \tag{2-29}$$

where τ_{ij}^R is the sub-grid scale stress and it is decomposed as,

$$\tau_{ij}^R = \tau_{ij}^r + \frac{2}{3}k_r \delta_{ij} \tag{2-30}$$

In Equation 2-30, the residual kinetic energy (k_r) is defined as half of the trace of the sub-grid scale stress tensor, $k_r \equiv \frac{1}{2}\tau_{ij}^R$ and τ_{ij}^r is the residual stress term. Substituting Equations 29 and 30 in Equation 28 can be rewritten as,

$$\frac{\partial \overline{u_i}}{\partial t} + \frac{\partial \overline{u_i u_j}}{\partial x_j} = -\frac{1}{\rho}\frac{\partial \bar{p}}{\partial x_i} + \upsilon \frac{\partial^2 \langle u_i \rangle}{\partial x_j \partial x_j} - \frac{\partial \tau_{ij}^r}{\partial x_j} \tag{2-31}$$

The closure can be achieved by an eddy viscosity model which relates the residual stress term τ_{ij}^{r} to the resolved rate of strain tensor $\overline{S_{ij}}$ with the eddy viscosity of the unresolved motions υ_t,

$$-\tau_{ij}^{r} = 2\upsilon_t \overline{S_{ij}} \tag{2-32}$$

$$2\overline{S_{ij}} = \left(\frac{\partial \overline{u_i}}{\partial x_j} + \frac{\partial \overline{u_j}}{\partial x_i}\right) \tag{2-33}$$

Using above relations Equation 2-31 can be reduced to:

$$\frac{\partial \overline{u_i}}{\partial t} + \frac{\partial \overline{u_i u_j}}{\partial x_j} = -\frac{1}{\rho}\frac{\partial (\bar{p} + \frac{2}{3}k_r\rho)}{\partial x_i} + (\upsilon + \upsilon_t)\frac{\partial^2 \langle u_i \rangle}{\partial x_j \partial x_j} \tag{2-34}$$

To model υ_t , a sub-grid scale (SGS) model is needed. In this study, Smagorinsky SGS model is used to model υ_t since it performs well for wall bounded flows [128]. The LES Smagorinsky Subgrid Scale provides the following mixing-length type formula for the subgrid scale viscosity [129]:

$$\upsilon_t = \rho \Delta^2 \bar{S} \tag{2-35}$$

where Δ is the length scale or grid filter width. The length scale Δ is directly related to the cell volume (V) and the wall distance, *d*, as follows:

$$\Delta = \begin{cases} f_v C_s V^{1/3} & \text{if length scale limit is not applied} \\ f_v \, min\left(\kappa d, C_s V^{\frac{1}{3}}\right) & \text{if length scale limit is applied} \end{cases} \tag{2-36}$$

where, C_s is model coefficient of 0.1, and $\kappa = 0.41$ is von Karman constant [130]. In Equation 2-36, f_v is the Van Driest damping function. The turbulent eddy viscosity in standard Smagorinsky model is nonzero at solid boundaries and turbulence can be overestimated near the walls; hence the addition of this damping function handles this problem. More information about the applications of the Van Driest damping function in turbulence modeling can be found in [131].

2.1.3 Detached Eddy Simulation (DES)

DES is a hybrid RANS-LES computational approach which focuses on combining the advantages of both RANS and LES methods [102,132]. The boundary layers and irrotational flow regions are solved using a RANS closure model while it will emulate LES subgrid scale (SGS) model in detached flow regions if the grid is fine enough [133]. Although it's computationally expensive than RANS turbulent models, its known to provide better results since ability of RANS to solve unsteady turbulent motion is limited. This model acts like RANS where the flow is attached to boundary layers and switches to LES where flow separation is present [134]. As discussed in the previous sections, both RANS and LES have similar formulations and in both equations, unknown eddy viscosity term need to be modeled. These similarities in the equations allow the uniform switching between RANS and LES to solve the flow problem. The switching between the two models (RANS model and SGS model) is done based on the local grid resolution and the distance from the wall [134]. For the current study, SST k-ω and Smagorinsky SGS model was employed in DES simulation. DES may cause some issues due to inaccurate switching to LES-mode from RANS mode inside the boundary layer. This is known to be caused due to the ambiguous grid spacing close to walls which causes the model to switch to LES mode inside the boundary layer, causing grid-induced separation [135]. This model incorporates the k-ω SST model as proposed by Menter [109] and is mostly appropriate for applications including complex recirculation systems and at high Reynolds numbers [136]. While DES holds great promise for certain types of simulations, it must be cautioned that it is not the answer to all turbulence modeling problems [137].

2.2 Verification of Turbulence Models

Research studies on low Reynolds number flows are less commonly found, although they are highly relevant to biomedical applications. These flows with such low Reynolds number are considered turbulent include those created through glottis in the upper airways [104] and blood flow through aortic heart valve.

2.2.1 CFD Modelling

The exact shape of an arterial stenosis varies from subject to subject and modeling it with accuracy is difficult. Hence, a simplified stenosis shape will be considered in the current study. The schematic of the flow domain and the stenosis with the length of L_c = 15 mm are shown in Figure 2-1. An area reduction of 75% was chosen to model a moderate stenosis [138], where the pipe and stenosis inner diameters were D = 20.6 mm and dc = 10.3 mm, respectively. In addition, 7 equally-spaced (by 3 cm) points on the centerline of the pipe were chosen for velocity measurements.

The flow direction was set to z-direction in simulations as shown by an arrow in Figure 2-1. In these CFD simulations, the entrance length of the tube upstream of the constriction was L_1 = 20 mm with a constant mean inlet velocity ($\bar{U}_{inlet}$) of 0.89 ms^{-1}, which equals the mean inlet velocity measured with LDA. The outlet boundary condition was set to zero pressure ($P = 0$). The density and dynamic viscosity of air were set to ρ = 1.184 $kg.m^{-3}$ and μ = 1.855E^{-5} Pa.s, respectively. These led to an inlet peak Reynolds number ($Re_{inlet} = (\rho \bar{U}_{inlet} D)/\mu$) of ~1170, and turbulent intensity of 5% (similar to the value measurement in the experiment). Also, initial velocity was set to a value close to inlet velocity to reduce the initial residual errors. The impact of the glass tube roughness was not considered in this study. The boundary conditions as well as turbulence parameters in this simple model are defined based on the previous studies in this field.

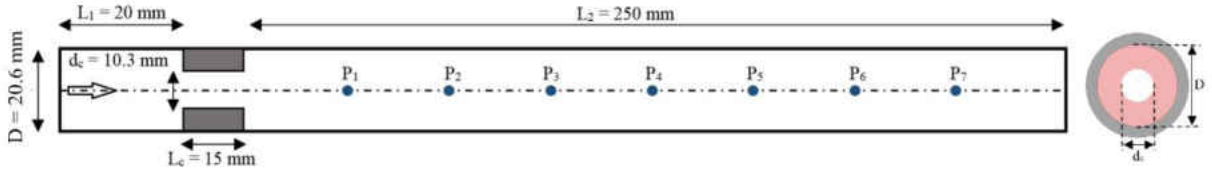

Figure 2-1 Schematic of the stenosed artery (pipe with constriction). Points P1 to P7 denote velocity measurement locations in the tube.

This study was conducted using the commercial CFD code STAR-CCM+ (CD-adapco-Siemens, TX, USA) to evaluate the different turbulence methods for an internal bounded flow. A time step of 0.0001 s was used to ensure adequate time step convergence (less than 10^{-4} for all residuals), which was particularly important with SRS models [139]. All simulations used 2nd-order spatial and temporal discretization accuracy for all equations.

2.2.2 Mesh/Grid Configuration

The use of scale-resolving simulation (SRS) turbulence models for wall bounded flows requires high quality mesh. When creating such mesh, it is important that $y^+ \leq 1$ [98,140]. Polyhedral mesh was generated throughout the flow domain, with a refined mesh at the constriction and wake regions, Fig. 2a. This led to a mesh containing ~2 million cells. In addition, accurate prediction of pressure drop in flows with separation depends on resolving the velocity gradients normal to the wall, as prism layers allow the solver to resolve near wall flow accurately [141,142]. Hence, a 5-layer prism layer mesh with a total thickness of 0.0003 m and layer stretching factor of 1.5 was employed near the boundaries, as shown in Figure 2-2, to resolve the velocity gradients normal to the wall. The y^+ value was maintained in the order of 1 for all turbulence models chosen in this study. In addition, a grid independent study was conducted to find the optimized mesh configuration as shown in Figure 2-3. Four different mesh configurations, mesh 1, 2, 3, and 4, were set up with approximately 700k, 1.4M, 2M, and 2.3M number of mesh cells. The evaluation of the mean velocity in flow direction (z-direction in this simulation) along

the pipe indicated that the mesh 3 and 4 setups led to similar results. Therefore, mesh 3 was selected as the optimized mesh.

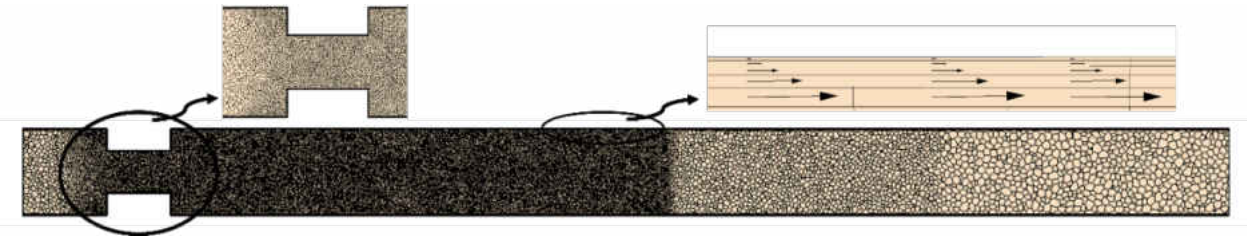

Figure 2-2 Polyhedral mesh generation with prism layers and a refined mesh at and downstream of the constriction.

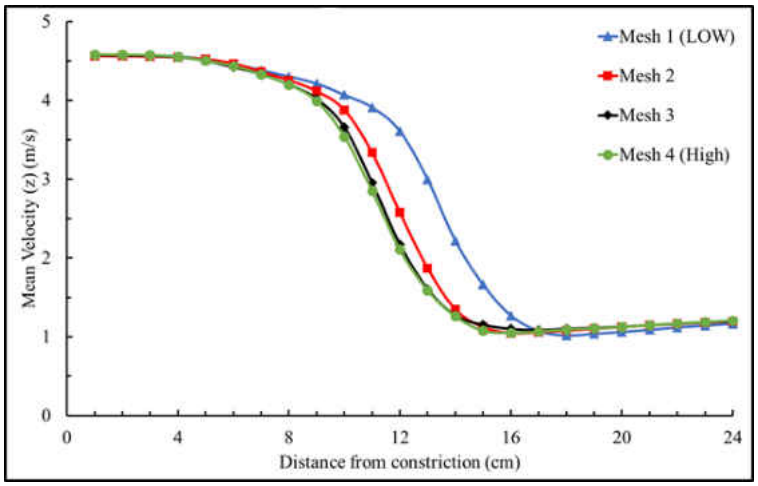

Figure 2-3 Grid independent analysis for the stenosed artery (pipe with constriction).

2.2.3 Experimental Setup and Procedure

In the current study Laser Doppler Anemometry (LDA) was used to measure the velocity. It is a non-intrusive method which does not interfere with the flow field and sound generation. Figure 2-4, shows the configuration of a LDA unit while Figure 2-5 displays the experimental setup for the stenosed artery (pipe with constriction).

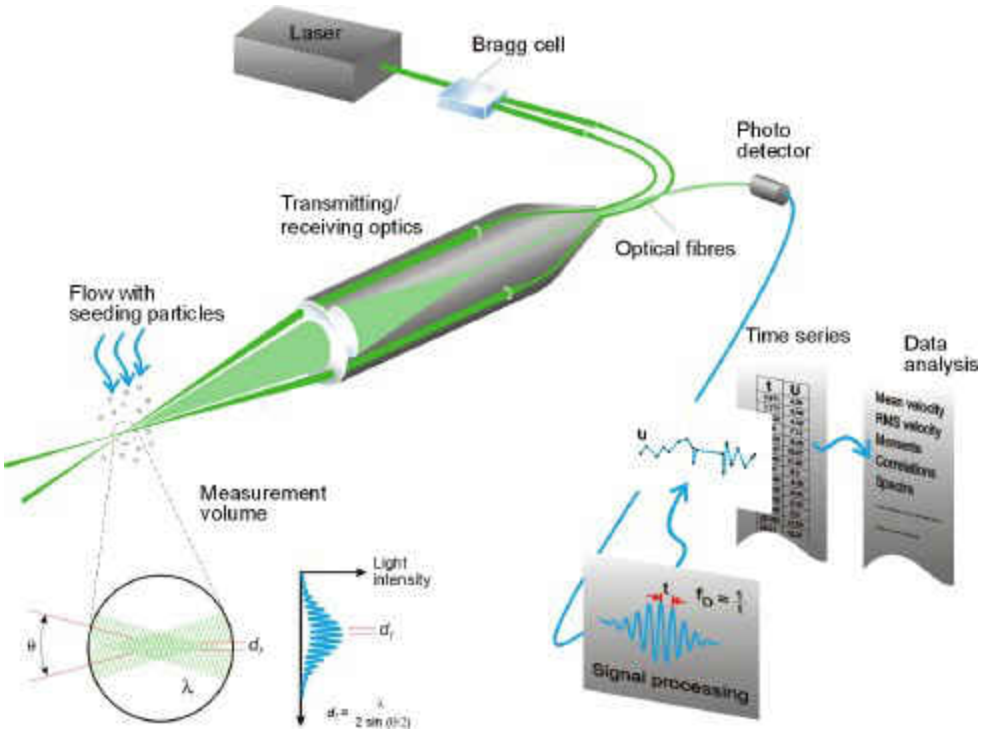

Figure 2-4: The operation procedure of a laser Doppler anemometry (LDA) unit [143]**.**

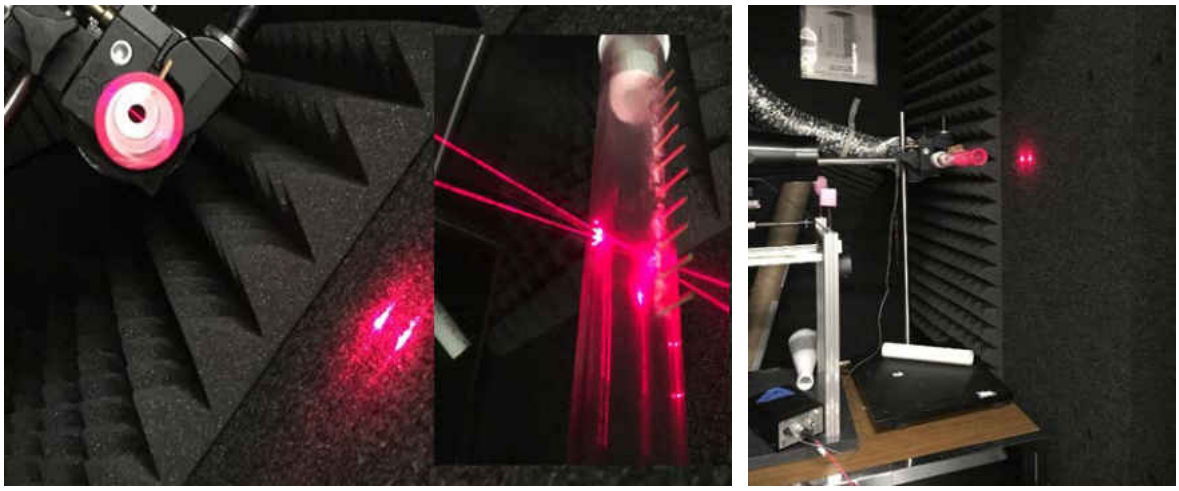

Figure 2-5 Laser Doppler anemometry (LDA) experiment setup for the stenosed artery (pipe with constriction).

The one-dimensional velocity measurements were obtained with a LDA system (Dantec Dynamics A/S., Skovulunde, Denmark [143]) used in backscatter mode. Laser Doppler Anemometry (LDA) measurements were performed at selected centerline locations (P1-P7 in

Figure 2-1) downstream of the constriction to obtain a detailed representation of the flow characteristics. The entrance length of the pipe prior to the constriction was long enough to reach an approximately fully developed turbulent airflow with the mean velocity of 0.89 $m.s^{-1}$ and the peak center-velocity of ~1 $m.s^{-1}$ at the inlet.

A Bragg cell was used to add an 80 MHz frequency shift to the beam with 660 nm wavelength. The "Bragg cell" split the laser beam in to two beams with same intensity, but with a frequency shift. In addition, a two-component fiber optic transceiver (Model FlowExplorer; Dantec Dynamics A/S., Skovulunde, Denmark [143]) with a 300-mm focal length lens was coupled to a fiber drive to produce an ellipsoidal probe volume with minor and major axes of 0.1 mm and 1 mm, respectively. The beam intersection generates parallel planes with high light intensity which are called "fringes". Distance between fringes can be estimated based on the wave length and the angles between the beams. When seeding particles pass through this region they scatter the light, which create a Doppler shift where the Doppler frequency is proportional to the particle velocities. A photodetector collects the scattered light and converts the light intensity to an electrical signal. The noise from other wave lengths such as ambient light is filtered prior to photo detector. The output electrical signal from the photo detector is called the "Doppler burst" signal which is later processed to determine the Doppler frequency shift of each seeding particle crossing the probe volume. Velocity of each seeding particle is calculated based on the fringe distance and the Doppler frequency shift.

High number of measurement samples (>~2000, with varying frequency between 200-1000 Hz) were acquired at each measurement location to ensure accurate results. The LDA system was calibrated for high-accuracy velocity measurements with calibration coefficient uncertainty lower

than 0.1% (stated by Dantec Dynamics A/S., Skovulunde, Denmark [143]) and mean confidence internal less than 0.09 $m.s^{-1}$.

2.2.4 Results and Discussions

Figure 2-6 shows the mean velocity measurements in the flow direction (z-component) at 7 different locations (i.e., P1 to P7 in Figure 2-1) downstream of the constriction using LDA. The velocity measurements were performed for 30 seconds at each location. Three seconds of data were included in this figure to more clearly show the flow fluctuations. P1 and P2 were located in the "jet region" of the constriction and had the highest mean velocities and lowest fluctuations. The mean velocities at P1 and P2 were 4.66 and 4.63 $m.s^{-1}$ while the root-mean-square (RMS) of the velocity fluctuations were 0.047 and 0.115 $m.s^{-1}$, respectively. On the other hand, the highest fluctuations along with a significant drop in the mean velocities were observed at the next three center-points (P3, P4, and P5). Here, the mean velocities were 2.09, 1.17, and 1.11 $m.s^{-1}$, and RMS fluctuations were 0.708, 0.503, and 0.205 $m.s^{-1}$ at P3, P4, and P5, respectively. In the current study, this region with the highest fluctuations is called the "fluctuating zone". It can be noted that the RMS of the fluctuations decreased from P3 to P5 where the flow reattachment happened till it approaches fully developed/stable conditions at P6 and P7 in the "flow stabilization" region close to the outlet. The mean velocities at P6 and P7 were 1.14 and 1.16 $m.s^{-1}$ while the RMS of the fluctuations were 0.126 and 0.093 $m.s^{-1}$, respectively. Further measurements showed that the starting point of the high fluctuations levels was between P2 and P3. It was also observed that the "jet region" (characterized by high centerline velocity) extended up to about 7 cm downstream of the constriction while the "fluctuating zone" extended beyond this point. The highest value of the RMS velocity fluctuations (strongest turbulent stresses) was seen at 9 cm downstream of the

constriction (P3). In addition, Table 2-1 shows the mean and root mean square (RMS) values of the velocity at each point.

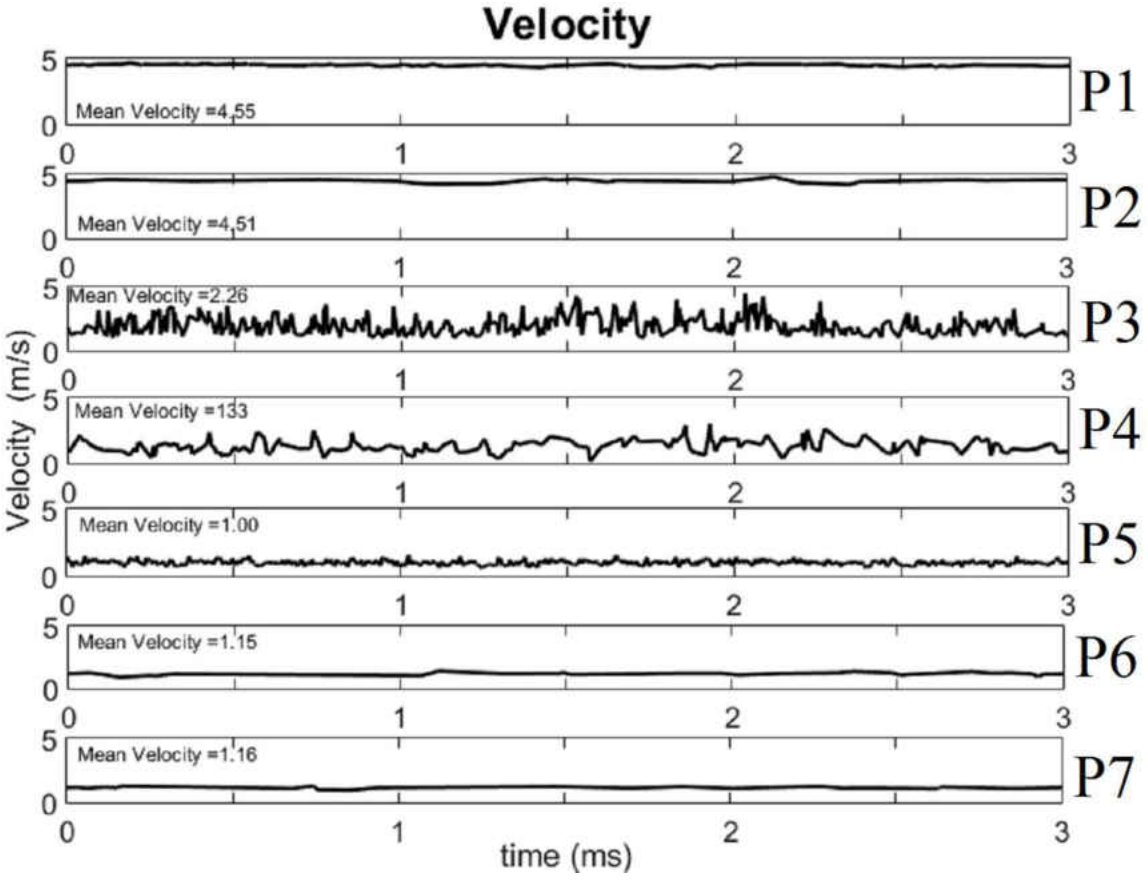

Figure 2-6 Measured axial mean velocities along the centerline of the stenosed artery (pipe with constriction).

Table 2-1: Mean and RMS values of measured velocities

Measurement point	Mean axial velocity (m/s)	RMS of axial velocity (m/s)
P1	4.55	0.047
P2	4.51	0.115
P3	2.26	0.708
P4	1.33	0.503
P5	1.00	0.205
P6	1.15	0.126
P7	1.16	0.063

Figure 2-7 shows the comparison of axial mean velocities along the centerline of the stenosed artery (pipe with constriction) between the computational and experimental results. The results showed that LES model had the best agreement while DES SST k-ω model had the maximum error. RANS models had a better agreement compared to DES SST k-ω model, while RANS RST model delivered better results compared to RANS SST k-ω model. All turbulence models had a good agreement at points P1, P2 and P6, P7, which are in the regions where the high velocity jet initiates and where the flow stabilizes near the outlet. All turbulence models had their highest errors at points P3, P4, and P5 where the high velocity jet is expected to become unstable and dissipate.

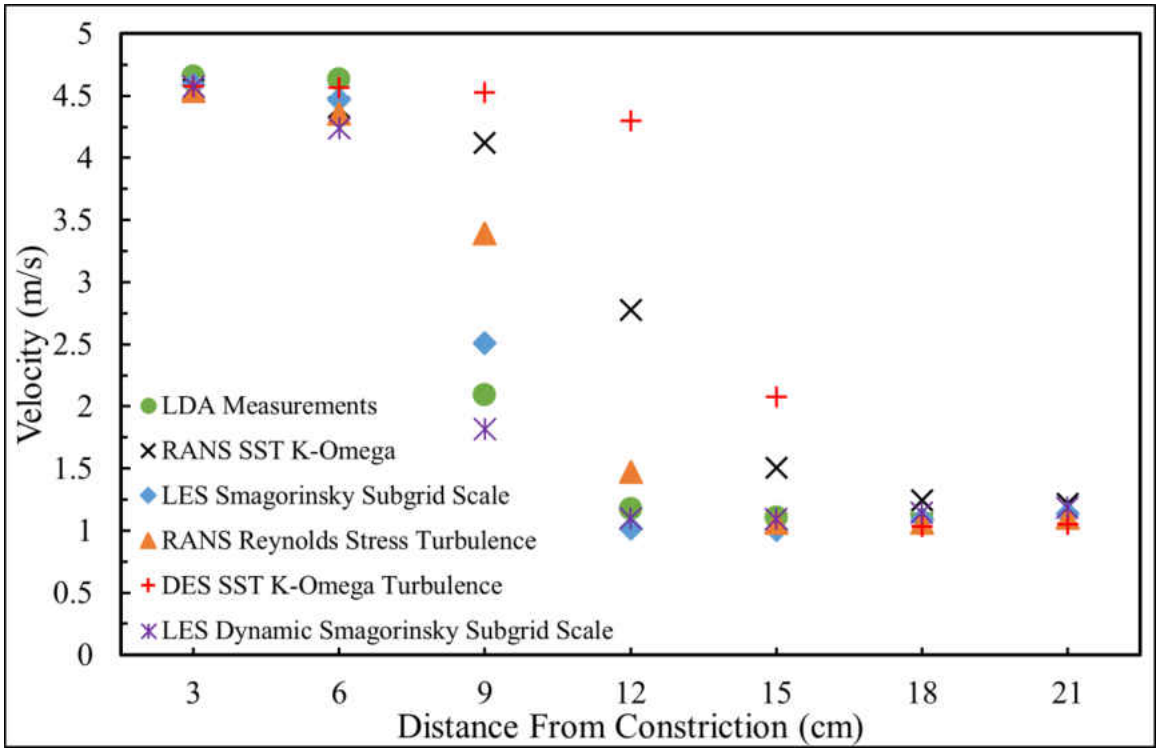

Figure 2-7 Comparison of experimental and computational results for axial mean velocities along the centerline of the stenosed artery (pipe with constriction) for different turbulence models.

Figure 2-8 shows the axial mean velocity at the outlet of the stenosed artery (pipe with constriction) along the diameter from center to the wall. All turbulence models predicted the flow at the outlet as the pipe was long enough for the flow to get stabilized and become fully developed.

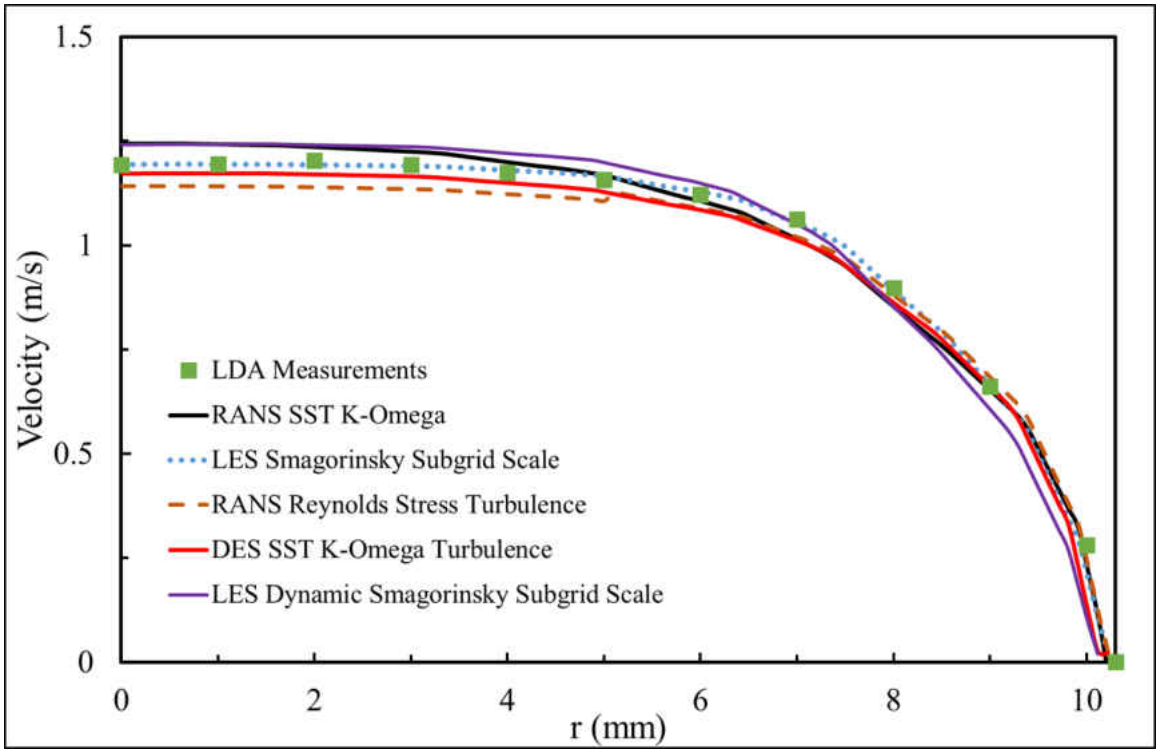

Figure 2-8 Comparison of experimental and computational results for axial mean velocities at the outlet of the stenosed artery (pipe with constriction) for different turbulence models.

As the objective of current study is to model the flow generated sound, accurate modelling of flow fluctuation is paramount to capture sound sources. Figure 2-9 shows the cross-sectional axial mean and RMS of velocity in the flow domain compared between each turbulent model. LES and RANS models (especially, RANS Reynolds Stress model) predicted the mean axial velocity similarly with high accuracy. For the flow fluctuations, the results clearly showed that RANS models perform poorly in capturing the V'_{rms}, compared to LES and DES models. This is expected since RANS models solve for average flow quantities. The two LES models similarly estimated

the velocity fluctuations, but with different amplitudes. Although, DES SST *k-ω* model could capture flow fluctuations, it predicted a delayed flow separation where high fluctuating zone moved toward the downstream.

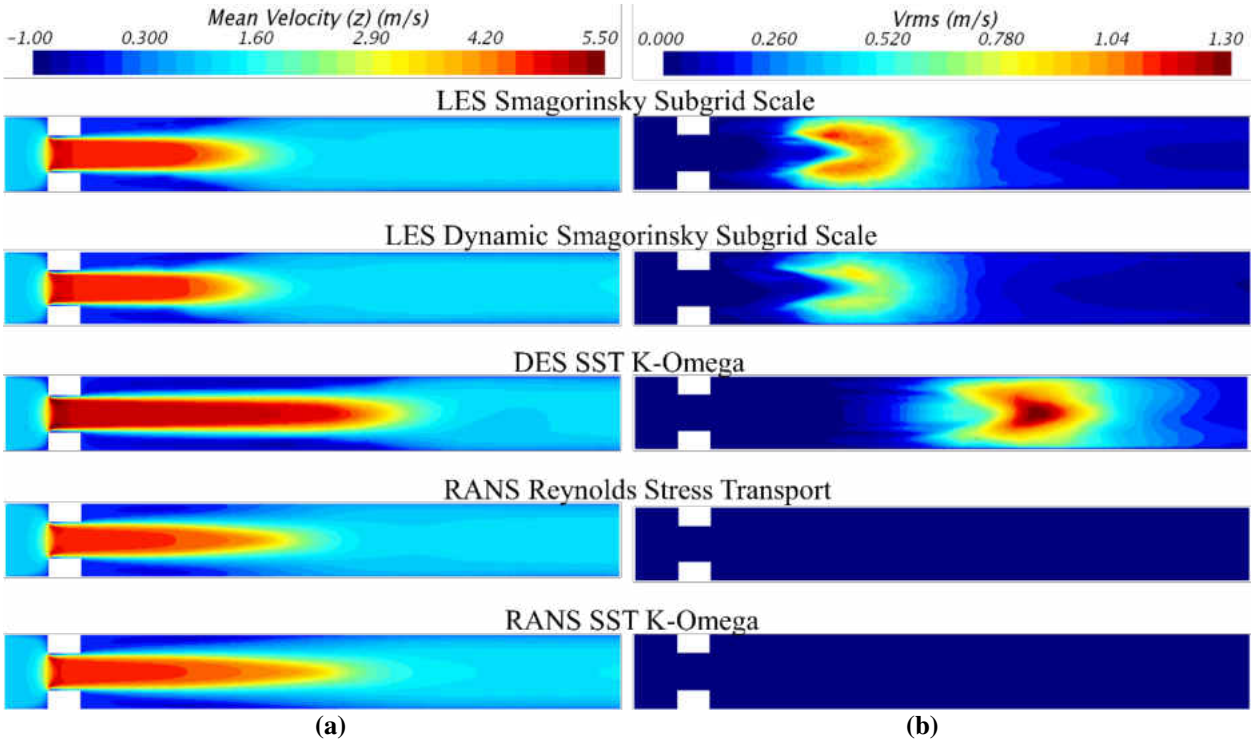

Figure 2-9 Axial mean velocity on the cross-sectional view of the stenosed artery (pipe with constriction) for different turbulence models.

Figure 2-10 shows the vorticity on the cross-section of the tube. Here, the vorticity values are displayed in the range of 0.1 s^{-1} to 8000 s^{-1} for clear comparison of vorticity fluctuations at the high fluctuation zone. Not only LES model accurately captures the flow fluctuations, it also captured smaller eddies compared to DES as seen in vorticity results. It seems that the LES Dynamic Smagorinsky is more sensitive to the flow fluctuations compared to the standard Smagorinsky model. As the DES model in the current study is a hybrid approach of SST *k-ω* and LES, inaccurate modelling of the flow near flow separation by SST *k-ω* is a probable reason for DES model over predicting the fluctuating zone towards downstream.

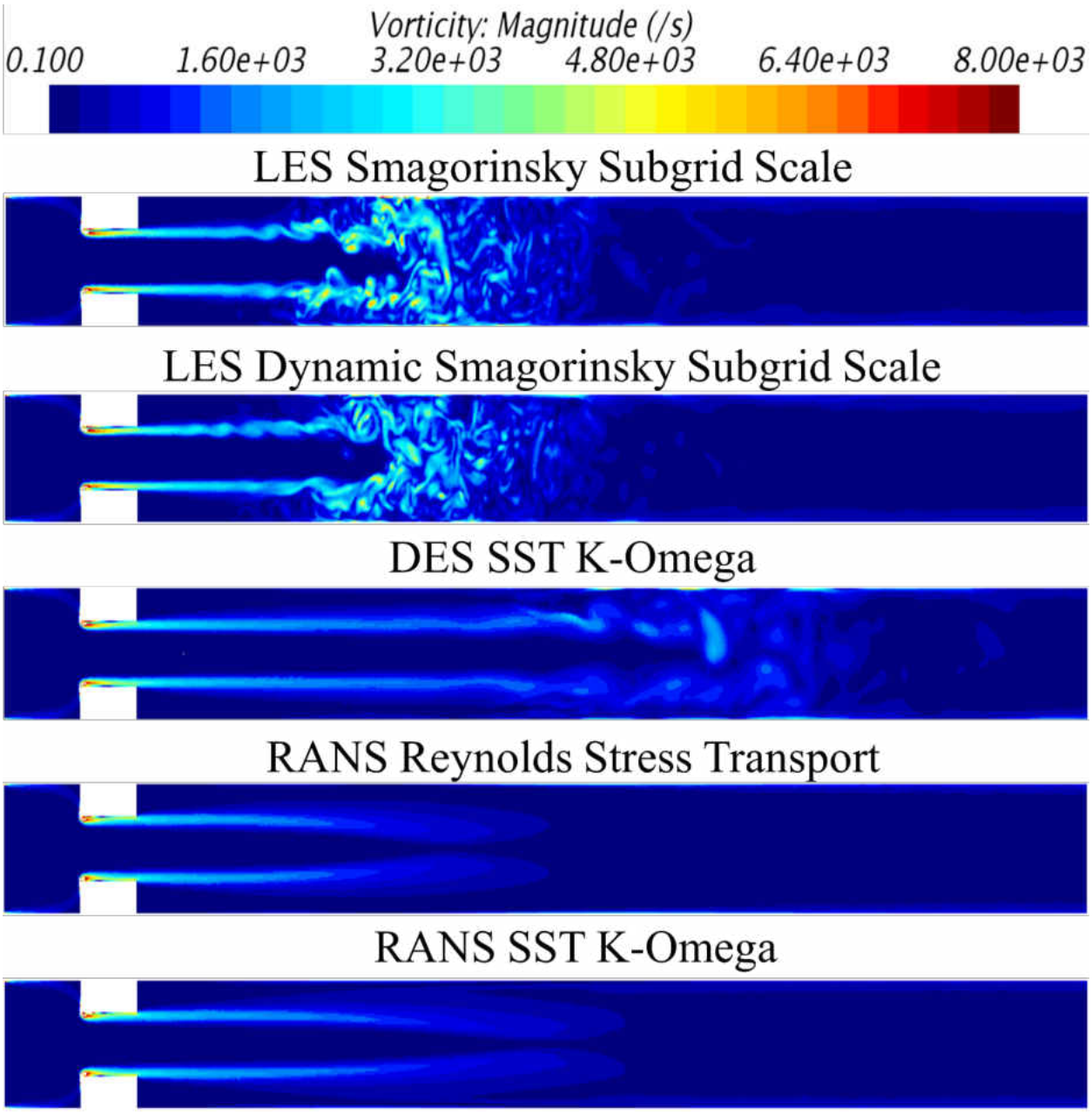

Figure 2-10: Instantaneous vorticity on the cross-sectional view of the stenosed artery (pipe with constriction) for different turbulence models.

In overall, the two LES models (LES Smagorinsky and Dynamic Smagorinsky models) showed promising results for the mean and fluctuating flow parameters. Additional results for the pressure fluctuations in the flow domain and on the wall surfaces are available in [101]. Figure 2-11 shows instantaneous velocity fluctuations for LES models and LDA measurements.

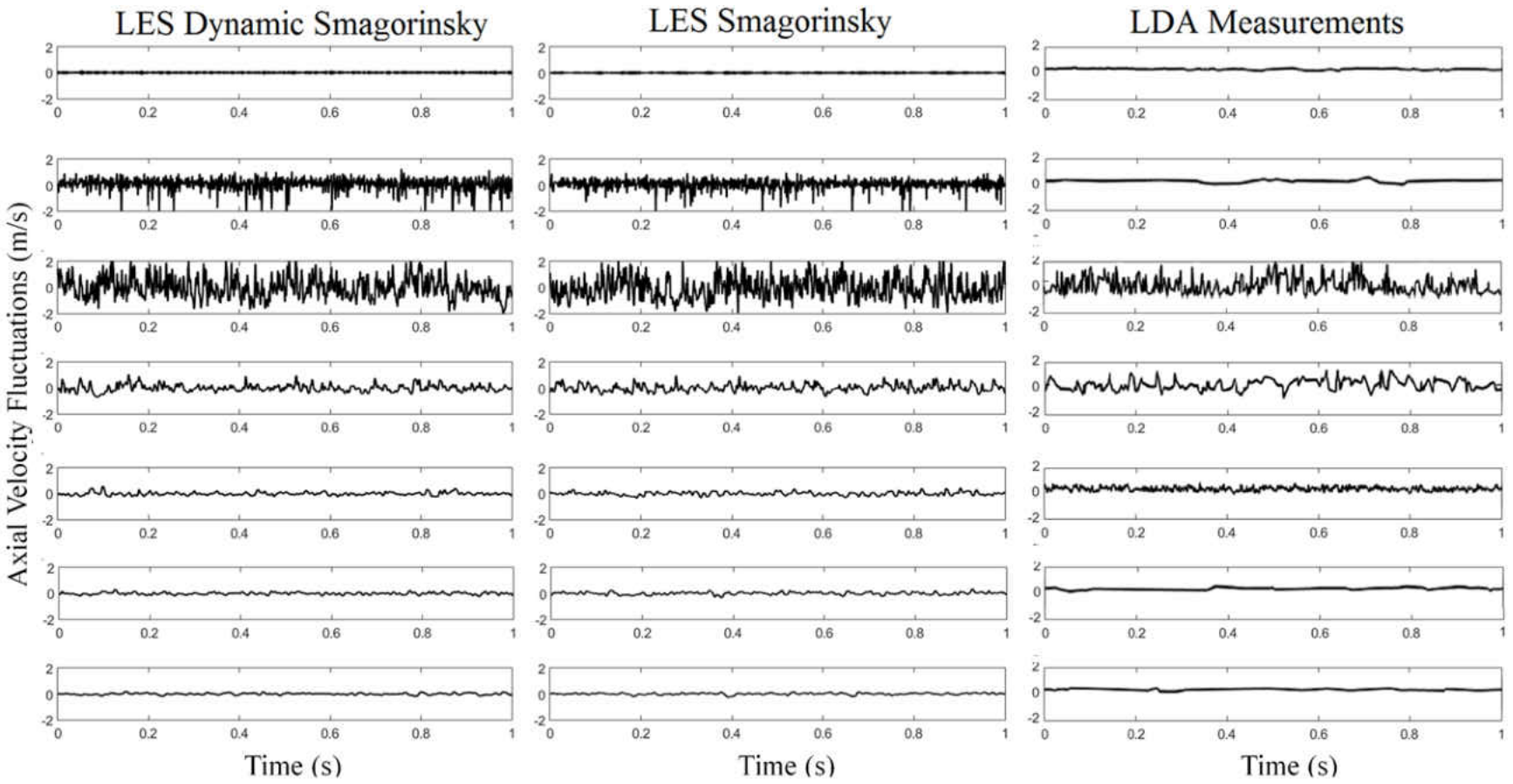

Figure 2-11 Instantaneous velocity fluctuations for LES Smagorinsky and dynamic Smagorinsky turbulence models and LDA measurements.

Figure 2-11 indicates that the LES models predicts the range of the velocity fluctuations along the pipe in all flow regions compared to LDA measurements.

To analyze the suitability of the LES models in detail, further investigation on the velocity profiles along the diameter of the pipe and close to the separation zone was done. Figure 2-12 shows the mean axial velocity profiles at 5 cm and 7 cm downstream of constriction and along the diameter of the pipe from center to the wall. Both LES models are in good agreement with the experimental LDA measurements. For example, the results showed the RMS error of 7.9% and 8.7% for the case of 7 cm downstream of the constriction for LES dynamic Smagorinsky and standard Smagorinsky models, respectively. Therefore, both models are reliable for mean flow calculations for internal flow applications. Table 2-2 shows the detailed information of the computational and experimental results for the mean axial velocity at two different locations in the separation zone (5 cm and 7 cm downstream of the constriction). Velocity was assumed to be 0 m/s at the wall as no-slip condition in the computational configurations.

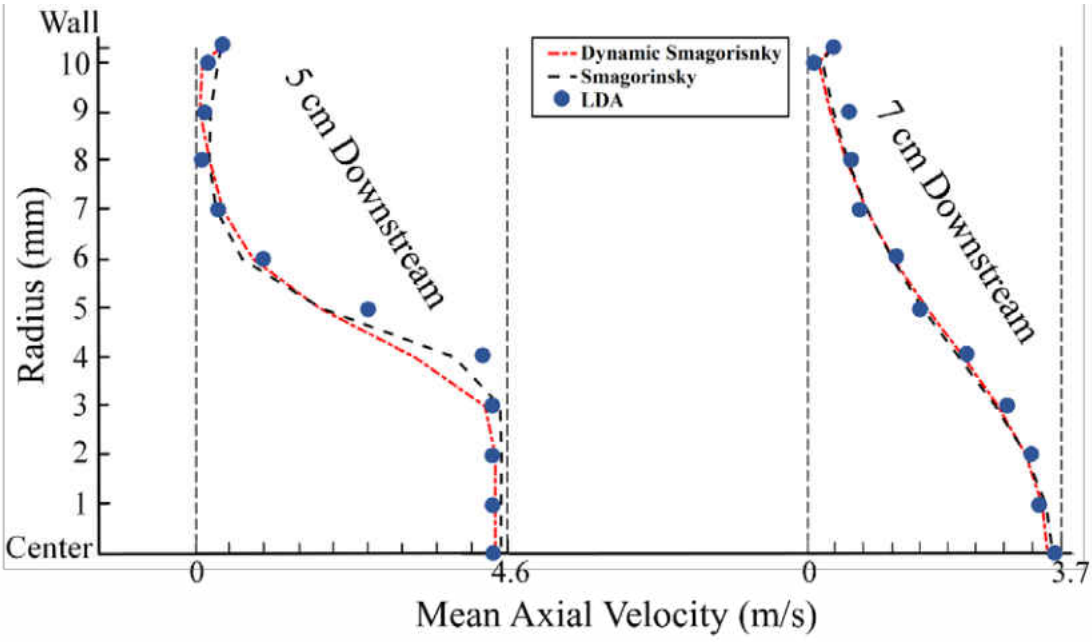

Figure 2-12 Mean axial velocity along the diameter of the stenosed artery (constricted pipe) at 5 cm and 7 cm downstream of the constriction for LES Smagorinsky and dynamic Smagorinsky turbulence models and LDA measurements.

Table 2-2 Mean axial velocity (m/s) at 5 cm and 7 cm downstream of the constriction for LES Smagorinsky and dynamic Smagorinsky turbulence models and LDA measurements

Mean Axial Velocity (m/s)						
Location	5 cm			7 cm		
	LES Dynamic Smagorinsky Subgrid Scale	LES Smagorinsky Subgrid Scale	LDA	LES Dynamic Smagorinsky Subgrid Scale	LES Smagorinsky Subgrid Scale	LDA
Wall	0	0	0	0	0	0
10	-0.3089	-0.0508	-0.1824	-0.1955	-0.1354	-0.2681
9	-0.3477	-0.1699	-0.2626	-0.0116	0.0406	0.0815
8	-0.1811	-0.1925	-0.2958	0.2616	0.2848	0.3011
7	0.0273	-0.0801	-0.0139	0.5850	0.5963	0.5012
6	0.5238	0.3489	0.6883	1.0286	1.0098	1.0858
5	1.6147	1.6367	2.4170	1.5724	1.4997	1.4823
4	3.1763	3.8249	4.3185	2.1773	2.1011	2.2339
3	4.3267	4.5785	4.4577	2.7452	2.7031	2.8792
2	4.4999	4.5997	4.4485	3.1980	3.2052	3.2927
1	4.4983	4.5932	4.4668	3.4682	3.5277	3.5243
Center	4.5009	4.5930	4.4904	3.5534	3.6381	3.6457

Figure 2-13 shows the RMS axial velocity fluctuation profiles at 5 cm and 7 cm downstream of constriction and along the diameter of the pipe from center to the wall. Both LES models are in good agreement with the experimental LDA measurements. For example, the results showed the RMS error of 10.5% and 12.2% for the case of 7 cm downstream of the constriction for LES dynamic Smagorinsky and standard Smagorinsky models, respectively. Therefore, both models are reliable for mean flow calculations for internal flow applications. Table 2-3 shows the detailed information of the computational and experimental results for the RMS axial velocity fluctuation at two different locations in the separation zone (5 cm and 7 cm downstream of the constriction). LES standard Smagorinsky showed more intense fluctuations in the fluctuating zone which is due the damping function discussed in Equation (2-36). The turbulent eddy viscosity in standard Smagorinsky model is nonzero at solid boundaries and turbulence can be overestimated near the walls.

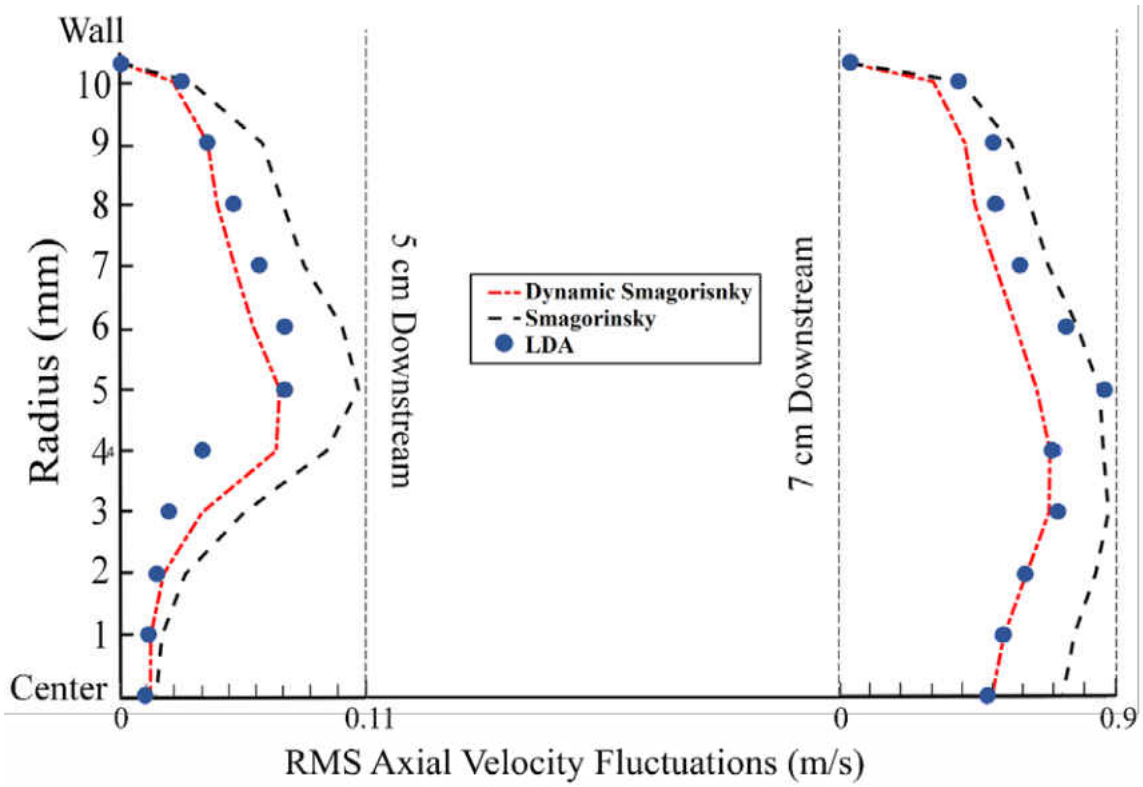

Figure 2-13 RMS axial velocity fluctuation profiles along the diameter of the stenosed artery (constricted pipe) at 5 cm and 7 cm downstream of the constriction for LES Smagorinsky and dynamic Smagorinsky turbulence models and LDA measurements.

Table 2-3 Mean axial velocity (m/s) at 5 cm and 7 cm downstream of the constriction for LES Smagorinsky and dynamic Smagorinsky turbulence models and LDA measurements

$V'_{rms,axial}$ (m/s)						
Location	**5 cm**			**7 cm**		
	LES Dynamic Smagorinsky Subgrid Scale	**LES Smagorinsky Subgrid Scale**	**LDA**	**LES Dynamic Smagorinsky Subgrid Scale**	**LES Smagorinsky Subgrid Scale**	**LDA**
Wall	0	0	0	0	0	0
10	0.2148	0.2841	0.2461	0.3387	0.4499	0.4397
9	0.3570	0.5797	0.3540	0.4682	0.6568	0.6856
8	0.3965	0.6648	0.4590	0.5086	0.7342	0.7024
7	0.4669	0.7523	0.5656	0.5921	0.8095	0.6888
6	0.5448	0.9079	0.6734	0.6778	0.9288	0.7888
5	0.6516	0.9723	0.6735	0.7604	1.0176	0.8844
4	0.6372	0.8433	0.3372	0.8155	1.0326	0.8353
3	0.3351	0.5077	0.1977	0.8113	1.0538	0.8501
2	0.1773	0.2675	0.1463	0.7198	1.0012	0.7147
1	0.1256	0.1705	0.1208	0.6275	0.9137	0.6176
Center	0.1229	0.1474	0.1038	0.5788	0.8670	0.5567

Figure 2-14 displays the z-component of instantaneous velocity (between 1 to maximum velocity of 5.41 $m.s^{-1}$) and streamlines using the LES turbulence model. The different flow regions can be seen including the jet and separation, fluctuating, flow reattachment, and flow stabilization regions, which are similarly labeled to an earlier study [144]. The velocity range in the figure is from 1.00 to the maximum instantaneous velocity of 5.41 $m.s^{-1}$ to help show the flow in the core of as well as the rest of the flow domain.

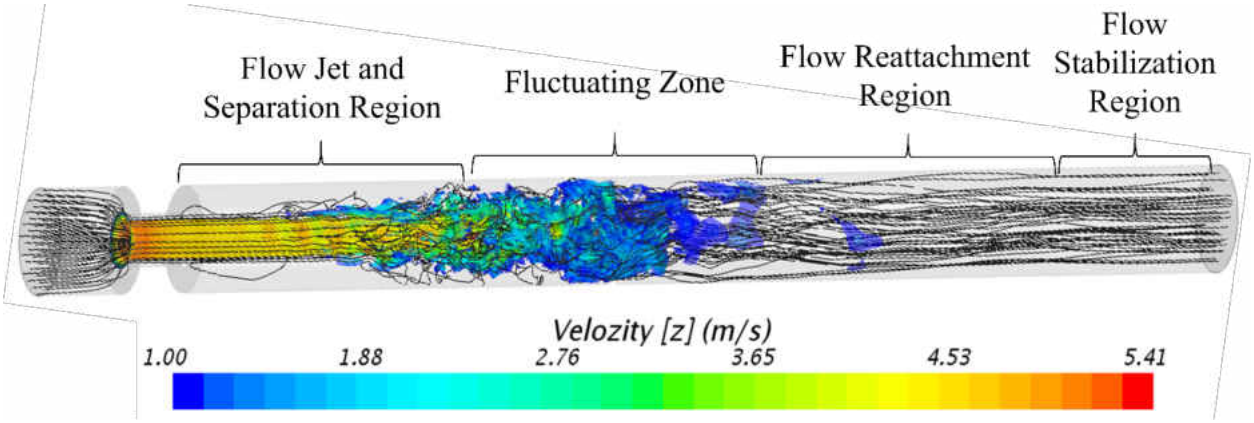

Figure 2-14: Distribution of axial velocity and streamlines (LES Dynamic Smagorinky Subgrid Scale) inside the tube with region classification

The order of the computational costs (the CPU time needed for the entire simulations) for such analysis were found to be for LES, DES, and RANS models. However, for such simple geometries the differences were not significant.

2.2.5 Limitation

In this study, a glass tube was selected as the test section. Due the finite size of the probe volume of the LDA, the velocity distribution cannot be measured very close to the wall. Therefore, the velocity at the tube wall was assumed to be zero due to no-slip condition. Air, as the operating fluid, was considered to be incompressible. In addition, the comparison of more turbulence models with higher mesh quality and simulation time may results in better understanding of their methodology and suitability for internal flows with low Reynolds and Mach numbers.

2.2.6 Conclusions

The current study assessed different turbulence models for the prediction of the flow field downstream of a constricted pipe. Models included Unsteady Reynolds-Averaged Navier-Stokes (URANS) and scale resolving simulation (SRS) turbulence models such as Large Eddy Simulation (LES) and Detached Eddy Simulation (DES). Simulation results were compared with experimental measurements using a one-dimensional laser Doppler anemometry (LDA). Analyses of the mean velocity and local velocity fluctuations indicated that the LES Smagorinsky subgrid scale turbulence model had the highest agreement with experimental results. The accuracy of LES in predicting mean flow was followed by that of RANS Reynolds Stress, RANS k- ω, and then DES. The RANS models do not, resolve turbulent flow fluctuations and eddies that would be a main source of sound generation. This would limit the utility of RANS in aeroacoustic studies. Also, DES did not localize the "fluctuating zone" properly and underestimated the flow fluctuations in the separation zone for this low Reynolds number flow. Therefore, LES would be an optimal turbulence model for internal flow with constriction, especially when sound generation would be of interest.

2.3 Development of a Programmable Pulsatile Heart Pump

Various companies have developed pulsatile pumps to simulate ventricular devices. Among them, the ViVitro Pulse Duplicator system [145,146] and Harvard Apparatus [147–149] are the most common pulsatile blood pumps. These pump allows for a significant amount of research to be conducted in the research field of heart valves. However, with the high cost of replacement parts and the lack of programmability, there is still a need for new pumps that better fits the demands of the research labs. The goal of this study was to develop a programmable and cost effective pulsatile pump.

2.3.1 Experimental Setup

Figure 2-15 shows the experimntal setup of the pulsatile pump. The pulsatile pump in the current study consists of main devices such as a high-speed linear actuator, piston, linear variable displacement transducer (LVDT), an arduino board, solid-state relays, 3D printed parts, etc. The combination of the linear actuator and the piston, controlled by arduino, enables adjustable stroke volume and ratio of systole to diastole flow. The PA-15 high speed actuator [150] is compatible with a variety of control systems. This mechanical linear actuator operates by conversion of rotary motion of a screw shaft into linear motion. More information of the input voltage and current, load capacity and stroke length can be found in [150].

The linear variable differential transformer (LVDT) [151] is a type of electrical transformer used for measuring linear displacement of the linear actuator. In should be noted that the forward and backward movements of the linear actuator was possible using four solid-state relays. Solid-state relay (SSR) is an electronic device that can switch positive and negative ends of the circuit for the linear actuator. The existance of a coupling mechanism in the SSRs enables the control signal to activate this switch without mechanical parts.

Figure 2-16 shows the main pipe including the test section, a flexible rubber tubing, a flowmeter, pipes and connections. The test section consists of two glass tubes upstream and downstream of the valve, the St. Jude Regent Medical heart valve and 3-D printed aortic root sinuses.

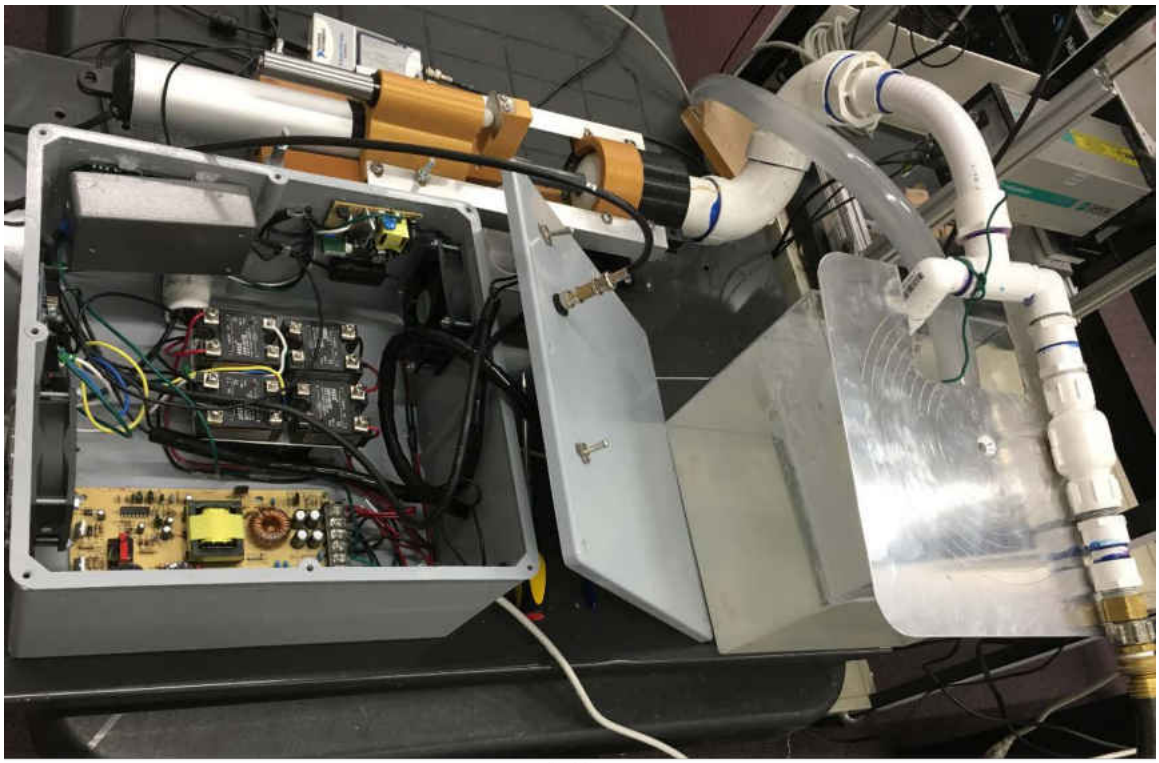

(a)

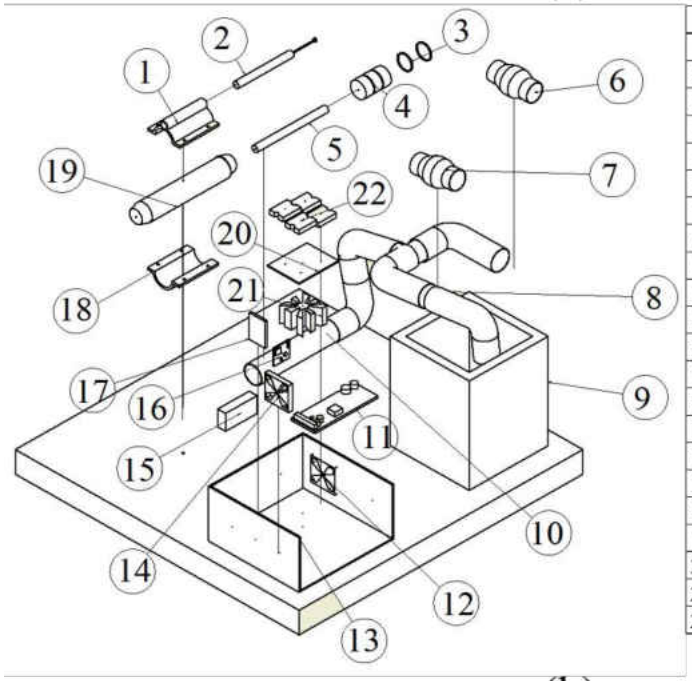

	Products
1	Top Holder for Linear Actuator
2	High Accuracy LVDT Displacement Sensors
3	O-rings for Piston
4	Piston
5	Piston Rod
6	Outlet check Valve
7	Inlet Check Valve
8	PVC Pipes
9	Water Reservoir
10	Cylinder
11	12 V Power Supply
12	Front Cooling Fan
13	Pump Control Box
14	Back Cooling Fan
15	LVDT Signal Conditioner
16	Arduino Power Supply
17	Arduino Board
18	Bottom Holder for Linear Actuator
19	High Speed Linear Actuator
20	Solid State relays Mounting Plate
21	Cooling Fan and Heat Sink for Solid State Relays
22	Four Solid State Relays

(b)

Figure 2-15 (a) Pulsatile pump setup including the linear actuator and pump control box; (b) Explode view of the main devices.

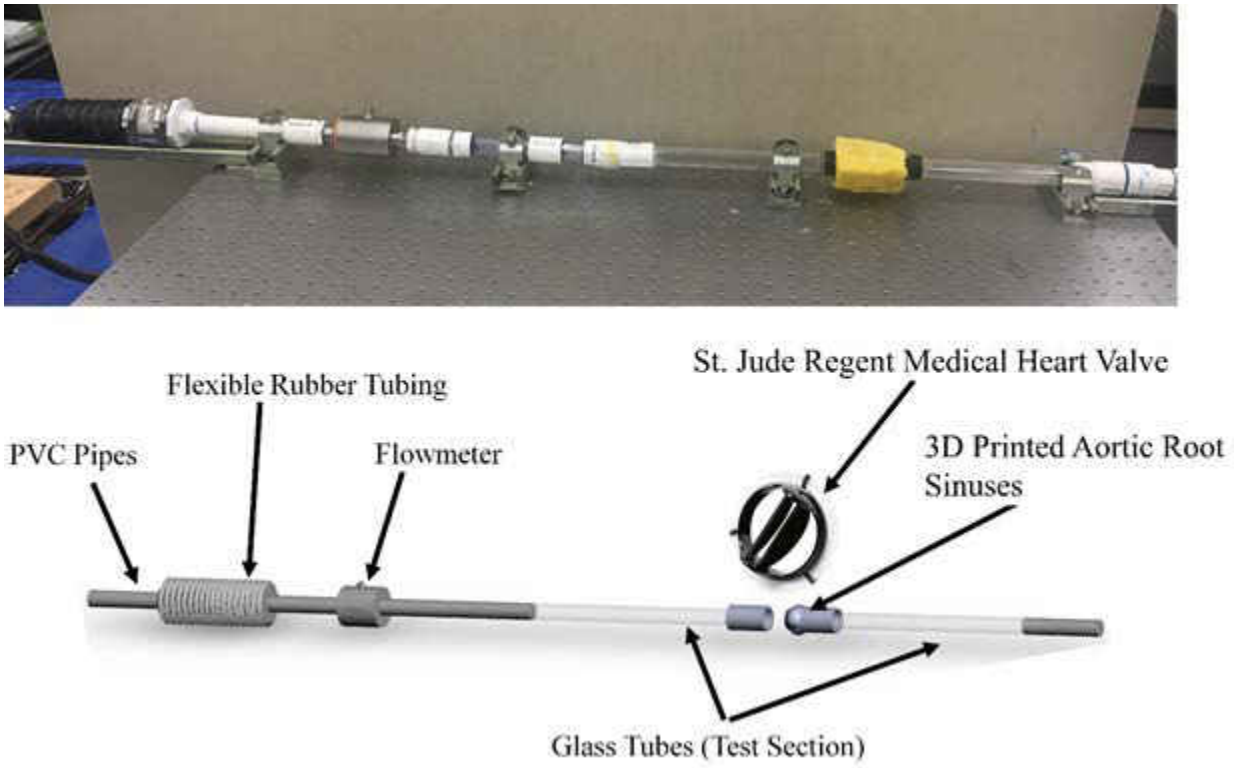

Figure 2-16 Main pipe and the test section of the experimental setup.

2.3.2 Flow Waveform Modeling

Figure 2-17a shows the target blood velocity waveform and displacement from left ventricle through the aortic heart valve [87]. The maximum velocity at the inlet is about 1 $m.s^{-1}$. The blood displacement in each pulse can be obtained by integrating the velocity profile. The maximum displacement occurs at the peak systole and equals to 20.32 cm. Figure 2-17b shows the desired linear velocity and displacement of the linear actuator. The linear velocity was calculated based on the heart valve and piston diameters. The diameters were 2.3 cm and 5.08 cm for the current St. Jude Regent Medical heart valve and pump piston, respectively.

The electronic Arduino board controls the operation of the linear actuaor. The operation of the linear actuator and the corresponding waveform (including the forward and backward movements)

can be modified using different codes. The code for this study can be found in APPENDIX II: ARDUINO CODE.

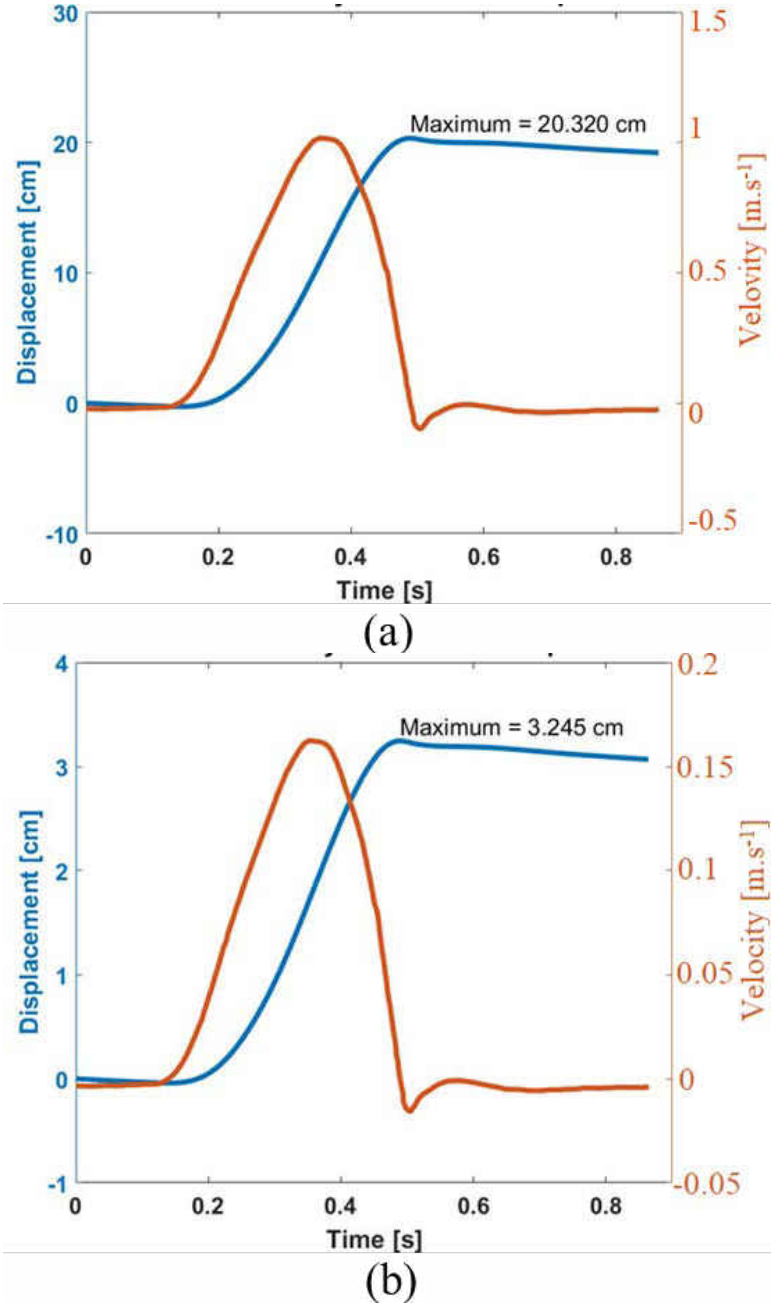

Figure 2-17 (a) Blood velocity and displacement profiles through aortic valve; (b) Desired velocity and displacement for the linear actuator.

Figure 2-18a shows the actual and desired displacements of the actuator. The trend for the actual actuator movement indicates the maximum displacement of 3.245 cm which is in the good

agreement with desired displacements. Figure 2-18b shows the displacement difference between the two cases. The maximum difference between the actual and desired displacements were about 0.05 cm. However, these differences in small fraction of time may results in higher differences in the velocity profiles. The dashed line in this figure shows the peak systole. After the peak systole, the actuator moves all the way back in order to fill the cylinder for the next pump. Therefore, the displacement difference was calculated from the beginning of the cardiac cycle up to the peak systole.

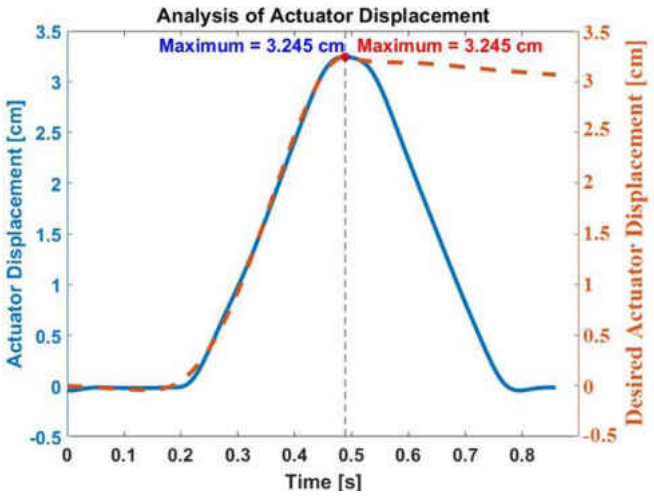

(a)

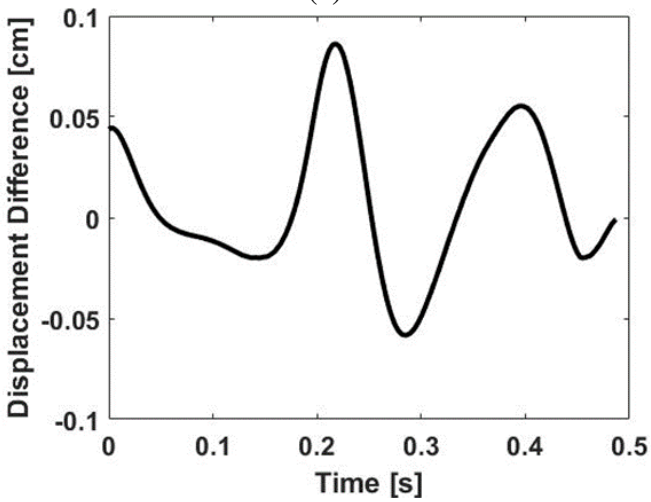

(b)

Figure 2-18 (a) Comparison of the actual and desired linear actuator movements. Dashed line shows the end of systole; (b) Difference between the actual and desired linear actuator movements till the end of systole.

Figure 2-19 shows the mean velocity waveform of one cardiac cycle in the test section upstream of the mechanical heart valve. The maximum velocity was about 0.9 m/s at the peak systole. Figure 2-19a shows the raw measured data using LDA; however, the waveform also includes the background noises such as the vibrations of the building in which the experiment was performed. It was found that these background vibrations consists of the frequencies close to 25 Hz, 40 Hz, and 50 Hz. Using a low-pass filter in MATLAB to remove the background noises, a smooth velocity waveform was achieved as shown in Figure 2-19b. As previously mentioned, the flexible rubber tube is a key part to control the flow waveform. Various flow waveforms can be created as the consequence of controlling the elasticity and resistance-to-flow of the system with this part.

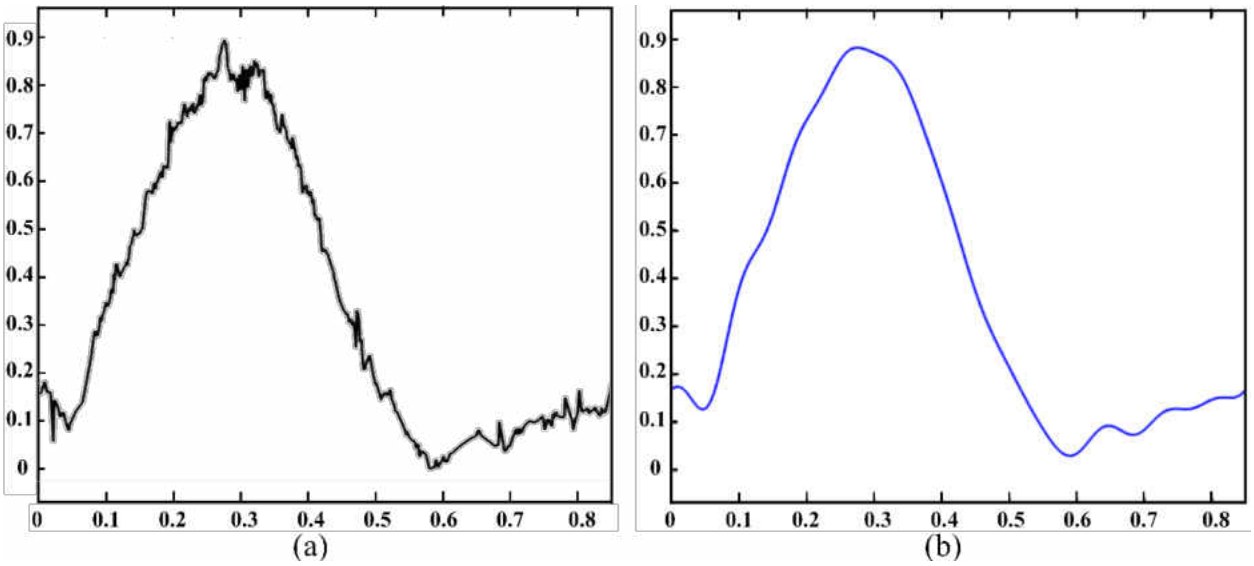

Figure 2-19 Velocity waveform upstream of the heart valve

2.3.3 Limitations

The purpose of this study was producing a programmable pulsatile pump that can develop any desirable flow waveform. The flexible rubber tubing (a bellow) had a significant role in creating the waveform. It was elastic and showed contraction and expansion influenced by the pulsatile

flow. Although this elasticity enables the backflow, similar to the elasticity of the artery walls, it caused a time delay in the fluid response to the actuator movements. Therefore, velocity measurements using LDA showed a cardiac cycle of longer duration than the desired cycle time. Removing the elasticity of the bellow helped achieving the desired cardiac cycle duration and maximum peak systole; however, the negative velocity (backflow) also disappeared. Hence, controling the elasticity in the system is a key factor to have a remarkable pulsatile pump capable of producing any flow waveform. On the other hand, the Arduino code was done based on the LVDT signal acquired by LabVIEW. The operation of this system can also be controlled completely by LabVIEW.

2.4 Modelling of Flow-Generated Sound

Acoustics (or, sound) is the study of the generation, propagation, absorption, and reflection of sound pressure waves in a fluid medium. The sound travels in space. Here, sound is the result of pressure variations (oscillations) in the elastic medium (blood, vessel wall, and tissue layer), generated by turbulent blood flow through the mechanical heart valve and the vibrating surface (internal side of the blood vessel wall.

In general, sound waves in any medium can be a mixture of longitudinal and shear waves, depending primarily on the boundary conditions.

Longitudinal Wave: Simplest type of wave is compressional (or longitudinal wave) where the particle oscillation is in the same direction as the energy transport. The disturbance propagates in the direction of the particle motion. This is the predominant mechanism in fluids and gases because shear stresses are negligible. For a longitudinal wave in an unbounded medium, sound travels at a speed of c:

$$\boldsymbol{c} = \sqrt{\frac{\boldsymbol{E}}{\boldsymbol{\rho}}} \tag{2-37}$$

where, E = Young's modulus for a solid material, or the bulk modulus for a fluid; ρ= density of the material.

Shear Wave: The particle motion direction is orthogonal (perpendicular) to direction in which the disturbance (and the energy) propagates.

Numerical modelling of flow-generated sound is often referred as Computational Aeroacoustics (CAA) modelling. Although the term "Aeroacoustics" indicates airflow, same techniques can be implemented for liquids, which may be termed hydroacoustics. CAA methods can be classified in to two groups, namely direct and hybrid methods. The direct method solves the compressible Navier-Stokes equations and together computes flow and acoustic solutions while hybrid approaches compute acoustics separately using the results from flow computation.

2.4.1 Direct Method

The acoustic field in a fluid flow can be fully computed through compressible Navier-stokes equations. Such a computation will include the sound generation, propagation as well as the interaction between acoustic and flow fields. Hence, a compressible CFD simulation can be used to solve acoustic problems and such methods are referred as direct CAA methods. However, direct methods have certain issues that hybrid CAA methods are often preferred over direct CAA methods. Some of these limitations are described below.

Low time step requirement due to length scale differences: length scales of the flow vary from the Kolmogorov length scale l_k to the large eddy scale L. Length scales in the acoustic domain are related to the acoustical wave length ƛ which is much larger than l_k. To accurately capture the sound sources, CFD mesh should be in the order of l_k in the source regions. For the solutions to be stable Courant–Friedrichs–Lewy (CFL) number in both flow and acoustic domains should be kept to a small value (typically less than unity for explicit differencing schemes).

$$CFL_{CFD} = u.\frac{dt}{\nabla x} \tag{2-38}$$

$$CFL_{CAA} = c.\frac{dt}{\nabla x} \tag{2-39}$$

Equation 2-37 and 2-38 show the CFL numbers for flow and acoustic problems respectively, where u is the flow velocity and c is the wave velocity which is close to the sound velocity in a fluid. As, c is much greater than, the time step dt should be maintained at a very low value for both domains. Considering the grid size ∇x is same for both domains. Hence, excessive computational power is needed for the simulations.

Energy differences: The energy levels in the acoustic field are much smaller compared to the flow field. For low Mach number (M) flow, this difference increases since the acoustic power is in the range of M^3 and M^4 [152]. When the acoustic variables are too small, numerical errors in the simulation can interfere with acoustic results. Hence, numerical error should be maintained much smaller than the acoustic variables, which takes extra computational effort.

Boundary conditions: The boundary conditions for CFD simulation generates spurious numerical reflections in the acoustic domain [152], since both flow and acoustics are solved in the same simulation. Hence, special modifications are needed for CFD boundary conditions, to reduce these spurious effects on wave propagation.

2.4.2 Hybrid Method

In the hybrid method, acoustics parameters can be computed separately after flow computation is done. One of the available approaches is the combined usage of the CFD software ANSYS Fluent [92] and the vibration and acoustics simulation tools of ANSYS Mechanical [92] for the specific application of this study, which is to calculate the blood flow sound caused by the turbulent flow through the bileaflet mechanical heart valve. More discussion about the proposed sound analysis method is included to CHAPTER 4: SOUND ANALYSIS.

CHAPTER 3: HEMODYNAMICS OF A BILEAFLET MECHANICAL HEART VALVE

3.1 Valve Modeling

The heart valve geometry (Figure 3-1a) was modelled based on St. Jude Medical and Regent Medical heart valves [7,25] and chosen to be similar to previous studies [1, 2]. An enhancement implemented in the current study (compared to some previous two-dimensional CFD studies) was to include the valve housing (or, valve ring) to the model. Here, the BMHV is in the fully open position and divides the flow into three orifices: two of them (top and bottom orifices) are roughly semicircular and the third (middle orifice) is almost rectangular. In addition, a realistic geometry of the aortic sinuses was created since it is important for appropriate flow field analysis [3, 4]. Figure 3-1b shows the asymmetric aortic sinuses geometry with inlet aortic root diameter of d = 0.023 m, which was extracted from angiograms [5].

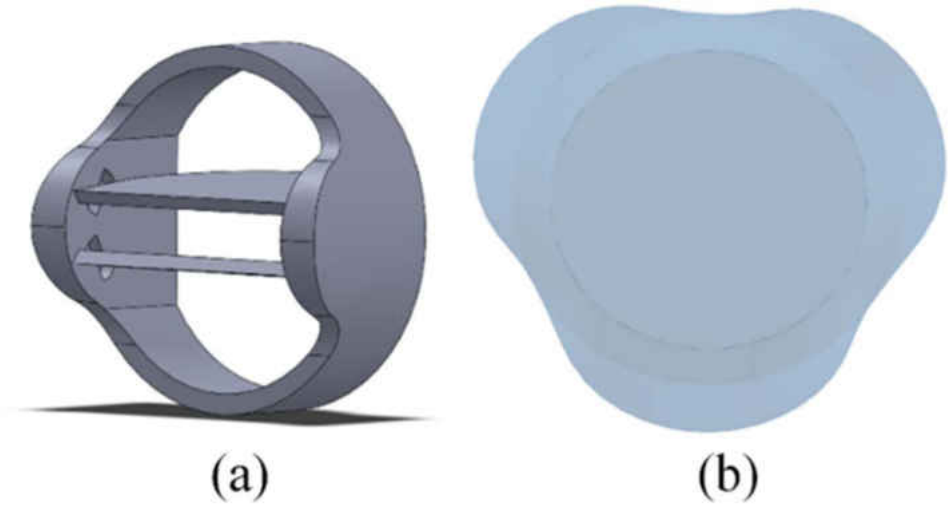

Figure 3-1 (a) A bileaflet mechanical heart valve modelled based on St. Jude Medical and Regent Medical heart valves [7,25]; (b) Front view of the aortic root sinuses similar to the geometry which was extracted from angiograms [57].

The importance of the flow field through the hinge region to valve performance was emphasized by the unsuccessful clinical trials of earlier bileaflet heart valves [153]. The sudden expansion and contraction zones characteristic of their valve hinge recess increased the unsteady flow, vortex, and stagnation regions which were found to be associated with turbulent shear stresses up to 8,000 dyne.cm^{-2}, which is greater than the accepted threshold level of blood cell damage [41,42,154,155]. Figure 3-2 shows the butterfly-shape hinge design, including the hinge recess (Figure 3-2a), for St. Jude Regent Medical valves (Figure 3-2b) with smooth contours. Figure 3-2c shows the simplified geometry of the hinge design. An inherent feature of bileaflet mechanical heart valves is the hinge recesses about which the leaflets pivot. The SJM hinge geometry is characterized by a streamlined butterfly geometry with smooth contours which minimize flow separation and stagnation.

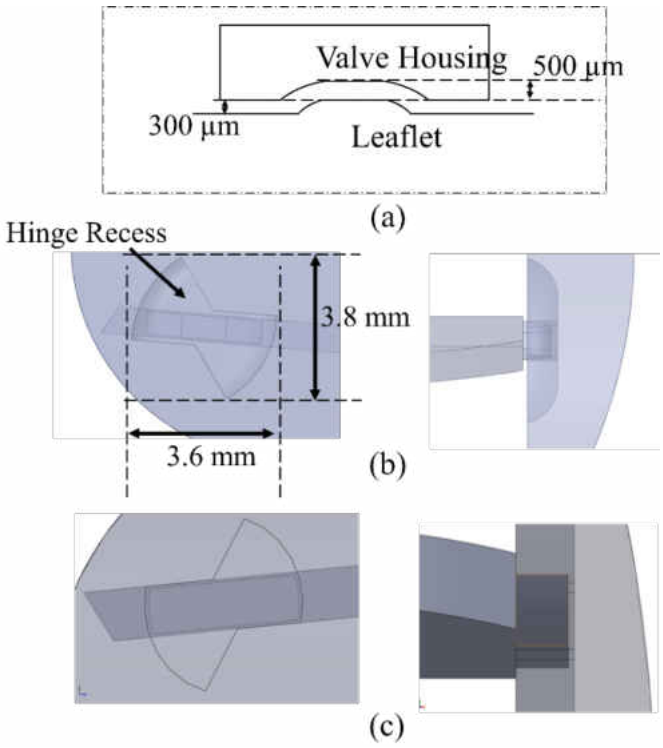

Figure 3-2 Heart valve hinge dimensions characterized by its butterfly shape; (a) Hinge recess and the gap in the hinge region; (b) St. Jude Regent Medical heart valve hinge design with smooth contours; (c) Simplified heart valve hinge design with less smooth contours.

In contrast to some of the other valve designs, the St. Jude Medical (SJM) bileaflet mechanical heart valves has exhibited low thrombosis rates and good clinical performances and are currently the two most commonly implanted prosthetic heart valves [153]. In-depth studies have shown that the flow fields within the constricted hinge region are critical to the proper function of the valves, since the hinge geometry directly influences the valve durability, functionality, fluid dynamics, and thrombus formation [156].

3.2 Fluid Dynamics of the Bileaflet Mechanical Heart Valves

Dynamic Fluid Body Interaction (DFBI) module simulates the motion of a rigid body in response to pressure and shear forces the fluid exerts. This module calculates the resultant force and moment acting on the body due to all influences, and solves the governing equations of rigid body motion to find the new position of the rigid body using a 6-DOF Solver [150]. The 6-DOF Solver computes fluid forces, moments, and gravitational forces integrates them over the surfaces of the 6-DOF bodies. For rigid bodies, it is sufficient to model the motion of the center of mass of the body alone. The relative motion of any other part of the body can be extrapolated from this center of mass. Moreoever, it is necessary to know the moments of inertia of the body about a fixed reference point (which is normally the center of mass) before the rotational motion can be known. Also, the center of rotation was set to the center of the leaflet hinge for 1-DOF rotation. For time integration, the 6-DOF solver employs a trapezoidal scheme of second order accuracy. This order of accuracy is independent of the order of accuracy of the implicit unsteady solver. Simulating the motion of multiple objects (here, top and bottom leaflets) was acheived by discretizing the computational domain with several different meshes that overlap each other. This approach is known as overset mesh which is most useful in problems dealing with multiple or moving bodies, as well as optimization studies. The overset meshes for top and bottom leaflets

were created using the overset mesh boundary, which is the outer boundary of the overset region that is expected to be coupled with the background mesh. The overset mesh interface wal also used to couple the overset regions with the background region. Figure 3-3 shows the 3D prospective and cross-sectional views of the flow domain and overset meshes.

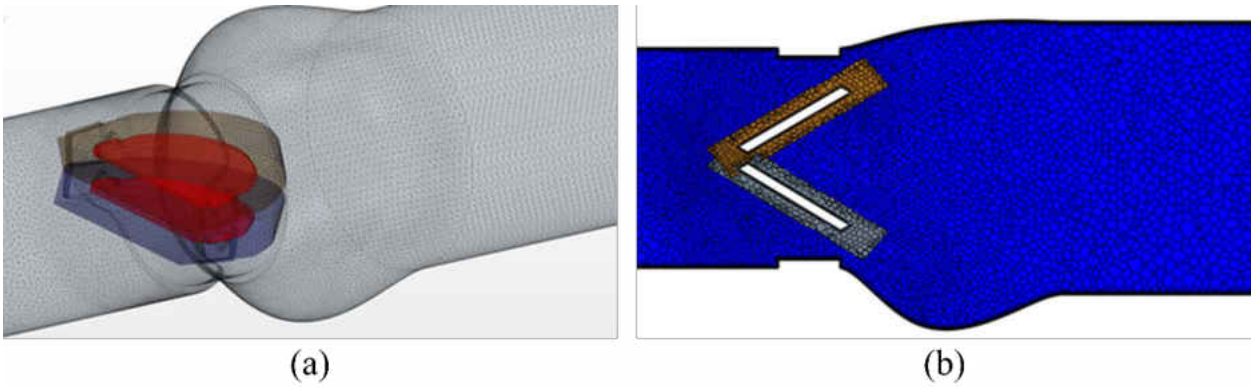

Figure 3-3 Dynamic fluid body interaction (DFBI) and overset mesh around the moving leaflets, (a) 3D prospective view; (b) cross-sectional view.

The following normal aortic physiologic flow conditions were imposed: peak flow rate of approximately 25 L/min, systolic duration of one-third of the cardiac cycle, a cardiac cycle of 860 ms, and a heart rate of 70 beats/min. The velocity fields and leaflet position calculated with the large-scale FSI solver during systole were found to be in excellent agreement with Particle Image Velocimetry experimental data published by Dasi et al. [11,87]. The CFD analysis was performed for a pulsatile flow through a three-dimensional BMHV. The inlet velocity corresponded to cardiac output of 5 L.min^{-1} and heart rate of 70 bpm with a systolic phase duration of 0.3 s (Figure 3-4). The peak inflow velocity was about 1.2 ms^{-1}. The density and dynamic viscosity of blood were set to ρ = 1080 kg.m^{-3} and μ = 0.0035 Pa.s, respectively. This lead to an inlet peak Reynolds number ($Re_{peak} = {\rho U_{peak} d_{inlet}}/{\mu}$) of 8516 and a Womersley number ($W_o = {d}/{2}\sqrt{{\omega\rho}/{\mu}}$) =

26.5; where, $\omega = {}^{2\pi}/_{T} = 17.21\ \text{rad.}\,\text{s}^{-1}$, is the frequency of pulsatile flow and T= 0.866 s is the period.

It is important to note that the DFBI Six-DOF solver was frozen for the initial two cycles, as shown in Figure 3-4. Then, the solver was activated; however, a motion limit was assigned for the leaflets in order to prevent sudden large displacements, and consequently, the solution divergence. This approach also helps the flow to reach its periodicity. The leaflets were able to move in their complete range of rotation in the 7th and 8th cardiac cycles at which the results were analyzed.

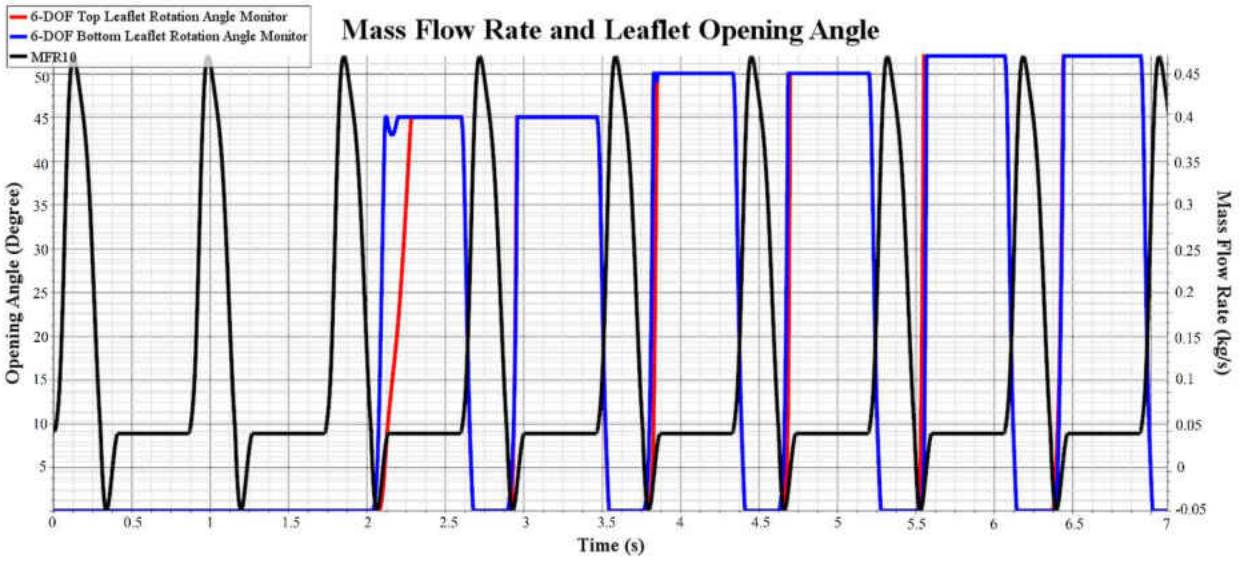

Figure 3-4 Mass flow rate and leaflet opening angle for a cardiac cycle of 0.860 s.

Figure 3-5 shows the velocity distributions in opening phase of the valve leaflets during the systole. The blood flow exerts forces on the two leaflets in the acceleration period time until they reached their fully open position at 0.06 s of the cardiac cycle. The reaction forces on the blood components may increase the risk of blood damage. The peak flow happens at 0.09 s at which the maximum velocity was about 2.1 m.s^{-1}, seen in the middle orifice. In the deceleration period time, the blood flow slowed down and has an inlet inflow of 0 m.s^{-1} at the end of the systole (0.3 s). This

causes the emergence of small vortical structures with high fluctuations downstream of the valve. Blood elements trapped in recirculation regions may experience exposure times as long as the entire forward flow phase duration.

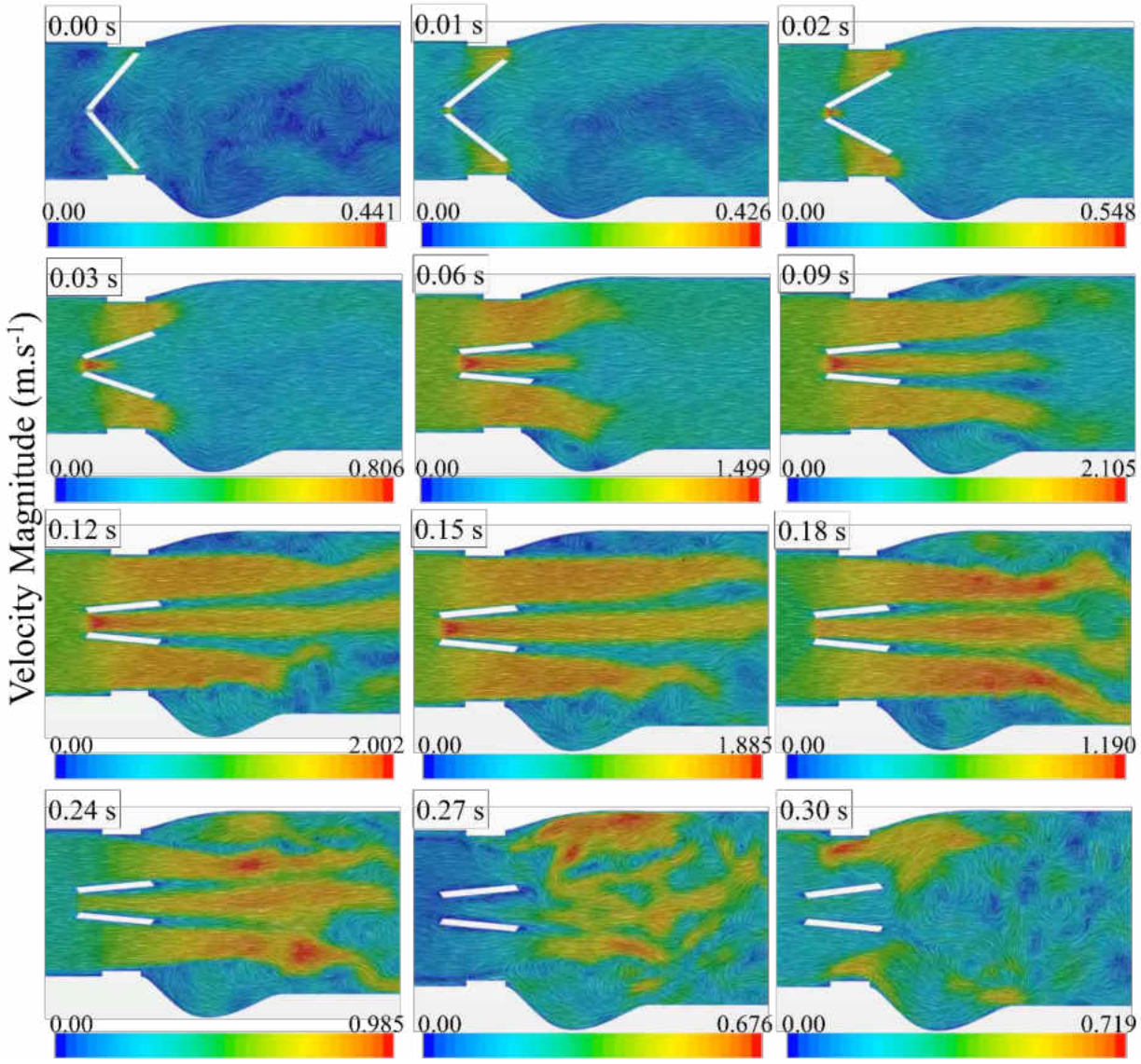

Figure 3-5 Valve leaflet opening phase during the systole (0-0.3 s).

Mechanical heart valves rely on reverse flow to close their leaflets. Figure 3-6 shows the velocity distributions in valve leaflet closing phase during the diastole. Blood flows back through the valve as the leaflets are closing. This phenomenon is known as water hammer effect. The

leakage flow structures can also be seen when the leaflets are fully closed from the gap between the leaflets and valve housing. It is interesting that the backflow velocity raised up to about 3.6 $m.s^{-1}$ along with high fluctuations which are higher that the velocity magnitude at the peak systole.

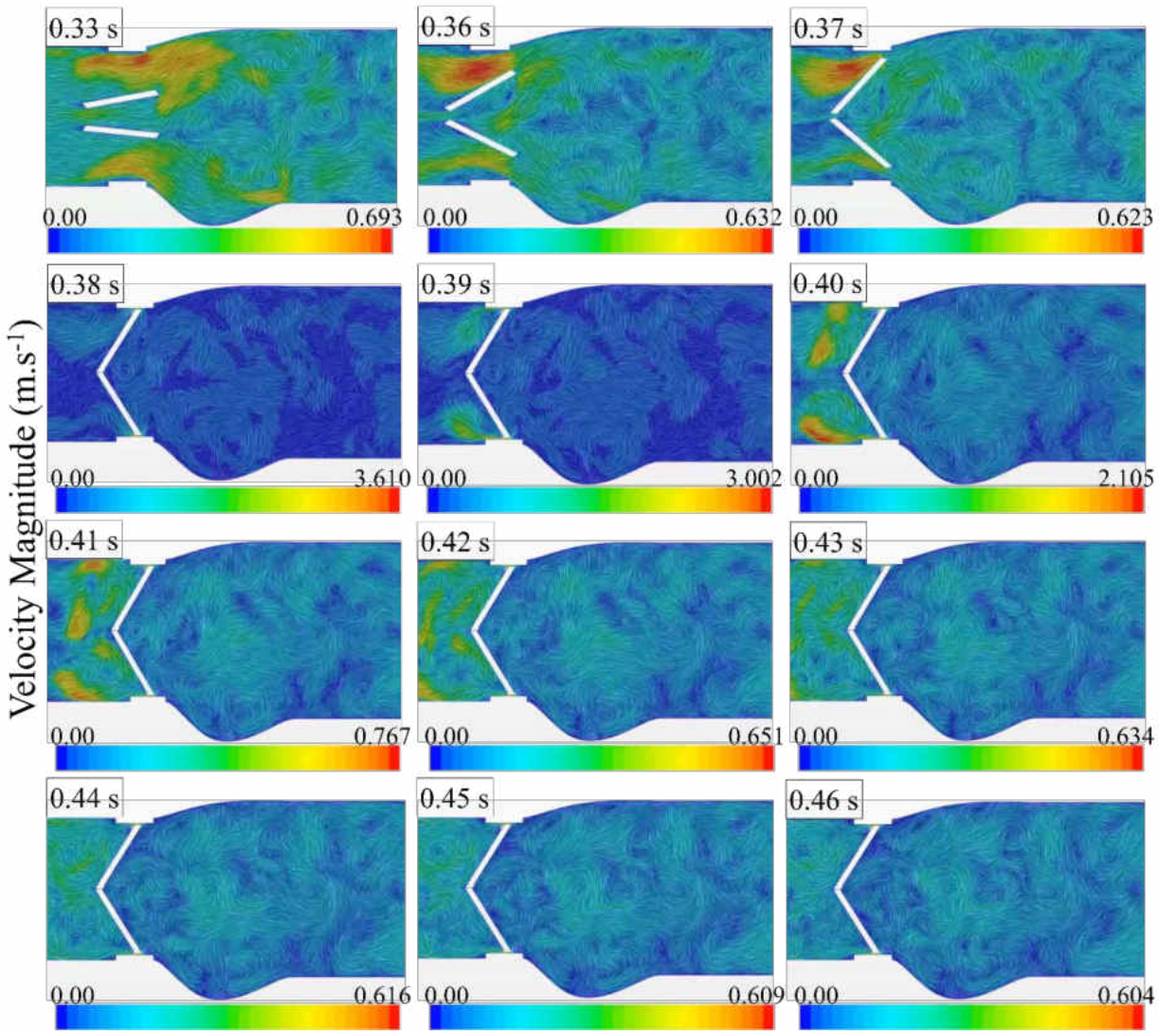

Figure 3-6 Valve leaflet closing phase during the diastole.

A detailed view of the blood flow leakage through the gaps between the leaflets and the housing as well as the hinge regions are depicted in Figure 3-7 by the instantaneous velocity snapshots. Under pulsatile conditions, these strong leakage jet were mostly seen to appear right at the moment of valve closure. This flow which is driven through the narrow hinge regions by a large cross-

valvular pressure gradient, produces elevated flow velocities and high turbulent shear stresses that may lead to hemolysis and initiation of the coagulation cascade. A previous investigation of the 25 mm SJM standard design under mitral conditions by Ellis [157] showed similar peak leakage velocity and turbulent shear stress within the hinge of the current model of 23 mm SJM Regent design under aortic conditions. As the hinge region of a mechanical bileaflet valve is implicated in blood damage and initiation of thrombus formation, detailed fluid dynamic analysis in the complex geometry of the hinge region during the closing phase of the bileaflet valve help understand the effect of fluid-induced stresses on the activation of platelets.

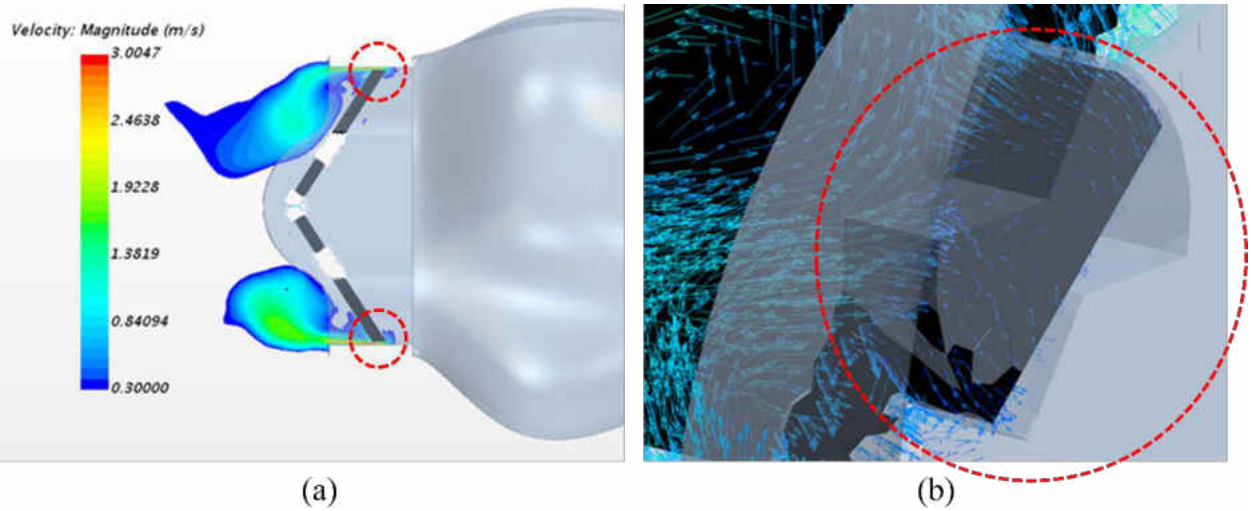

Figure 3-7 (a) High-velocity blood Regurgitation through the gaps between the leaflets and the valve housing; (b) Leakage driven through the narrow hinge regions by a large cross-valvular pressure gradient which produces turbulent shear stresses with high exposure time.

3.3 Heart Valve Dysfunction (Patient-Specific Condition I)

3.3.1 Simulation Setup

In the current study, a normal functioning (0% dysfunction) and a BMHV with different levels of dysfunction were simulated using a commercial CFD software package (STAR-CCM+, CD-adapco, Siemens, Germany). Figure 3-8a shows the side cross section of the BMHV with a top functional leaflet and a bottom dysfunctional leaflet at 0, 25, 50, 75 and 100% levels of

dysfunctionality (corresponding to a gradually decreasing effective orifice area (EOA)). In addition, Figure 3-8b shows the leaflet hinges as well as direction of net pressure, shear forces (F_p and F_τ, respectively), and moments (Ω) acting on the leaflets.

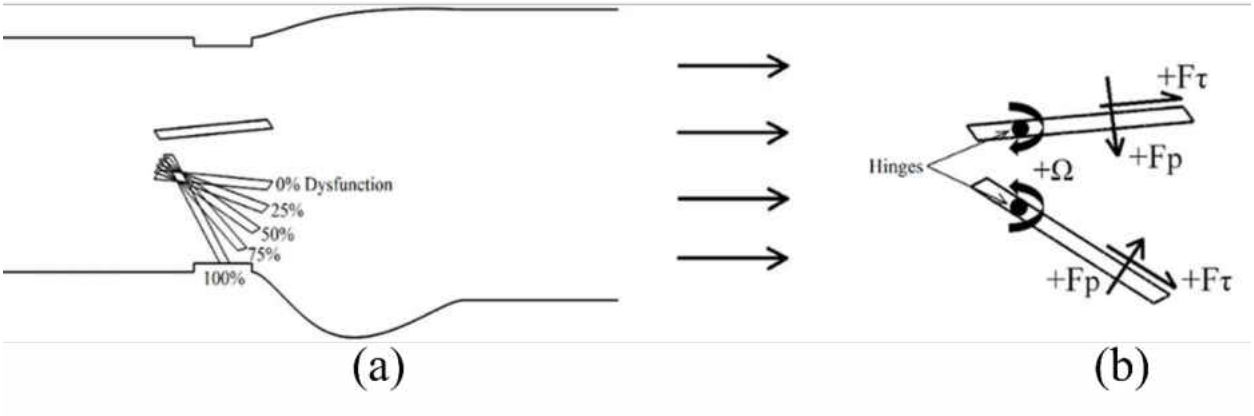

Figure 3-8 (a) Degrees of bottom leaflet dysfunction; and (b) Sign conventions for forces acting on the leaflets.

The low-Reynolds SST k-ω turbulence model [6, 7], which is known to perform well for internal flows, was used to simulate the flow during a complete cardiac cycle. Since the current study focuses on the fully opening period from 60 to 250 ms [8], the dynamics of the leaflet opening and closure were not simulated as done in previous studies [9, 10, 11]. The unsteady simulation was performed with a time step of 0.5 ms and 25 iterations per time step. Numerical solution typically converged to residuals about $< 10^{-4}$. Moreover, high quality polyhedral mesh was generated in the flow domain, especially in the heart valve and aortic sinuses regions (Figure 3-9). The y^+ was maintained less than 1 close to all walls including leaflet surfaces ($y^+ = 0.46$ at the peak flow).

Figure 3-9 High quality polyhedral mesh generated (a) close to the wall and leaflet surfaces and, (b) in the flow domain.

3.3.2 Numerical Uncertainty

Steady flow simulation was conducted to establish grid density prior to unsteady simulation. The uncertainty and error in the study was calculated following ASME recommendations [12]. Figure 3-10a shows velocity profile at the entrance of the aortic sinuses along with the corresponding error bars while Table 3-1 shows the discretization error of the maximum velocity value in the entire field.

Table 3-1 Calculation of discretization error

φ = Maximum velocity in the entire field (m/s)			
N_1; N_2; N_3	6,529,062; 2,598,513; 1,390,150		
r_{21} (Refinement factor of N_2/N_1)	1.35	e^{21}_a	0.11%
r_{32} (Refinement factor of N_3/N_2)	1.32	e^{21}_{ext}	0.11%
φ_1	2.523	GCI^{21}_{fine}	0.14%
φ_2	2.521	φ^{32}_{ext}	2.515
φ_3	2.526	e^{32}_a	0.21%
p	2.289	e^{32}_{ext}	0.24%
φ^{21}_{ext}	2.526	GCI^{32}_{course}	0.29%

The fine-grid convergence index (GCI_{fine}) in Table 3-1 was 0.139% (excluding modeling errors [12]). In addition, the maximum discretization uncertainty was approximately 7% in the area close to the leaflets (Figure 3-10b). These numerical uncertainties are comparable to previous studies [9].

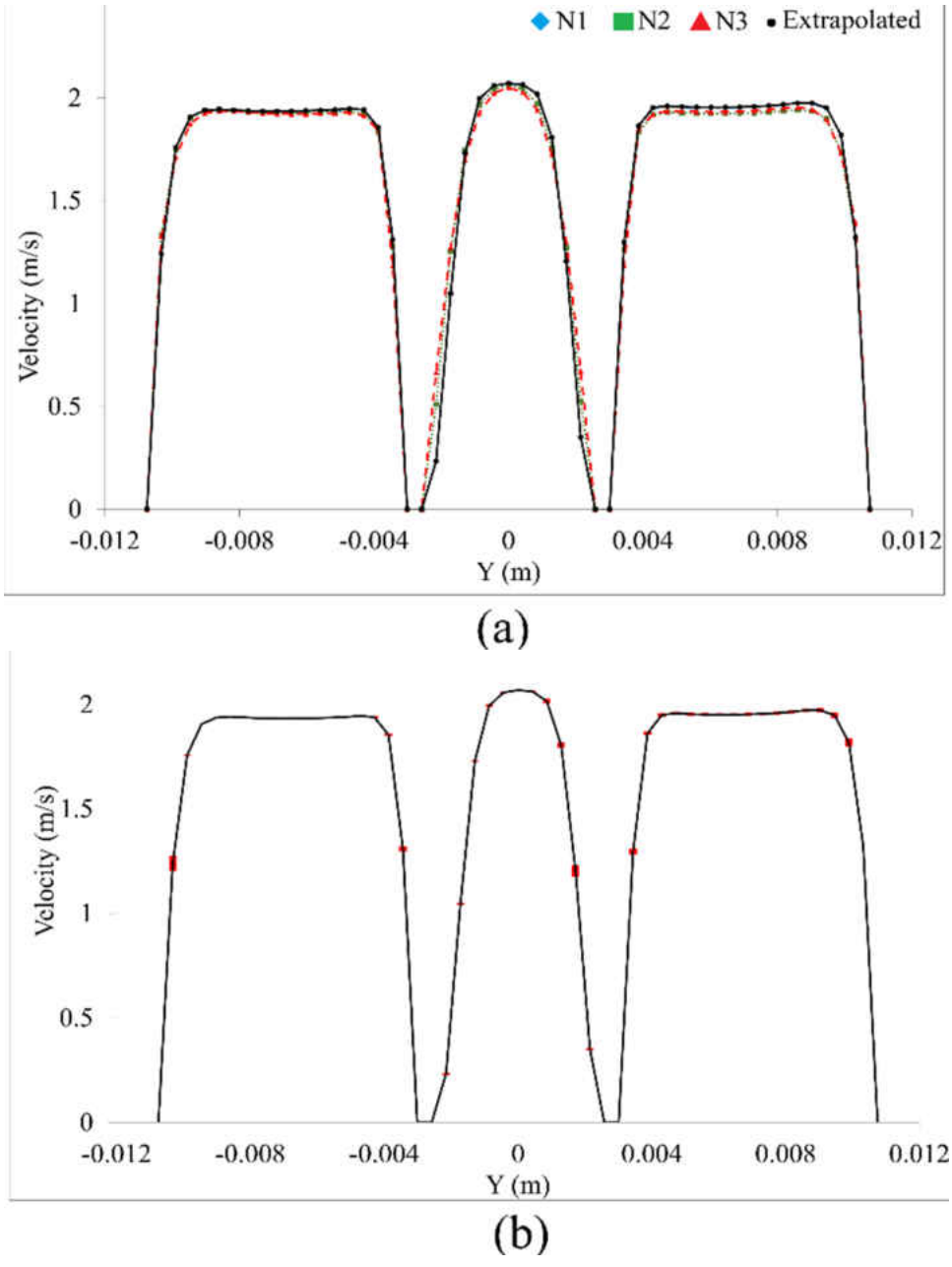

Figure 3-10 (a) Velocity profile at the entrance of the aortic sinuses for different grid solution; (b) Fine-grid solution with discretization error bars.

3.3.3 Validation

The normalized velocity profile along a line located 7 mm downstream of the healthy valve (at the peak systole) is shown in Figure 3-11a for a normal functioning valve. The velocity profiles obtained in previous studies that considered similar geometries and flow conditions [11, 13] are also shown in the same figure. Here, normalized velocities are plotted to facilitate comparison with studies that reported normalized profiles [11]. The maximum velocities were compared for steady cardiac outputs of 5 and 7 $L.min^{-1}$. These velocities were 0.96 ms^{-1} and 1.35 ms^{-1} in the current study, respectively, which were comparable to maximum velocities of 1.0 ms^{-1} and 1.36 ms^{-1} reported in the previous study [11]. To quantify the difference between our computational results and the previous experimental results [13], the root-mean-square (RMS) of the velocity differences among the two studies were calculated. The RMS of the velocity difference was 6.58% of the maximum velocity, suggesting agreement between the results of the current study and measured values. The normalized velocity profile was also compared with two other experimental and computational studies at the trailing edge of the leaflet and 105 ms after the peak systole [14, 7] (Figure 3-11b). The RMS of the velocity difference was < 6% of the maximum velocity, suggesting agreement with these studies.

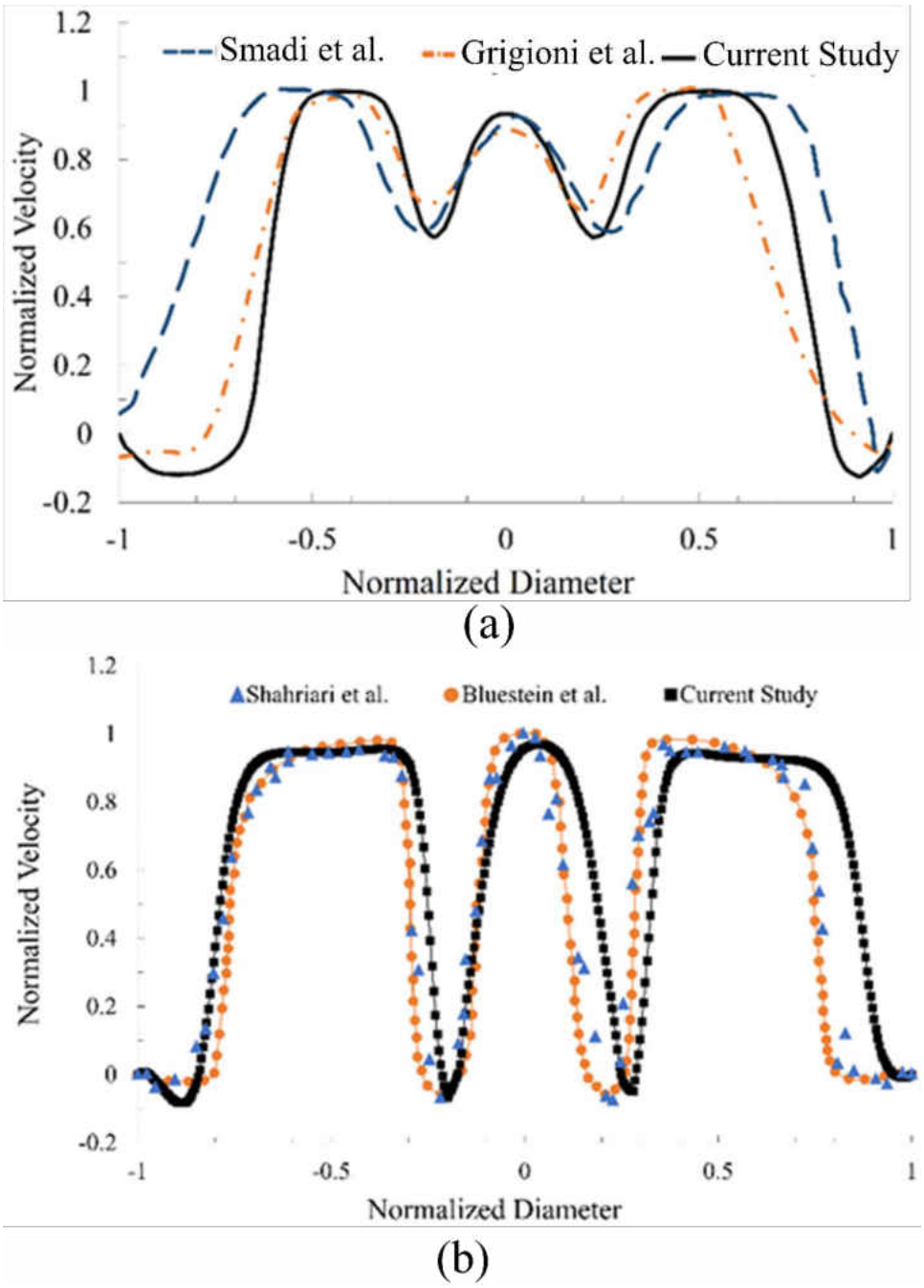

Figure 3-11 (a) Normalized velocity profiles at 7 mm downstream of the valve (at the peak systole) in the current study compared to previous experimental [158] **and computational [90] studies. More agreement can be seen between the current and the experimental study; (b) Normalized velocity profiles at the trailing edge of the leaflets (105 ms after the peak systole) in the current study compared to previous experimental [88] and computational [31] studies.**

High turbulent shear stress levels at the valve hinges and downstream of the valve can lead to thrombus formation and the leaflets' motion restriction [15, 16]. This, in turn, may lead to a life-

threatening dysfunction of one or both leaflets of BMHVs [17]. Blood complications, in overall, mostly occurred at the valve ring and hinge area and impaired the movement of both leaflets. Montorsi et al. [18] concluded that the distinction between blocked and hypomobile leaflet is vital. On the other hand, the peak velocity and the position of the maximal velocity at valve orifices were determined as the best predictors of dysfunctional valve leaflets [9, 19]. Fortunately, many of these complications can be prevented or minimized with careful medical management and periodic monitoring of valve function. Prompt recognition of valve dysfunction allows early treatment [20], where CFD can play a significant role in this case. For example, blocked leaflets could be fully recovered when valve thrombosis is detected early [18].

3.3.4 Velocity and Turbulent Kinetic Energy

Figure 3-12a shows a cross-sectional view of the velocity at t = 90 ms, where the color represents the magnitude and the short lines indicate direction. For 0% dysfunction (Figure 3-12a1), the flow appeared to be more uniform; especially compared to cases with dysfunctional leaflets (Figure 3-12a2 to 5a5). Figure 3-5a1 also shows relatively small increase in velocity in the orifices and wake regions downstream of the leaflets as would be expected. As the bottom leaflet dysfunction took place, the velocity magnitude in the orifices increased. This may be because of the narrowing of bottom orifice with dysfunction, which led to flow area reduction. Flow separation in the middle orifice was observed around the leading edge of the bottom leaflet for dysfunctionalities of 25-100% (Figure 3-12a2 to 5a5). Separation also occurred close to the trailing edge of the top leaflet for 75% and 100% (Figure 3-12a4 and 5a5). In addition, Figure 3-12a shows a trend of increasing separation bubble size with dysfunctionality. Although not clearly shown in the figure, vortex shedding was also observed. While Figure 3-12 shows

information for t = 90 ms, flow structures were also examined for all times between 60 to 250 ms and were found similar to those shown in Figure 3-12.

Figure 3-12b shows the turbulent kinetic energy (TKE), which is indicative of velocity fluctuations. TKE tended to increase with dysfunction and a region of higher TKEs around the top leaflet started to develop when dysfunction reached ≥ 75%.

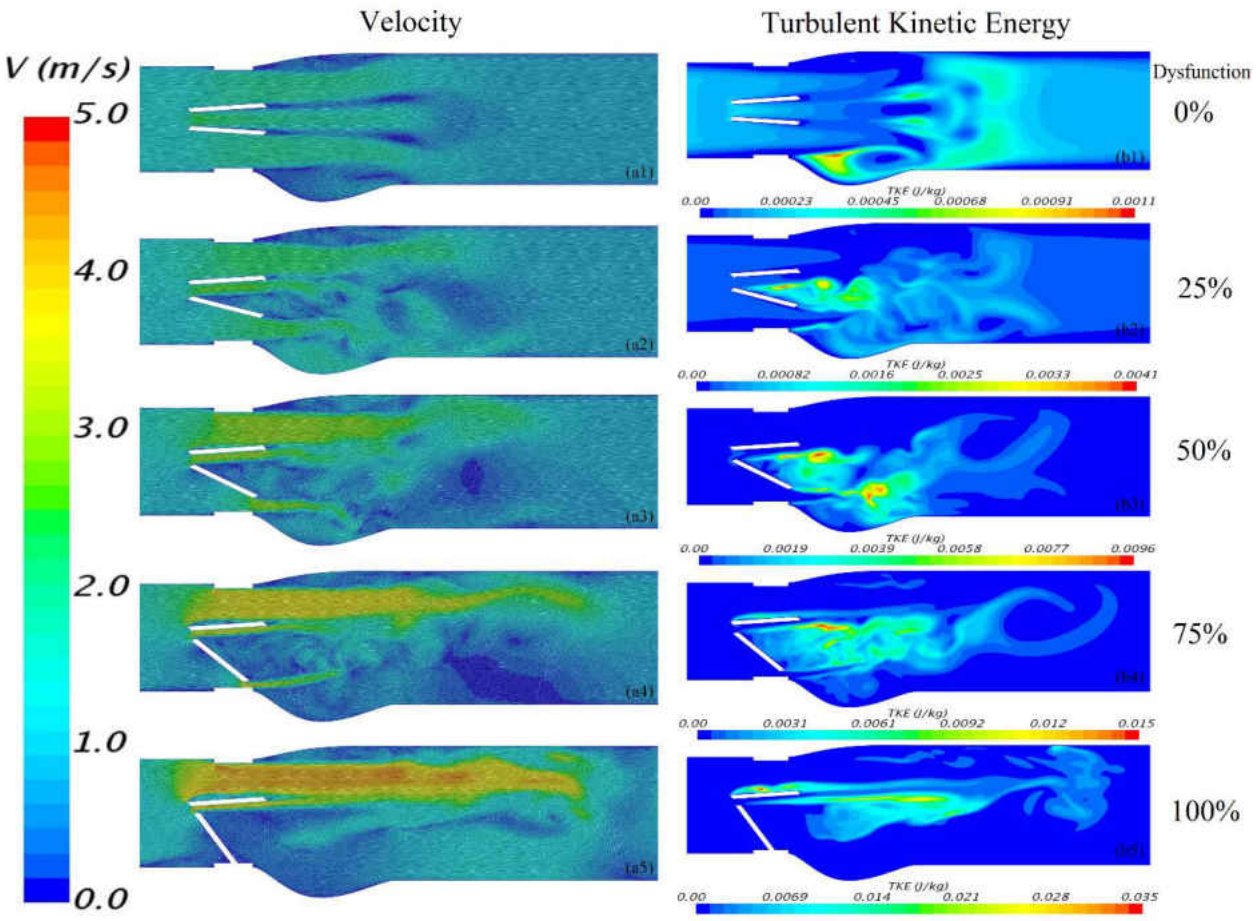

Figure 3-12 Velocity and turbulent kinetic energy at 90 ms for different degrees of lower leaflet dysfunction. There was a general trend of increased maximum velocity and TKE with increased dysfunction. (Note that the scale for TKE increased with dysfunction).

3.3.5 Streamline and Vorticity

Figure 3-13a1 to 6a5 shows the streamlines at the peak systolic time of 90 ms, where the color represents the velocity magnitude. For 0% dysfunction (Figure 3-13a1), the blood flow seemed to

have a narrower velocity range (i.e. more uniform velocity) compared to the higher levels of dysfunction (Figure 3-13a2 to 6a5). Figure 3-13a1 also shows relatively smaller flow separation in the wake region downstream of the leaflets as would be expected. The flow reattachment also happened closer to the exit of the aortic sinuses. The velocity magnitude in the orifices increased, especially in the bottom orifice, as leaflet dysfunction increased. Figure 3-13 also suggests that an increased leaflet dysfunction may increase the potential for development of higher levels of disturbances in the flow and possibly increased turbulence. This data also suggested that more intense vortical structures start to appear in the valve and sinus regions during the acceleration phase (e.g., 60 to 90 ms). Figure 3-13b1 to 6b5 shows vorticity at different levels of dysfunction. Vorticity increased with dysfunctions and spread downstream of the leaflets. Conversely, lower levels of vorticity occurred in the sinus downstream of the dysfunction leaflet at 100% dysfunctions, which can be because the obstruction caused by the dysfunction created a low velocity region behind that leaflet. While Figure 3-13 shows information for t = 90ms, flow structures were also examined for all times between 60 to 250 ms and were found similar to those shown in Figure 3-13. Higher velocities and flow separation at the leaflet surfaces were accompanied by growing eddies and vorticity downstream of the valve (Figure 3-13).

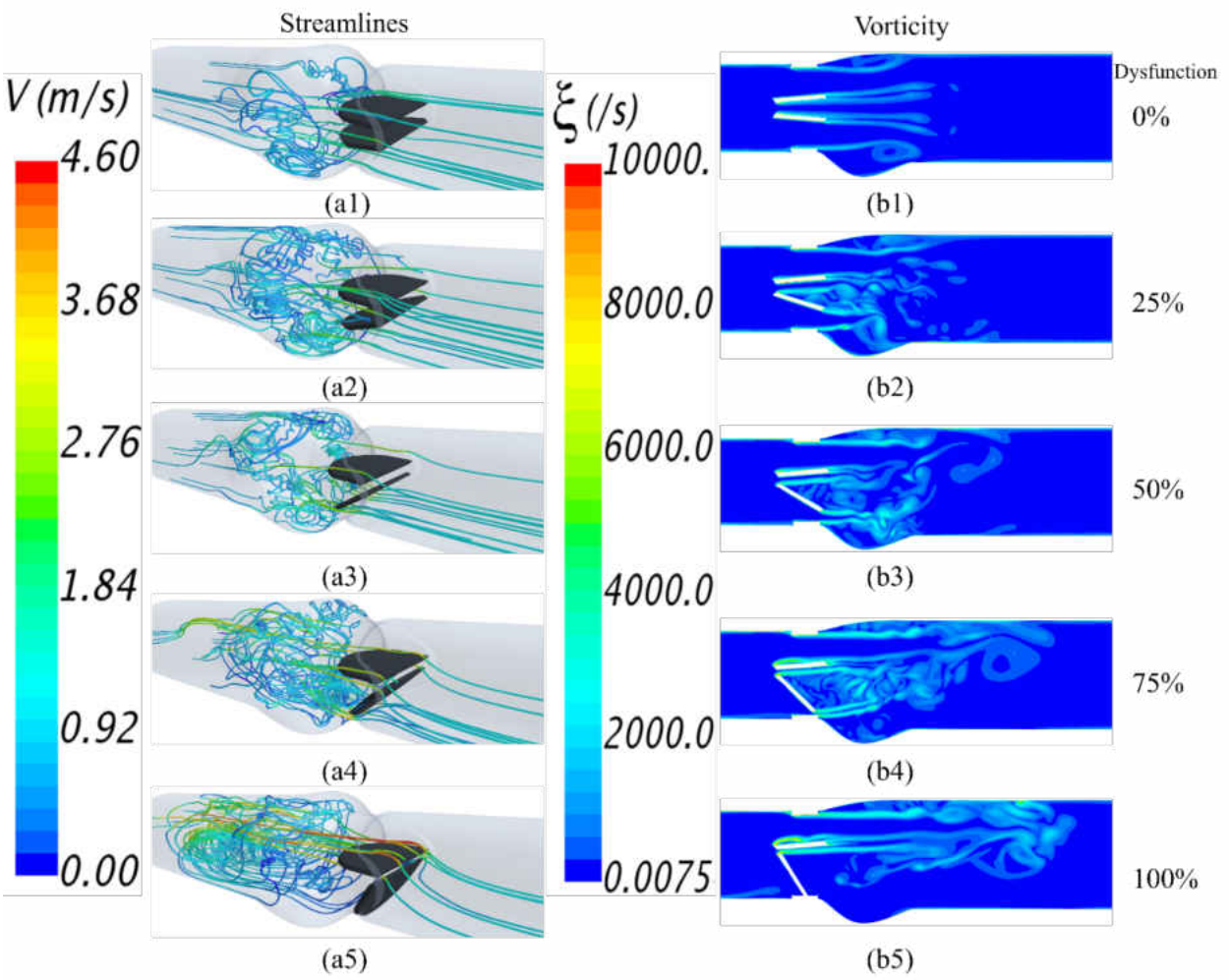

Figure 3-13 Flow field around the valve: (a) Streamlines; (b) Vorticity

3.3.6 Wall Shear Stresses

Figure 3-14 shows the distributions of wall shear stress (WSS) on aortic sinuses at different levels of dysfunctions at the peak systolic phase. The highest wall shear stresses occurred at the 50% dysfunction followed by 100%, 75%, 25% and 0% dysfunctions, respectively. At 75% and 100% dysfunctions, wall shear stresses on the sinus downstream of the bottom leaflet decreased possibly due to flow obstruction by that leaflet.

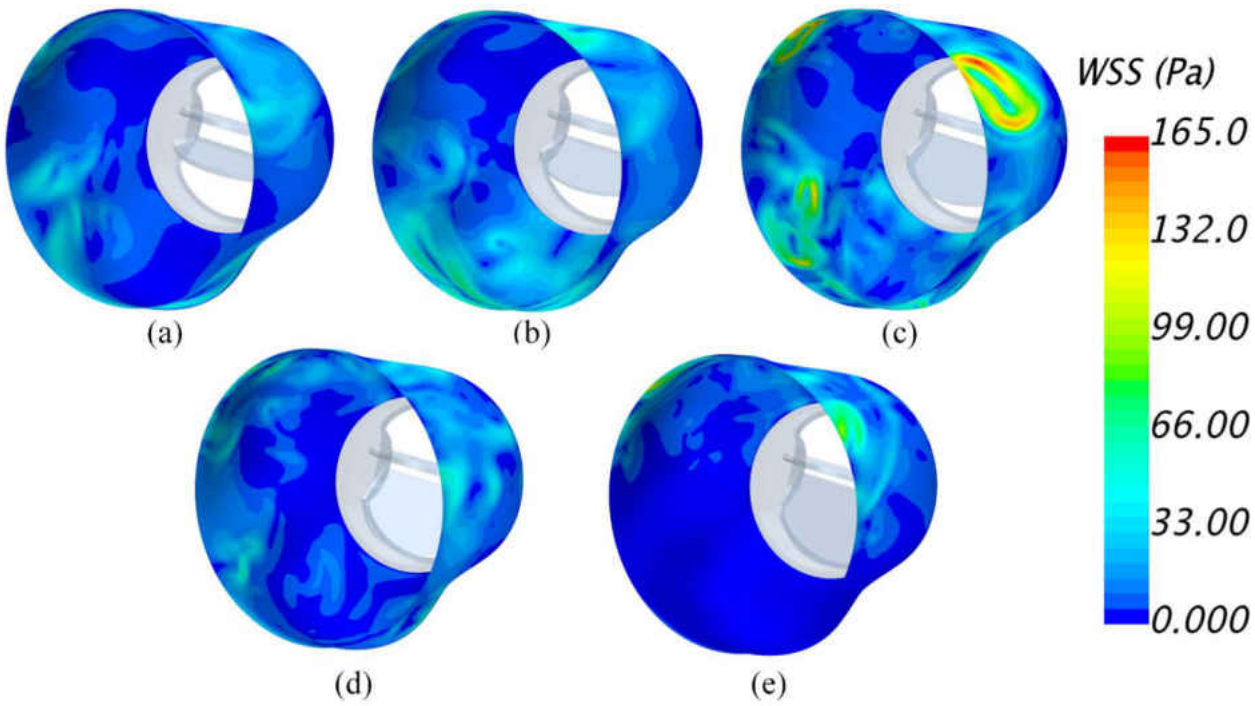

Figure 3-14 Wall shear stress distribution on aortic sinuses at the peak systolic velocity and different degrees of dysfunction: a) 0%; b) 25%; c) 50%; d) 75%; and e) 100%. Highest wall sheer stresses occurred around 50% dysfunction.

Figure 3-15 shows the wall shear stresses (WSS) on the valve frame at different levels of dysfunction for Newtonian (Figure 3-15a1 to a5) and non-Newtonian (Figure 3-15b1 to b5) flow conditions. Wall shear stresses increased with dysfunction, which was accompanied by increased velocity in the orifices. The case of at 0% dysfunction (Figure 3-15a1) was associated with lower WSS on the valve frame. At 50% and 75% dysfunctions, wall shear stresses increased on the valve wall downstream of the bottom orifice where flow with higher velocities passed through the orifice. At 100% dysfunction, lowest WSS was observed on the surface at the bottom valve surface. In addition, higher WSS developed around the hinges and frontal surface of the valve with dysfunctions, especially at 75% and 100% dysfunctions. Identification of areas of high WSS is important as it is associated with increased risk of thrombus formation [1]. As shown in Figure 3-15, WSS magnitudes for Newtonian flow were similar to those for non-Newtonian flow. The

maximum difference between the two cases was less than 2%. For example, the maximum WSS at 100% dysfunction was ~951 Pa and ~954 Pa for Newtonian and non-Newtonian flows, respectively. Therefore, we can conclude that the Newtonian flow assumption is appropriate for calculating WSS on valve frame.

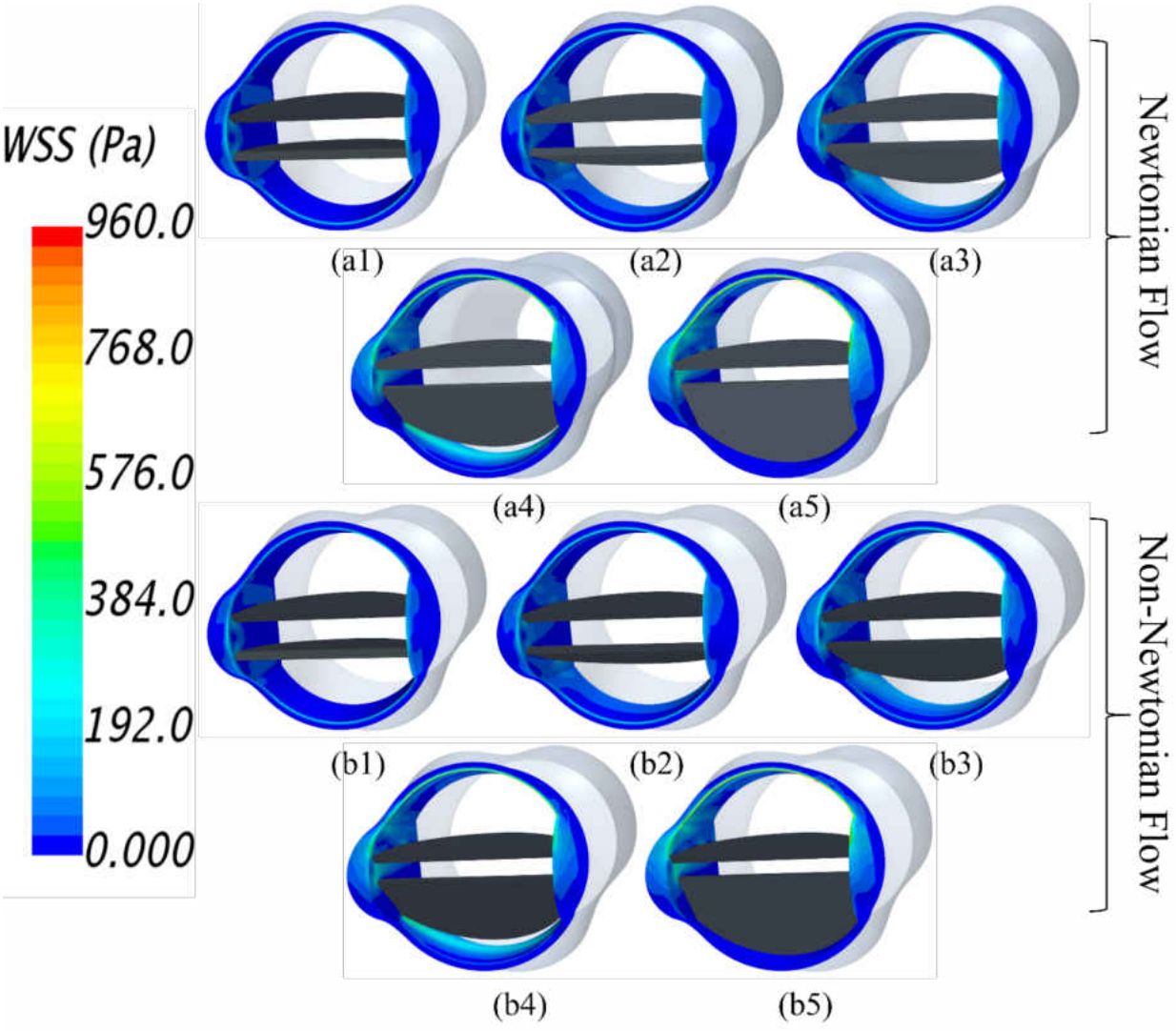

Figure 3-15 Wall shear stresses on valve frame; (a) Newtonian flow; (b) non-Newtonian flow. (1: 0%; 2: 25%; 3: 50%; 4:75% and 5: 100% dysfunction).

Table 3-2 illustrates the maximum values of the averaged wall shear stress applied on the heart valve frame, which occurred at the peak systole. The averaged and maximum wall shear stresses

on the valve frame at the peak systole increased with dysfunction. The information regarding the location of the highest WSSs in the flow domain is presented in this table. Also, the data indicate that the helicity increased with dysfunction and peaked around peak systolic velocity time.

Table 3-2 Averaged and maximum wall shear stresses (WSSs) on the valve frame, location of the highest WSSs in the flow domain and the maximum helicity in the aortic sinuses at peak systole.

Dysfunction (%)	Averaged WSS (Pa)	Max WSS (Pa)	Location of the Highest WSS	Maximum Helicity in Aortic Sinuses (m/s^2)
0	27.86	241.67	Leading edge of the leaflets	2088.01
25	38.71	326.77	Leading edge of the leaflets	5209.04
50	48.08	448.96	Leading edge of the leaflets, trailing edge of the dysfunctional leaflet and top leaflet hinges	5936.48
75	65.34	666.61	Inner surface of the Valve frame close to the trailing edge of the dysfunctional leaflet, bottom surface of the top leaflet and top leaflet hinges	8328.39
100	50.24	952.78	Upper half of the valve frame, top leaflet top and bottom surfaces and top leaflet hinges	9794.89

3.3.7 Helicity

Figure 3-16 shows helicity isosurfaces at different times and dysfunction levels. Since helicity is proportional to the flow velocity and the vorticity, it indicates the potential for development of helical flow. The data in this figure showed that helicity increased with dysfunction and peaked around peak systolic velocity time. This data also suggested that intense vortical structures start to appear in the valve and sinus regions during the acceleration phase (e.g., 60 ms) before spreading downstream at later times. For leaflet dysfunction of $\geq$ 75%, lower helicity (compared to dysfunctionality of < 75%) was observed in the dysfunctional leaflet side, which can be because the region downstream of that leaflet may contain lowered velocity and vorticity.

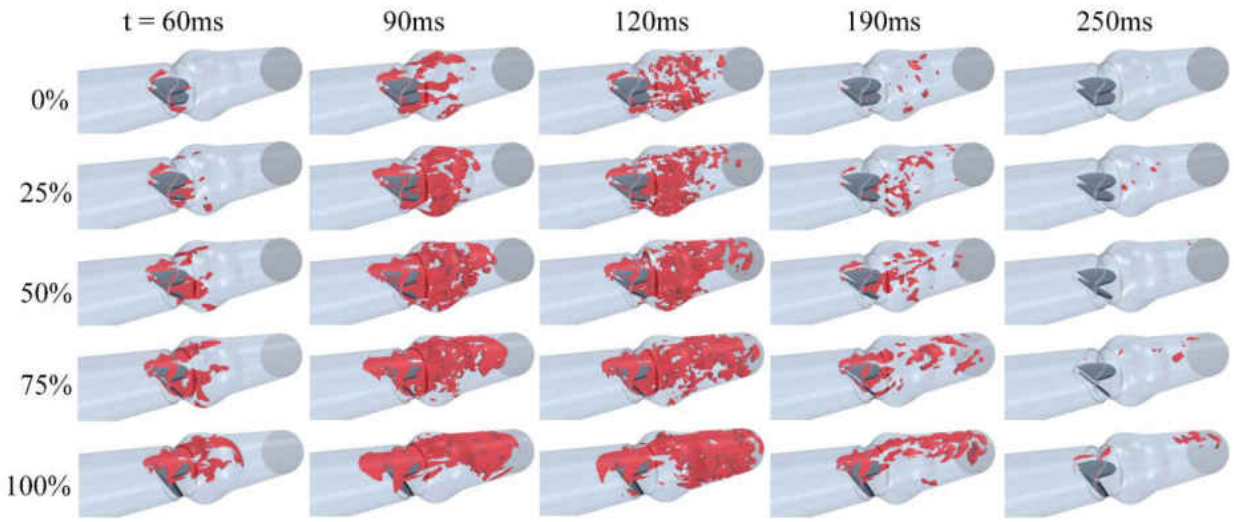

Figure 3-16 Helicity isosurfaces (isovalue = 414m/s2) at different times and dysfunctions. A general increase in helicity was observed with dysfunction.

3.3.8 Maximum Velocity and Pressure Drop

Figure 3-17a shows the maximum velocities at the entrance of the aortic sinuses, which were comparable to a previous computational study in which the results for only three dysfunctional cases (0%, 50%, and 100%) were reported [9]. The maximum velocity changed from 2.05 ms^{-1} to 4.49 ms^{-1} as dysfunction increased from 0% to 100%. Maximum transvalvular pressure gradient (TPG_{max}) can be computed from the maximal instantaneous velocity using the simplified Bernoulli equation ($TPG_{max} = 4v_{max}^{2}$) [9, 17]. More information about the calculation of the simplified Bernoulli Equation is available in APPENDIX I: SIMPLIFIED BERNOULLI EQUATION. Figure 3-17b shows the maximum pressure gradient compared to the previous study [9] for different levels of dysfunction. Here, the TPG_{max} increased from 16.48 to 80.64 mmHg. The higher velocities and pressure gradients in the current study can be because of the smaller valve diameter and the addition of valve ring (which likely caused more flow obstruction). Furthermore, the current study performed 3-D analysis rather than 2-D.

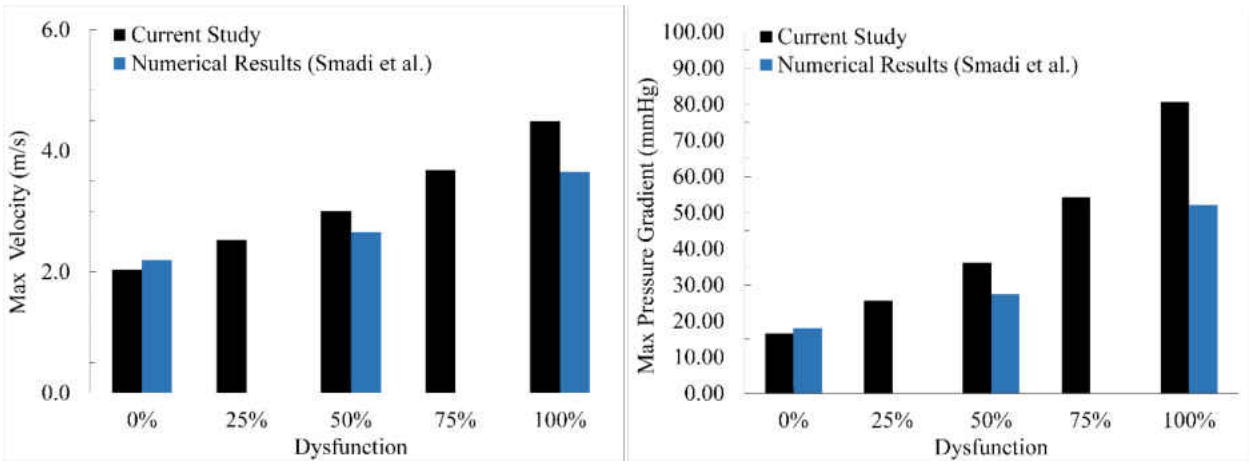

Figure 3-17 Comparison of the current study results with available data from a previous computational study (Smadi et al. 2010 [3]): (a) Maximum velocity at the entrance of the aortic sinuses, and (b) maximum pressure gradients across the valve computed from simplified Bernoulli equation. Both quantities continuously increased with dysfunction. While the trends were similar, differences may be due to the geometrical variations and the fact that the current study performed 3D compared to 2D simulation in [3].

3.3.9 Blood Complications

Three-dimensional principal stress analysis requires the computation of the full Reynolds stress tensor (T):

$$T = \begin{bmatrix} \sigma_{xx} & \tau_{xy} & \tau_{xz} \\ \tau_{yx} & \sigma_{yy} & \tau_{yz} \\ \tau_{zx} & \tau_{zy} & \sigma_{zz} \end{bmatrix} = \rho \begin{bmatrix} \overline{u'u'} & \overline{u'v'} & \overline{u'w'} \\ \overline{v'u'} & \overline{v'v'} & \overline{v'w'} \\ \overline{w'u'} & \overline{w'v'} & \overline{w'w'} \end{bmatrix} \tag{3-1}$$

where, u', v', and w' are the velocity fluctuation components and, σ and τ represent normal and shear stresses, respectively. Popov [21] provides a detailed discussion of the calculation of three-dimensional maximum or principal stresses which involves the solution of the roots of the following third order equation:

$$\sigma^3 - I_1\sigma^2 + I_2\sigma - I_3 = 0 \tag{3-2}$$

where,

$$I_1 = \sigma_{xx} + \sigma_{yy} + \sigma_{zz} \tag{3-3}$$

$$I_2 = \sigma_{xx}\sigma_{yy} + \sigma_{yy}\sigma_{zz} + \sigma_{xx}\sigma_{zz} - {\tau_{xy}}^2 - {\tau_{yz}}^2 - {\tau_{xz}}^2 \tag{3-4}$$

$$I_3 = \sigma_{xx}\sigma_{yy}\sigma_{zz} + 2\tau_{xy}\tau_{yz}\tau_{xz} - \sigma_{xx}{\tau_{yz}}^2 - \sigma_{yy}{\tau_{xz}}^2 - \sigma_{zz}{\tau_{xy}}^2 \quad (3\text{-}5)$$

The three roots $\sigma_1 < \sigma_2 < \sigma_3$ of the above equation are the three principal normal stresses. The coefficients $I_1, I_2,$ and $, I_3$ are functions of the measured Reynolds stress tensor and are the three stress invariants of the Reynolds stress tensor. In addition, the maximum or principal shear stresses (τ_{ij_P}) are linearly related to the normal stresses by the following equations:

$$\tau_{ij_P} = \frac{\sigma_i - \sigma_j}{2};\ \tau_{max} = \frac{\sigma_3 - \sigma_1}{2} \quad (3\text{-}6)$$

Several studies reported that the hemolysis (the breakage of a red blood cell's membrane), can occur for turbulent shear stresses in the range from 400 to 5000 N.m^{-2} with exposure time as small as 10 ms [22, 23]. In addition, these high turbulent shear stresses can lead to platelets activation, which increase the risk of platelet aggregation and blood clots formation [24, 25]. Blood clot may detach and the resulting free-floating clot can block arteries leading to serious consequences such as embolism and stroke [26].

While stresses acting on the fluid occur in different directions, principal stresses are the highest. Figure 3-18 displays turbulent shear (τ_{max}) principal stresses for different levels of dysfunction at the peak systole. Since an increased risk of blood damage may occur for stresses exceeding 400 N.m^{-2}, only stresses in this range are shown. These results suggested that as the leaflet dysfunctionality increased, the principal turbulent shear stresses increased. More specifically for 0 %, 25%, 50%, 75%, and 100% dysfunction levels, the maximum principal shear stresses at peak systole were 420, 510, 760, 1155, and 1695 N.m^{-2}. In addition, the regions of elevated stresses grew with dysfunction and were concentrated around and downstream of the functional (top) leaflet where high jet velocity and stronger helical structures existed (Figure 3-12, Figure 3-13, and Figure 3-16). These regions are of the particular interest since elevated turbulent stress levels are known to be associated with blood damage and thrombus formation.

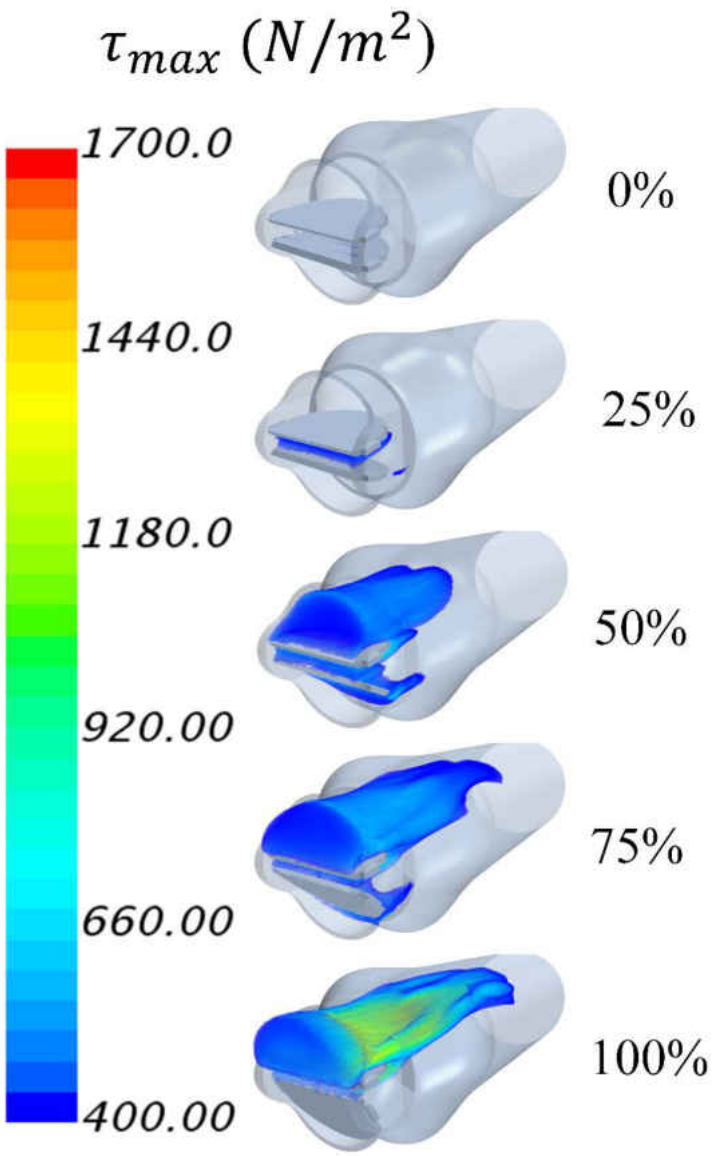

Figure 3-18 Principal shear stresses for different levels of dysfunction at the peak systole. Elevated levels of principal stresses were observed with dysfunction, which increase blood damage risks. Published cutoff stress value for damage is above 400 N/m2 [41].

The highest principal turbulent stresses, however, occurred slightly after (100-120 ms) peak systole during the deceleration phase. Table 3-3 shows the highest principal turbulent stress values and their occurrence time. It can be seen that these values were somewhat higher (~ 4-14%) than those at peak systole.

Table 3-3 Maximum Principal Shear Stresses

Dysfunction	Max. Principal Shear Stress ($N.m^{-2}$)	Time (s)
0%	440	0.102
25%	534	0.103
50%	832	0.112
75%	1276	0.112
100%	1972	0.119

3.3.10 Pressure Distribution

Figure 3-19 shows the pressure distribution in the vicinity of the leaflets. The maximum pressure at the blocked leaflet increased with dysfunction. For dysfunctions higher than 50%, a region of high pressure developed at the bottom surface of the functional leaflet upstream the hinge, which would generate higher moments in the direction of leaflet opening.

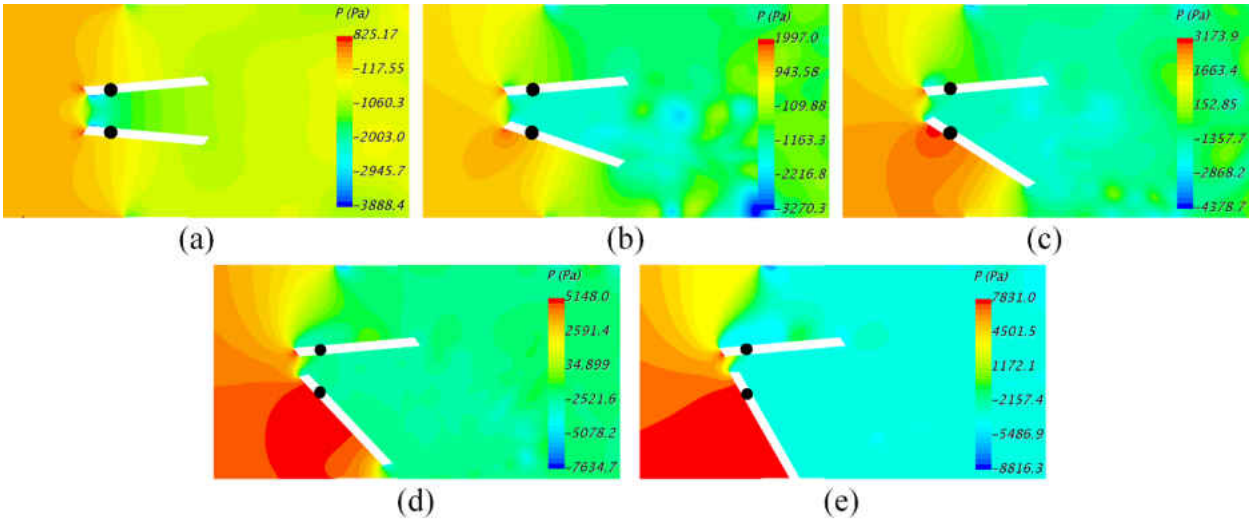

Figure 3-19 a) 0%; b) 25%; c) 50%; d) 75%; and e) 100%. For dysfunction ≥ 75%, a region of high pressure developed at the bottom surface of the functional leaflet upstream of the hinge, which would generate moments that tend to keep that leaflet open.

3.3.11 Applied Forces and Moments on Leaflets

The net pressure and shear forces on the top and bottom leaflets for the full cardiac cycle are displayed in Figure 3-20. Results showed that increased dysfunctionality of one leaflet led to higher net forces on the functional and dysfunctional leaflets up to 200%, and 600%, respectively. Note that although the net pressure forces (F_p) on the top leaflet were negative (upward) for 75% and 100% dysfunctions, forces were acting upstream of the hinges (Figure 3-19d-e), which would result in positive moments (Figure 3-21a). Figure 3-20b shows the F_p on the bottom leaflet, which was positive for all cases. Net shear forces (F_τ) on the top and bottom leaflets (Figure 3-20c and Figure 3-20d, respectively) were positive during the period under consideration for all levels of dysfunction except for the dysfunctional leaflet with 100% dysfunction. The change in the sign may be attributed to the large reveres flow regions (Figure 3-12a, and Figure 3-19) that formed downstream of the leaflet. The moments acting on the leaflets (Figure 3-21) also increased with dysfunction (up to 550%, and 4,000% for healthy and dysfunctional leaflets, respectively) and tended to keep the leaflets open during the opening period (60 ms to 250 ms). It is important to document elevated forces and moments as they would lead to higher reaction forces at the hinges (where thrombus tends to form), which may create more adverse conditions.

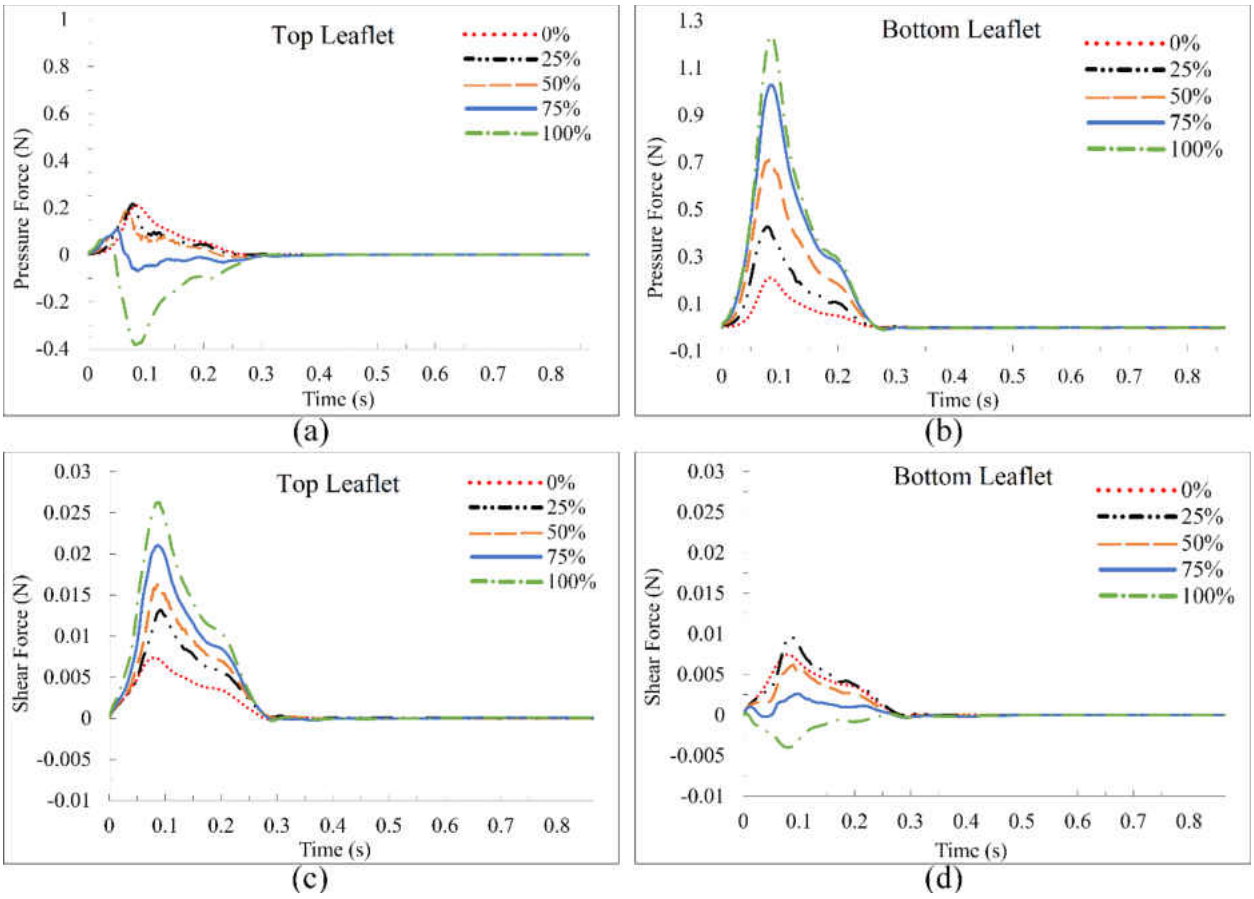

Figure 3-20 Net pressure and shear forces on leaflets: a) F_p on top leaflet; b) F_p on bottom leaflet; c) F_τ on top leaflet; and d) F_τ on bottom leaflet. The sign of some forces started to reverse at high levels of dysfunction.

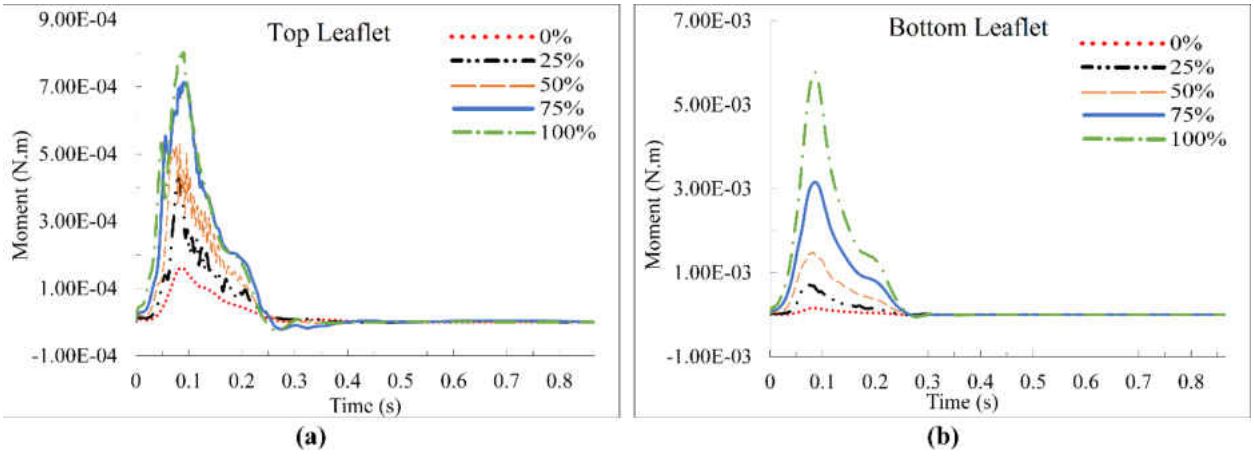

Figure 3-21 Net moments on: a) Top leaflet, and b) Bottom leaflet. The moments tended to be in the directions of leaflet opening. All moments increased with dysfunction. In most cases of dysfunction, the moments on the dysfunctional leaflet were higher (note the different scale for the dysfunctional leaflet).

3.3.12 Conclusion

In this study, adverse hemodynamics conditions at the peak systole due to incomplete leaflet opening of a bileaflet mechanical heart valve were investigated. A realistic 3-D geometry of the aortic sinuses and a complete model of a bileaflet mechanical heart valve including the valve ring were constructed. Results suggested that maximum blood velocities increased as the effective orifice area was reduced due to the increase of leaflet dysfunction. The higher levels of dysfunction were also accompanied with flow separation at the leaflet surfaces and growing eddies especially downstream of the valve in the aortic sinuses. Dysfunctionality increased the transvalvular pressure gradient by up to 300%, which would increase the effort to produce the same cardiac output. Principal turbulent stresses up to 1695 N.m-2 exceeded the threshold values for elevated risk of hemolysis and platelet activation, which can lead to potential developing thrombosis, especially around the normal leaflet. The region with high (i.e., above threshold = 400 N.m-2) principal stresses initially increased slowly (i.e., between 0 and 25% dysfunction). The region increased significantly at higher dysfunction suggesting a possible need for closer monitoring of the patients with > 50% of leaflet dysfunction. Dysfunctionality of one leaflet led to higher net forces on the healthy and dysfunctional leaflets (by up to 200%, and 600%, respectively). The resulting moments acting on the leaflets also increased with dysfunctionality (up to 550%, and 4,000% for healthy and dysfunctional leaflets, respectively) and tended to keep the leaflets open during the opening period (60 ms to 250 ms). These higher forces and moments would tend to increase the reaction forces and stresses in the hinge region where vulnerability to thrombus and pannus formations tend to be high and lead more leaflet motion restriction.

3.4 Different Geometry of Aortic Sinuses (Patient-Specific Condition II)

Bileaflet mechanical heart valves have one of the most successful valve designs for more than 30 years. These valves are often used for aortic valve replacement, where the geometry of the aortic root sinuses may vary due to valvular disease and affect valve performance. Common geometrical sinus changes may be due to valve stenosis and insufficiency. In the current study, the effect of these geometrical changes on the mean flow and velocity fluctuations downstream of the valve and aortic sinuses were investigated. The study focused on the fully-open leaflet position where blood velocities are close to their maximum. Many heart disorders initiate within the left ventricle, as this chamber is subjected to the highest mechanical loads [159]. The blood flow through the left ventricle is regulated by the mitral and the aortic valves, which influence the inflow and the outflow conditions, respectively [160]. The aortic valve, in particular, is one of the most commonly affected heart valves in a diseased heart [161]. Aortic valve pathologies such as stenosis and insufficiency cause a variation in the geometry of aortic sinuses and affect the performance of the aortic valve [162]. This incidence is responsible for 44% of morbidity [163]. Analysis of flow dynamics around heart valves [46,91,97,98], and cardiac sounds [48,105,164–166] may help lowering mortality rates. These pathological changes in extreme cases are often due to aortic incompetence caused by a dilated, aortic dissection, and severe aortic valve stenosis [167–169]. In addition, deformation of the aortic root after valve replacement or structural dysfunction of the recently replaced bioprosthetic heart valve due to pure stenosis due to cusps stiffening is common [170]. It would be desirable to match a prosthetic heart valve type with a specific type of aortic geometry in order to obtain a disturbance-free velocity field with low pressure drop.

Successful analysis of the flow through prosthetic heart valves such as bileaflet mechanical heart valves (BMHVs) depends on sufficient understanding of the conditions under which natural

valves function. Previous studies showed that the geometry of the aortic root sinuses can contribute to the vortex generation and flow recirculation [171]. As a result, these shear stresses can cause damage to the blood cells and facilitate thrombus formation. Barannyk et al. [91], analyzed the impact of the aortic root geometries on the pulsatile blood flow through a prosthetic valve. It was found that the different geometries did in fact create different Reynold Shear stresses and recommended that the implantation of a prosthetic valve should be done in conjunction with the root geometry in order to limit the possible levels of stresses.

The objective of this study is to investigate the dimensional changes of the aortic root due to aortic valve disease, such as valve stenosis and valve insufficiency, and to determine the influence of those changes on the appearance of abnormal flow patterns in the flow through aortic bileaflet mechanical heart valve. The accurate representation of a complex aortic root anatomy was modelled as it is essential in order to reproduce the internal physiological flow field correctly. The mean flow and velocity fluctuations downstream of the valve and aortic sinuses with the focus on the fully-open leaflet position were investigated. This information can be used to improve the design of mechanical heart valves in future studies and gain better understanding of the hemodynamics of blood flow through the prosthetic valves.

In this study, a bileaflet mechanical heart valve was modelled similar to previous studies [9,10,172], which in the fully open position divides the flow into three orifices: two of them (top and bottom orifices) are roughly semicircular and the third (middle orifice) is approximately rectangular (Figure 3-22). An enhancement implemented in the current study (compared to some previous two-dimensional CFD studies [3,90] was to include the valve ring into the model. In addition, a realistic geometry of the aortic sinuses was created since this is important for appropriate flow field analysis [46,173].

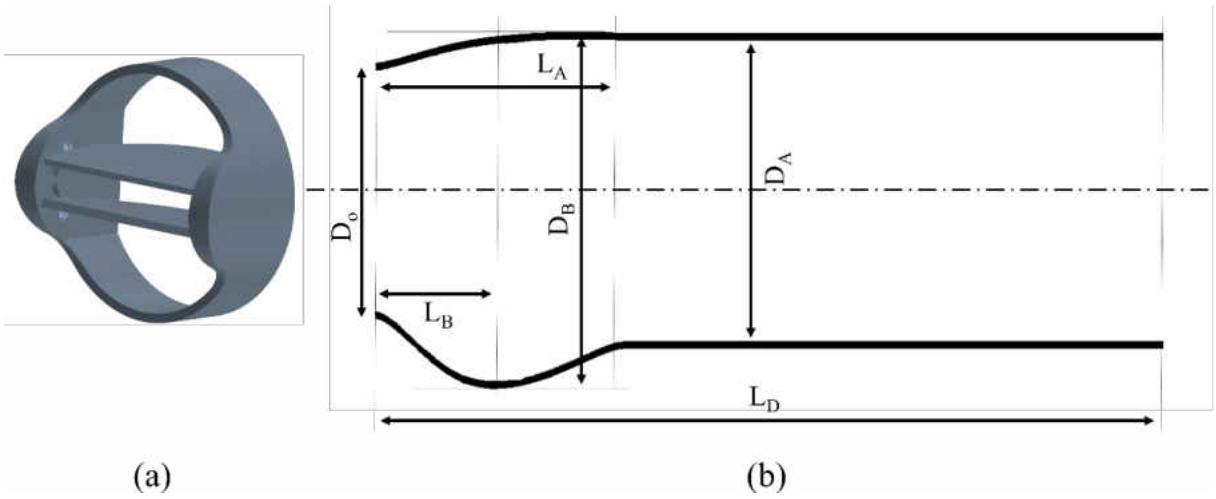

Figure 3-22 (a) Bileaflet mechanical heart valve; (b) Cross-sectional view of aortic root sinuses.

Figure 3-22b shows the cross-sectional view of the asymmetric aortic sinuses geometry with inlet aortic root diameter of d = 0.023 m, which was extracted from angiograms [174]. In this paper, the aortic root was modeled based on following parameters: D_O is the diameter of aortic annulus, D_A is aortic diameter, D_B is the maximum projected sinus diameter, L_A is the length of the sinuses, and L_B is the distance between D_O and D_B. These parameters can be computed based on the aortic annulus diameter (D_O), which is the same as the size of the implanted mechanical heart valve. L_D = 100 mm is the length of the region downstream of the heart valve. The corresponding parameters to the aortic valve stenosis and aortic valve insufficiency are included in the Table 3-4. They are referred as dilated aortic root and constricted aortic root, respectively [174].

Table 3-4 Parameters for the geometrical characterization of the aortic root

Parameters (mm) →	D_O	D_A	D_B	L_A	L_B
Normal	22.3	27.7	34.6	22.3	7.6
Severe Stenosis	22.3	33.5	38.4	23.2	12.1
Severe Insufficiency	22.3	23.5	30.6	18.3	12.5

3.4.1 Velocity Distribution

Figure 3-23 shows the velocity distribution through the BMHV for different aortic root geometries at the peak systole. Results showed a maximum velocity of ~2.5 $m.s^{-1}$ for all geometries which appear at the leading edge of the leaflets and through the three orifices. However, severe stenosis and insufficiency changed the flow pattern downstream of the heart valve and in the aortic sinuses. For normal sinuses (Figure 3-23a), the flow is relatively uniform downstream of the aortic roots. As the central orifice jet developed during the systole phase, the peak values of velocity fluctuations (or high turbulent intensities) remained concentrated in the wake of the leaflets in the region where the jet became highly unstable and the shear layers breakdown to vortical structures. For the severe insufficiency roots (Figure 3-23b), large vortical structures were created and trapped in the sinus region. The high-velocity jets through the top and bottom orifices tend to keep these vortices, and consequently the blood components, inside the sinuses with low velocity and pressure gradients. These may cause higher risk of blood clotting and thrombus formation. In addition, the wake behind the leaflets and high-velocity flow extended far downstream of the leaflets. This can lead to higher wall shear stresses on the aortic sinuses. The velocity distribution downstream of the valve for the severe stenosed aortic sinuses were similar to the normal sinuses (Figure 3-23c); however, small-size vortices along with secondary flow region were created. These phenomena can increase the potential for blood damage and platelet activation.

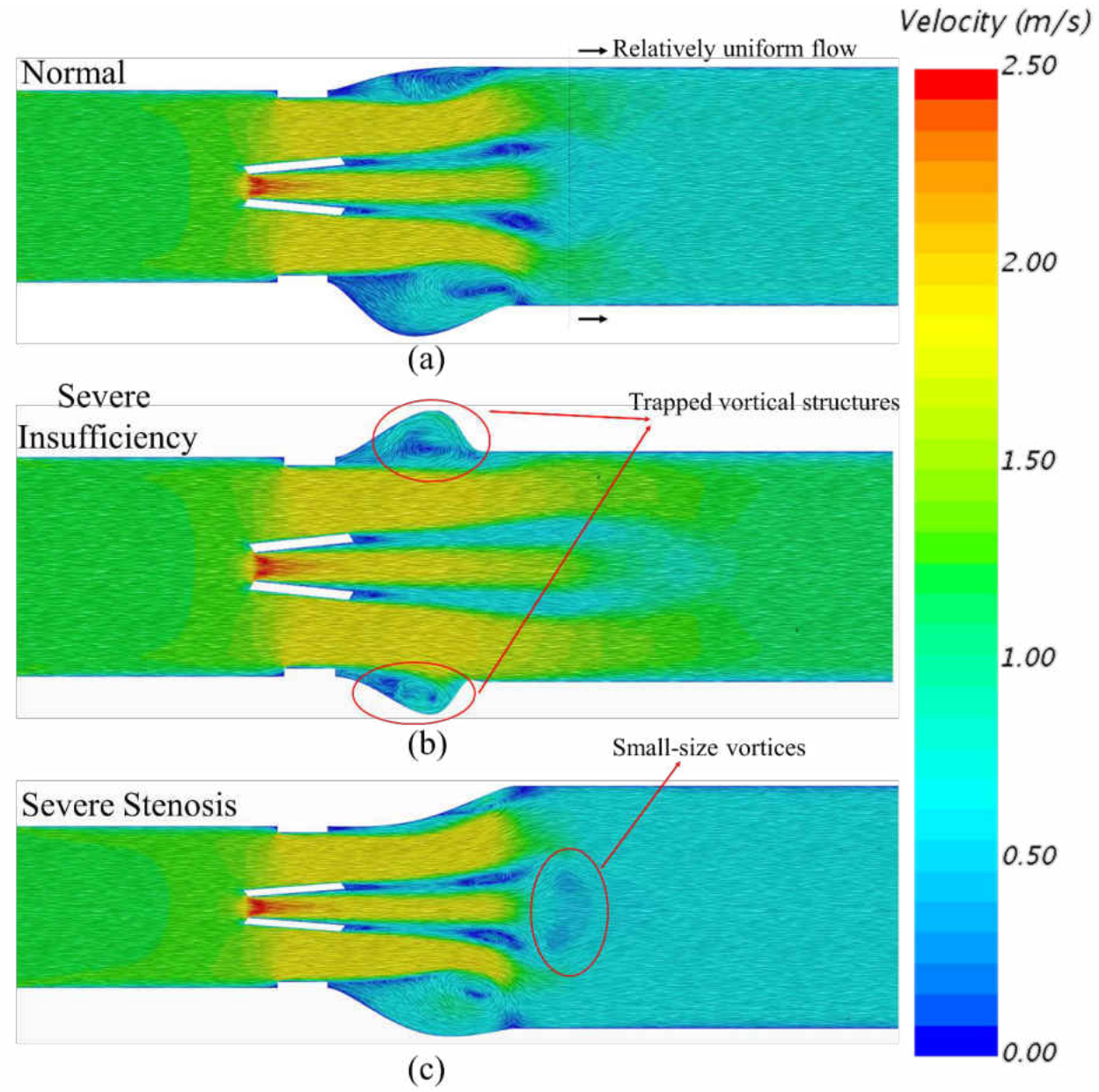

Figure 3-23 Velocity distribution through a bileaflet mechanical heart valve for different geometries of aortic root sinuses: (a) normal sinuses; (b) severe insufficiency; (c) severe stenosis.

3.4.2 Wall Shear Stresses

Figure 3-24 shows the instantaneous distributions of wall shear stress (WSS) on the different geometries of aortic sinuses at the peak systolic phase. The vortices which existed in the sinuses (Figure 3-23) caused wall shear stresses (WSS) up to 60 Pa for the normal aortic roots (Figure

3-24a). The regions with low levels of WSS demonstrate the desirable hemodynamic conditions of this BMHV. For the aortic insufficiency, the trapped vortices (a region of recirculation with high velocity fluctuations) led to high values of WSS about 110 Pa. Conversely, for severe stenosis, wall shear stresses on the sinus were lower and similar to normal sinuses possibly due to lower eddies in the sinuses. High wall shear stresses increase the potential risk of blood clotting and vascular diseases like aortic stenosis.

3.4.3 Principal Shear Stresses

Several studies reported that the hemolysis (the breakage of a red blood cell membrane), can occur for turbulent shear stresses in the range from 400 to 5000 $N.m^{-2}$ with exposure time as small as 10 ms [41,175]. In addition, these high turbulent shear stresses can lead to platelets activation, which increase the risk of platelet aggregation and blood clots formation [16]. Clots may detach and the resulting free-floating clot can block arteries leading to serious consequences such as embolism and stroke [47,176]. While stresses acting on the fluid occur in different directions, principal stresses are the highest. Figure 3-25 displays maximum turbulent shear (TSS) principal stresses for different geometries of aortic root sinuses at the peak systole and how a deformation in the aortic root geometry led to the elevated levels of the TSS. The TSS distribution through the BMHV for the normal and severe stenosis (Figure 3-25a, and Figure 3-25c) showed similar pattern with the maximum values of ~790 and 805 $N.m^{-2}$. For the severe stenosis, the TSS decreased far downstream of the valve which can indicate the suitability of this BMHV for this condition. On the other hand, TSS was significantly higher around and downstream of the heart valve for the severe insufficiency (Figure 3-25b). The maximum TSS value of 820 $N.m^{-2}$ was observed for this aortic root geometry. These results shows that the implantation of this BMHV for the severe insufficiency of the aortic root sinuses would need extra care.

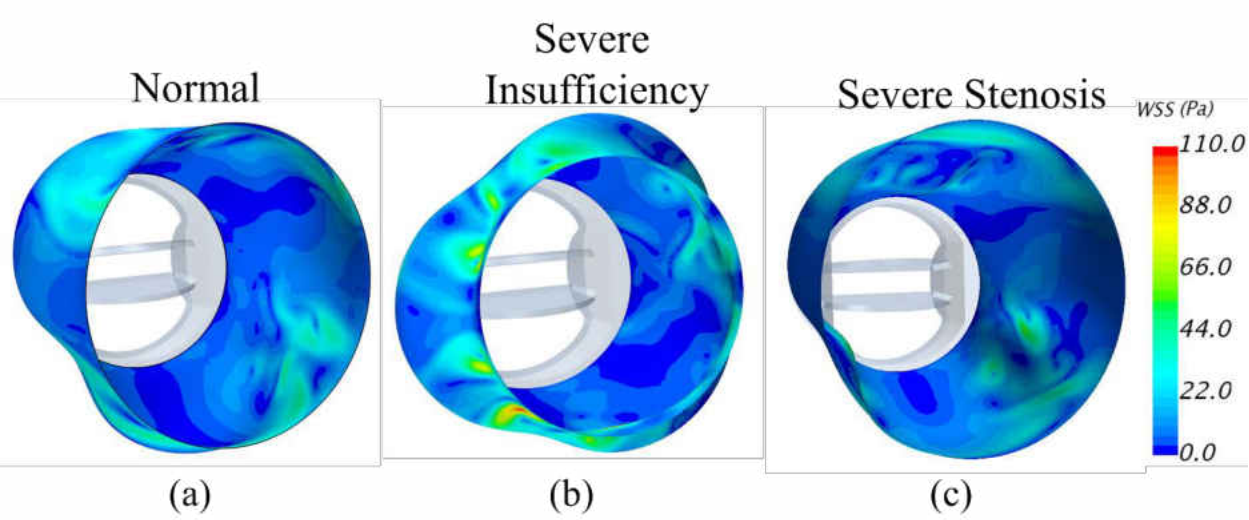

Figure 3-24 Wall shear stress distribution on different geometries of aortic root sinuses: (a) normal sinuses; (b) severe insufficiency; (c) severe stenosis.

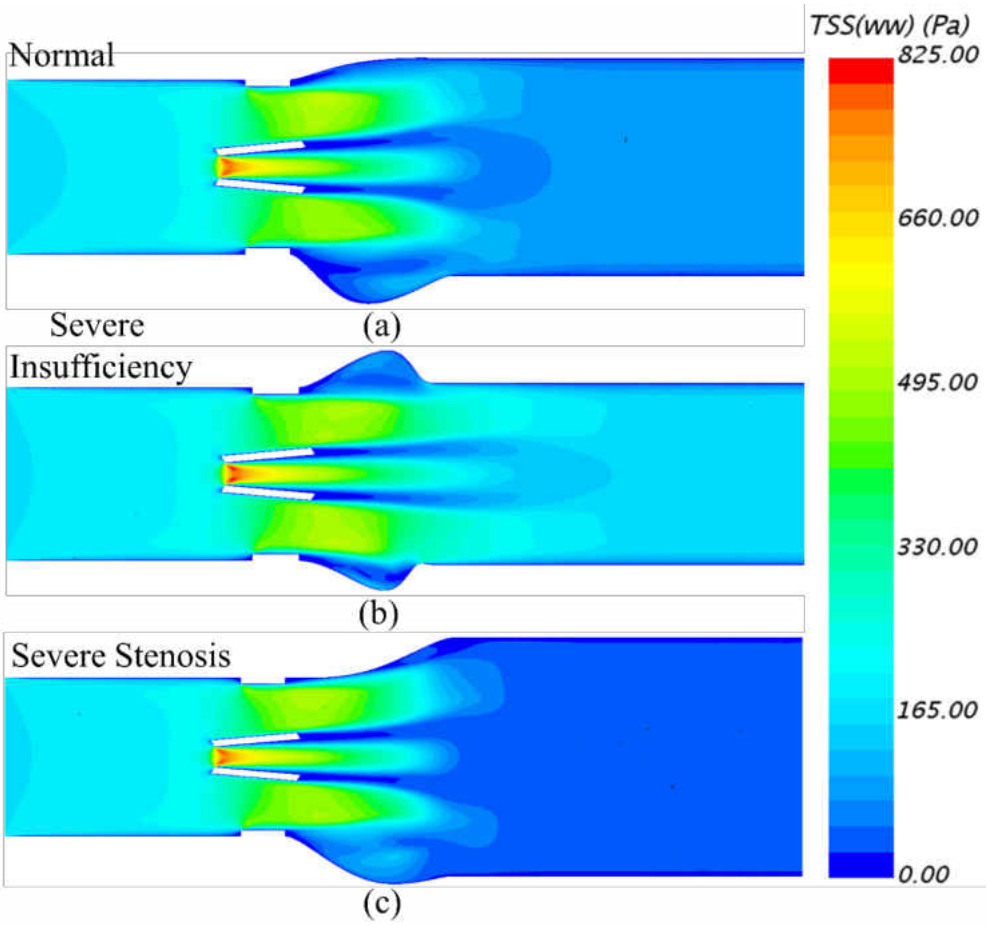

Figure 3-25 Turbulent shear stresses (TSS) through a bileaflet mechanical heart valve for different geometries of aortic root sinuses: (a) normal sinuses; (b) severe insufficiency; (c) severe stenosis.

3.4.4 Conclusion

In this study, the influence of pathological changes of the dimensions of the aortic root sinuses on the appearance of abnormal flow patterns in the flow through aortic bileaflet mechanical heart valve was investigated. These pathological conditions investigated were valve stenosis and valve insufficiency. The results showed that the flow through the BMHV with normal and aortic root severe stenosis were similar in terms of the vortical structures and corresponding stresses on and downstream of the aortic sinuses. These results demonstrate the desirable hemodynamic conditions of this BMHV for these conditions (normal and severe stenosed aortic roots). On the other hand, the results for the valve insufficiency indicated that flow through the BMHV lead to trapped vortical structures in the sinus region while the turbulent intensity remains high downstream of the valve. Therefore, implanting a heart valve without considering the consequences such as adverse hemodynamic conditions in the aortic root geometry caused by valve diseases might result in sublethal or lethal damage to blood components as well as increased risk of platelet activation.

3.5 Limitations

In this study, the artery wall was considered as rigid walls; therefore, the fluid-structure interactions of the walls were neglected. The contraction and expansion of the walls may lead to reduction in the reaction forces and wall shear stresses. In addition, lumped parameter (also known as 0-D model) can be useful addition to these studies as it can modeled the rest of the bodies on the boundaries.

CHAPTER 4: SOUND ANALYSIS

Most fluid flows are characterized by irregularly fluctuating flow quantities that often occur at small scales and high frequencies. Hence, resolving these fluctuations in time and space requires excessive computational cost. Optimum modeling of these structures [69,177,178] is of interest for the acoustic investigations including biomedical applications, which are active areas of research [49,105,164,165,179–181].

The ANSYS Mechanical solver performs the harmonic response analysis in a frequency sweep over the whole spectrum to compute the broad-band sound in the frequency domain. To analyze the sound through the vessel wall and tissue layer with a vibrating wall, caused by the turbulent blood flow, it is required to couple ANSYS Fluent results and Mechanical simulation. The objective of harmonic analyses is to calculate response of system as a function of frequency based on volumetric flow rate or pressure excitation. The current proposed coupled acoustic analysis takes the fluid-structure interaction into account.

Here, the workflow of the combined usage of the CFD software ANSYS Fluent [92] and the vibration and acoustics simulation tools of ANSYS Mechanical [92] is demonstrated:

- Prepare a 3D simulation of the blood flow through the bileaflet mechanical heart valve.
- Install and add the ACT Acoustics extension.
- Set up the export of the wall pressure signals on the internal side of blood vessel wall.
- Run the transient flow simulation.
- Compute the Fourier transform of the wall pressure signals, visualize its results in different frequency bands, and export fields of the complex Fourier amplitudes in the CGNS format.

Fluent allows to export in CFD general notation system (CGNS) files pressure values of a transient turbulent run after its transformation in the frequency domain. The CGNS files can be used in Mechanical to map the pressure of the structural component at each frequency in harmonic response analyses.

The second part of the sound analysis continues with the subsequent ANSYS Mechanical simulation steps:

- Set up a harmonic response analysis in ANSYS Workbench.
- Import the structural bodies (blood vessel and tissue layer).
- Define the acoustics properties of the vessel wall and tissue layer.
- Insert a “CFD Pressure mapping” object in the harmonic analysis (from the “Tools” menu of the “Acoustics” toolbar).
- Select the faces on which the pressure will be mapped (internal side of blood vessel wall).
- Map the real and imaginary components of the pressure from the CGNS files.
- Perform the frequency vibroacoustic analysis of the vessel wall and tissue layer. The solver performs the resolution for all frequencies between the “Range Minimum” and the “Range Maximum” contained in those files. Here, frequency range of 1 to 500 Hz were selected.
- Post-process the vessel wall and tissue layer deformations and the sound pressure levels at any location.

The “Full” harmonic resolution method must be chosen here because this is currently the only solution method supported to import and map the CFD pressure from the CGNS files. In post-processing it is possible to display the mapped pressure at a given frequency.

In addition, the mesh should be fine enough to capture the mode shapes of the structure. For linear elements, at least 12 elements per wavelength are needed, while 6 elements per wavelength are needed for quadratic elements [92]. The wavelength can be calculated by,

$$\lambda = \frac{c}{f} \tag{4-1}$$

4.1 Validation of Hydro-Vibroacoustics Approach

4.1.1 Geometry

A two-dimensional constricted channel is considered (Figure 4-1) similar to a previous study [83]. This geometry serves as a model of a stenosed artery in patients with vascular diseases.

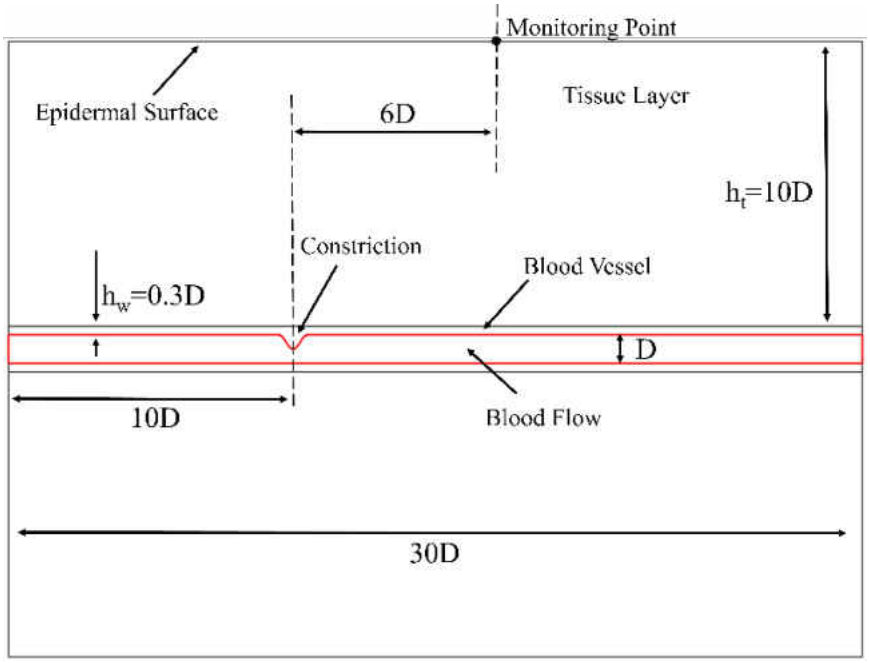

Figure 4-1 Schematic of the constricted channel model and acoustic domain; D arterial diameter, h_w arterial wall thickness; h_t tissue layer thickness.

The channel is constricted from top wall, and the profile of the constriction is given by

$$\boldsymbol{y = y_{max} - \frac{b}{2}\left[1 + cos\left(2\pi\frac{x-x_0}{D}\right)\right]}; \tag{4-2}$$

$$-D \leq (x - x_0) \leq D$$

where, x_0 is the center of the stenosis, $D \cong 11.34$ mm is the height of the channel, and $b = 0.5D$ is the size of the constriction. Similar constricted artery models were also used in earlier studies [182,183].

4.1.2 Hemodynamics

The CFD analysis was performed for a pulsatile flow. The flow was driven by a pulsatile pressure drop between the inlet and outlet with a sinusoidal variation in time as defined in Equation 4-3 and shown in Figure 4-2 (non-dimensional form):

$$\frac{\Delta P}{\rho U^2} = [A + B\ sin(2\pi f t)] \tag{4-3}$$

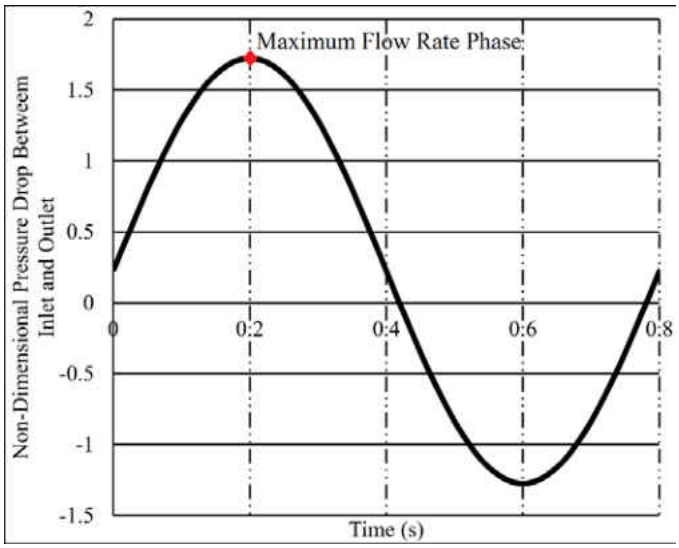

Figure 4-2 Non-dimensional pulsatile pressure drop between inlet and outlet.

where, A is set to 0.225 and B to 1.5. The non-dimensional frequency of pulsation (Strouhal number), describing oscillating flow mechanisms, is $St = fD/U_{max}$= 0.024 and the Reynolds number is set to $Re = \rho U_{max} D/\mu = 2000$, where $f = 1.25$ Hz is the frequency of pulsatile flow for the heart rate of 75 bpm, $U_{max} \cong 0.59$ m.s^{-1} is the maximum centerline velocity at the inlet. In addition, density ρ =1050 kg.m^{-3}, and dynamic viscosity $\mu = 0.0035$ Pa.s. The chosen flow parameters yield a Womersley number of $\alpha = (\pi \cdot Re \cdot \frac{St}{2})^{1/2} = 8.6$, which is in the appropriate

range for large arteries [184]. In this study, flow was considered to be laminar. The unsteady simulation was performed with a time step of 0.1 ms and 10 iterations per time step. Numerical solution typically converged to residuals < 10^{-4}. Moreover, high quality triangular mesh was generated in the flow domain, especially in the stenosed region. Therefore, y^+ was maintained less than 1 close to all walls. In the current model, the blood flow is assumed to be Newtonian (which is a good assumption for the larger and medium sized arteries [32]).

In addition, a mesh-independent study was conducted to find the optimized mesh configuration. Prism layer mesh was also employed near the boundaries since accurate prediction of pressure drop in flows with separation depends on resolving the velocity gradients normal to the wall [141,142]. Dirichlet pressure boundary conditions are applied at the exit ($p_{exit} = 0$), and a no-slip boundary condition is used for the top and bottom walls. The flow computations are carried out for about four pulsation cycles after it reaches a stationary state.

4.1.3 Acoustics

This coupled acoustic analysis takes into account the fluid-structure interaction (pressure waves generated by vessel wall deformation due to fluid pressure). The interactions of the fluid and the internal side of the vessel wall at the mesh interface causes the acoustic pressure to exert a force applied to the structure and the structural motions produce an effective "fluid load". The transient pressure (force) fluctuations on the vessel wall excite the solid domain, causing vibrations which in turn detected as sound on the epidermal surface. Any sustained cyclic load will produce a sustained cyclic response in a structure which is often called a harmonic response. Harmonic response analysis (HRA) in ANSYS finite element analysis (FEA) software package [92] was used to simulate these vibrations. HRA calculates the steady-state (harmonic) response of a linear structure subjected to a harmonically varying load. HRA can solve for the response of a structure to

harmonically varying loads over a frequency range. The equation of motion of a structure under harmonic loading can be derived as,

$$\boldsymbol{M\ddot{x} + C\dot{x} + kx = F(t)} \tag{4-4}$$

$$\boldsymbol{F(t) = F_{max} e^{i(\omega t+\varphi)}} \tag{4-5}$$

$$\boldsymbol{x(t) = x_{max} e^{i(\omega t+\theta)}} \tag{4-6}$$

$$(-M\omega^2 + i\omega C + k)x_{max}e^{i(\omega t+\theta)} = F_{max}e^{i(\omega t+\varphi)} \tag{4-7}$$

In the above equations, Equation 4-4 represents the equation of motion of a structure in time domain, where M, C, and k denote structural mass, damping and stiffness matrices. If the applied force, $F(t)$, is harmonic, it can be represented as in Equation 4-5 where, F_{max}, ω, φ are the force amplitude, angular frequency and phase shift, respectively. Similarly, the displacement $x(t)$ is also harmonic under harmonic loading and presented in Equation 4-6, where x_{max}, θ are the magnitude and phase shift of displacement, respectively. By substituting Equations 4-5 and 4-6 in Equation 4-4, the derived Equation 4-7 is solved in HRA simulation. In the present work, the pressure fluctuations on the vessel wall are recorded from the CFD solution, which are later transformed in to frequency domain using Fast Fourier Transformation (FFT). The transformed pressure in the frequency domain are then mapped on to the vessel wall in HRA simulation.

Figure 4-3 shows the hydro-vibroacoustic simulation methodology in the current study:

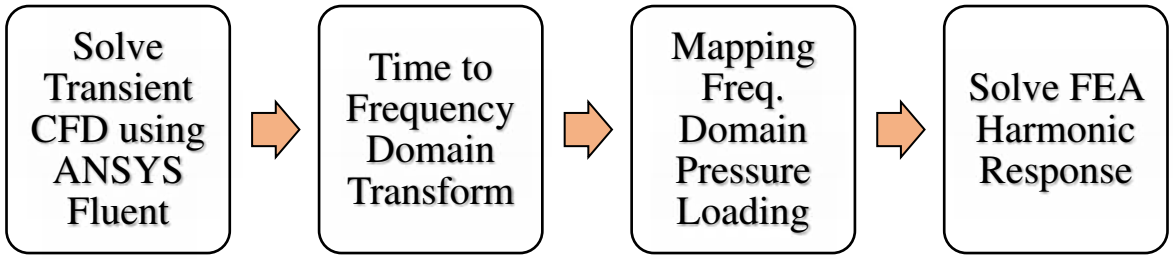

Figure 4-3 Hydro-vibroacoustic Simulation methodology of the current study using ANSYS Fluent and FEA Harmonic Response.

In the current study, the fluid–structure interaction of blood flow with the arterial wall was also considered; however, it was neglected in the previous study [83]. These interactions with the elastic blood vessel may introduce resonance peaks in the sound spectrum [185]. However, these resonance peaks generally vanish due to the damping associated with the surrounding tissue and may not have important components in the sounds detected at the skin surface [68,83,185]. The acoustic domain in the current study includes not only the lumen surface but also the arterial wall (blood vessel) and the surrounding tissue layers. The acoustic material properties were: the density of 1050 $kg.m^{-3}$, 1100 $kg.m^{-3}$, 1200 $kg.m^{-3}$, and speed of sound of 1500 $m.s^{-1}$, and 1580 $m.s^{-1}$, and 1720 $m.s^{-1}$ for the blood, vessel wall and surrounding tissue, respectively. The top boundary of the acoustic domain represents the epidermal surface at which a stethoscope can sense transmitted sound via the displacement, velocity, or acceleration of the epidermis. It is also assumed that the acoustic waves radiate through all other boundaries. The shear waves generated in the tissue were considered negligible compared to the acoustic waves and that the viscous dissipation of the acoustic wave was also neglected [77,83,85]. In a previous study [83], only the bulk modulus and speed of sound of the materials were specified. However, the same bulk modulus corresponds to many combinations of Young's modulus and poisson's ratio values. The latter parameters highly affect the stiffness of the vessel wall and tissue layers, which consequently alter the amplitude of the sound propagation. Hence, each bulk modulus can correspond to many solutions. In addition, any difference in the Reynolds number could highly affect the flow behavior and the amplitude of the pressure forces on the vessel wall.

4.1.4 Instantaneous Vorticity

The instantaneous vorticity contours at different times are shown in Figure 4-4. The results are in good agreement with the previous results [83,184]. For the 50 % stenosed artery, it is observed that

the vortex roll-up starts from the maximum flow rate phase (0/8T, where T is the period of pulsation). The detachment of separation bubble in the wake of the stenosis, and the boundary layer separation at the bottom surface are clearly visible. At 4/8T, the shear layers become unstable during deceleration and a coherent vortex series are formed as shown with an overall wavelength of about 1D.

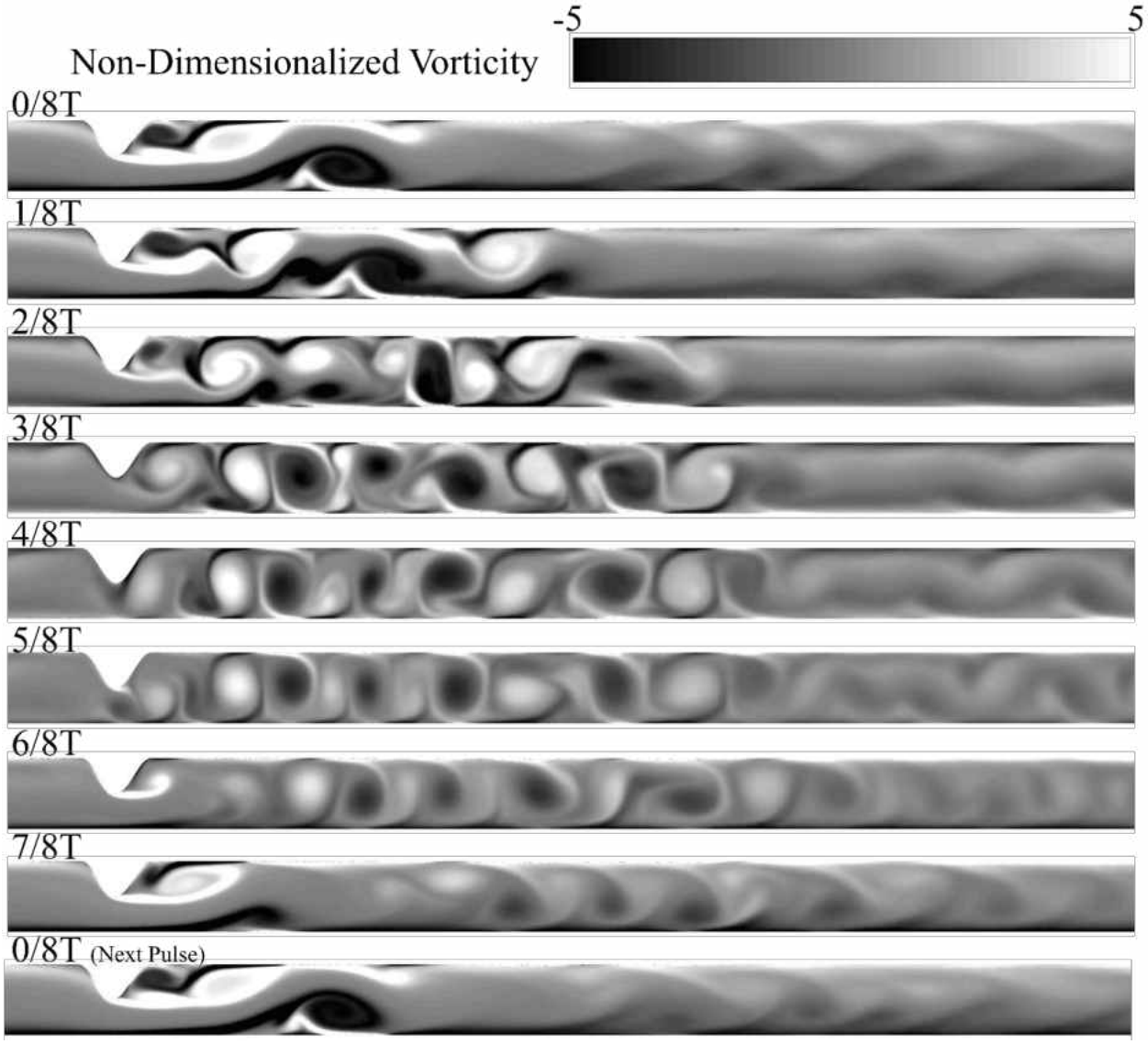

Figure 4-4 Time evolution of vorticity field; 0/8T maximum flow rate, 4/8T minimum flow rate phase. (The vorticity contours shown were normalized by time scale D/U_{max}).

4.1.5 Sound Analysis

The signal through the tissue layer was monitored at 6D downstream from the stenosis on epidermal surface (see Figure 4-1), where the maximum acoustic energy could be observed [83]. The calculated spectra of vertical velocity fluctuations on epidermal surface using HRA agreed with the spectra calculated from linearized perturbation compressible equation [83].

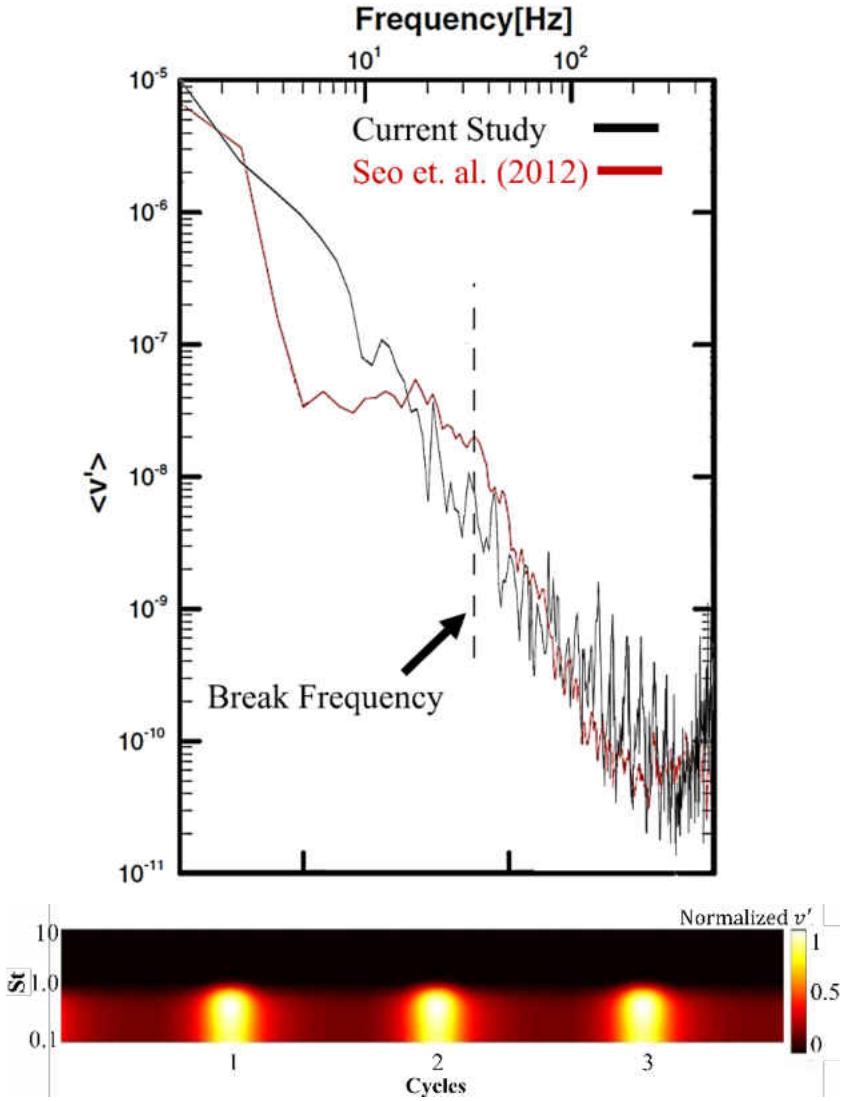

Figure 4-5 Frequency spectrum of vertical velocity fluctuations (v') on the epidermal surface monitored 6D downstream from the center of the stenosis. The frequency was (y-axis) was normalized (from 0.1 to 10).

The most energetic frequency was 1.25 Hz, corresponding to the heart pulse rate of 75 bpm. The next distinct frequencies were found to be approximately 20 and 40 Hz which are in good agreements with the previous study [83]. The vertical dashed lines indicate the break-frequency [79], where the slope of the spectrum changes significantly. The current model could accurately capture the break frequency of the spectrum. The break-frequency is a system's frequency response at which the energy flowing through the system begins to be reduced. This is due to the breakage of the large eddies (vortices) into small eddies in the flow domain. The difference in the amplitude of the solid velocity and velocity fluctuations could be caused by the material properties of the vessel wall and tissue layers. Time–frequency spectrogram of epidermal vertical velocity fluctuation, which is plotted in Figure 4-5b for the stenosed artery, shows the intensity and frequency content of the arterial bruit.

4.1.6 Advantages and Limitations

Here are some of the advantages of the current hydro-vibroacoustic method compared to the previous models [83]:

- Considering both shear and longitudinal wave propagations.
- Accurately capturing the break frequency of the velocity fluctuation measured on epidermal surface.
- Capability of providing accurate solution with a faster computational time.
- Considering the fluid–structure interaction between blood flow and the arterial wall.

In this study, lumped parameter (also known as 0-D model) could be useful addition to these studies as it can model the rest of the systems (e.g. blood vessels) connecting to the boundaries. Also, the accuracy of the current method for the unsteady and varying flow conditions (especially, for pulsatile flow) can more investigated in future works.

4.1.7 Conclusion

A new computational approach for simulating the blood flow-induced sound generation and propagation in a stenosed artery with one-sided constriction was investigated. The employed HRA method was capable of getting an accurate solution with a faster solution time. The analysis of the computed results indicates that the epidermal velocity fluctuations were correlated with transient pressure (force) fluctuations on the vessel wall more intense over the near post-stenotic region. This supports the view that the primary source of arterial bruits is the vortex inducted perturbations in the near post-stenotic region.

4.2 Future Work

Sound would be the bridge between engineers and clinicians, as clinicians mostly rely on the sound signature of the biological systems for medical monitoring and diagnosis. Computational sound analysis of a bileaflet mechanical heart valve (BMHV) can provide detailed information of flow-induced sound due to the interactions of the blood flow and the heart valve. Applying the proposed hydro-vibroacoustic method for the heart valve analysis involves the following procedure:

- Solving transient CFD
- Saving pressure loads on the surrounding walls
- Mapping frequency domain pressure loading on the walls
- Solve harmonic response of surrounding tissue
- Compute the frequency response of the velocity and acceleration on the epidermal surface

However, there exist challenges in applying the proposed hydro-vibroacoustic method for the sound analysis of the BMHV. Such sound analysis requires a short time step to capture propagating structural waves (wave velocities in vessel wall and tissue layer are 1580 $m.s^{-1}$ and 1720 $m.s^{-1}$,

respectively). Appropriate boundary conditions also need to be considered to avoid incorrect reflections and resonance from the side walls. In addition, non-linearity of the material properties and more realistic geometry of the surrounding tissue have significant roles for accurate results.

The sound generated by a BMHV can be divided into two sources: flow-induced and solid-induced sounds. The flow-induced sound is generated by the interactions of the blood flow with the heart valve leaflets, and the turbulence created downstream of the valve. High-intensity vortical structures can develop high velocity and pressure fluctuations throughout the flow domain and apply forces on the walls. These pressure forces can consequently oscillate the vessel wall and tissue layers and propagate toward the surface. Using the hydro-vibroacoustic method, the propagation of these forces at different frequencies can be mapped on the tissue. Figure 4-6 shows the cross-section of the computational model and stress distibution through the tissue layer.

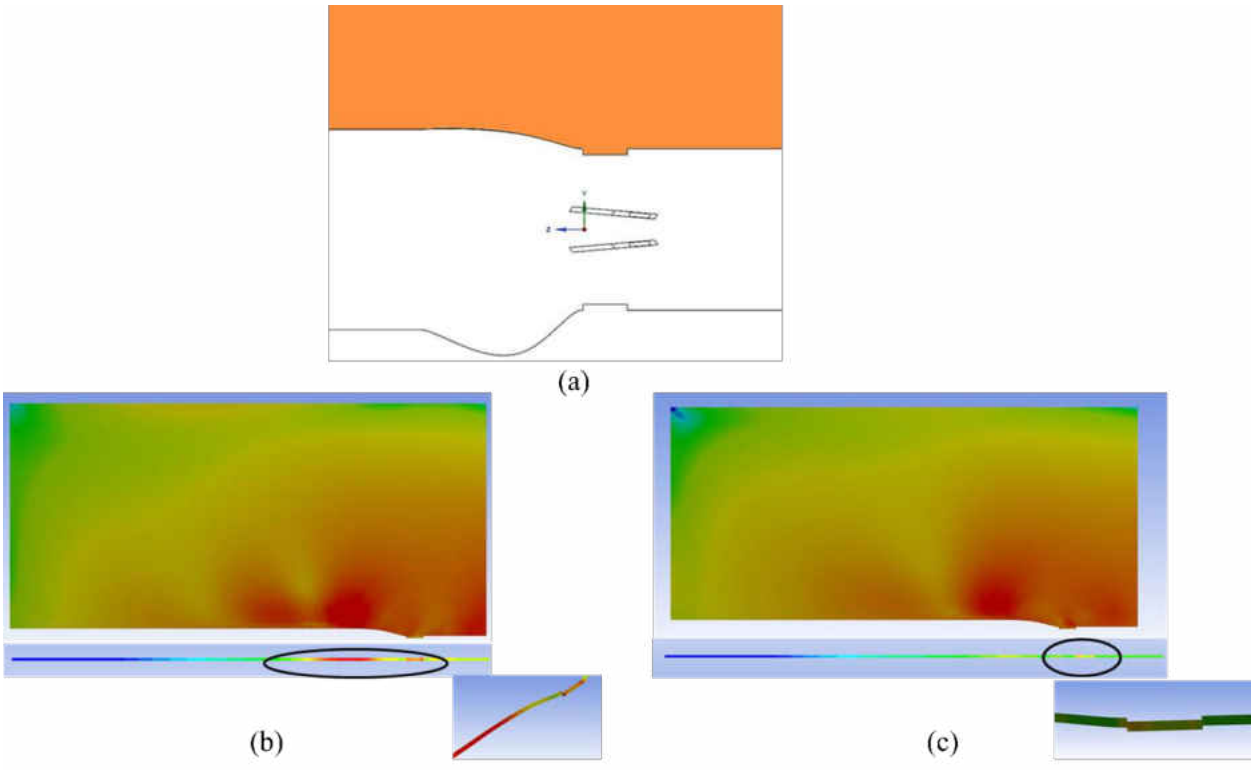

Figure 4-6 (a) Cross-sectional view of the computational model; Mapped pressure forces on the top wall and stress distribution on the tissue at (b) 125 Hz; (c) 250 Hz.

The Solid-induced sound generated by a BMHV can be produced when the two leaflets collide with each other at their leading edges or with the valve housing at their trailing edges. Fluid-structure interaction allows the simulation the heart valve in operation, where the leaflets rotates from fully-open to fully-closed positions. Figure 4-7 shows an example of the stress distribution through the tissue layer at the fuly-closed position where the top leaflet hits the valve housing.

Figure 4-7 Stress distribution through the tissue layer at the fully-closed position where the top leaflet hits the valve housing.

Considering both sound sources along with addressing the challenges dicussed above lead to a more realistic model with accurate results close to what clinicians may hear on skin. This approach can be called virtual phonocardiography.

CHAPTER 5: SUMMARY

The research impact of the current study can be listed as:

- Investigating and comparing different turbulence models suitable for low Mach number internal bounded flows. Accurate modeling of the flow and turbulence leads to detailed information of the flow, especially the fluctuations which are know as flow-induces sound sources.
- Pulsatile pumps allow for a significant amount of studies in the research field of hemodynamics of the heart valves. The goal of this study was to develop a programmable and cost effective pulsatile pump which can produce almost any desired flow waveform.
- Computational fluid dynamics (CFD) analysis of a bileaflet mechanical heart valve, which helps increase the understanding of normal or abnormal valve functions. CFD has a potential to support, enhance and explain clinical observations by providing detailed information of the blood flow. This information might not be easily accessible with in-vivo measurements.
- A new finite element method to investigate the flow-induced sound generation and propagation in a tissue-like material. Advantages of the methods used in the current study include: (a) capability of providing accurate solution with a faster solution time; (b) accurately capturing the break frequency (a frequency at which the spectral curve slope changes, which indicates a drop in flow energy) of the velocity fluctuation measured on epidermal surface; (c) inclusion of the arterial wall elasticity in the analysis (i.e., fluid–structure interaction between blood flow and the arterial wall).

APPENDIX I: PUBLICATIONS

Here is the list of current publications related to the work done by the author (Fardin Khalili) in the biomedical acoustics research lab (BARL) at University of Central Florida (UCF):

- **Khalili, F.**, Mansy, H. A., "Hemodynamics of a bileaflet mechanical heart valve with different levels of dysfunction", J Appl. Biotech & Bioengineer, 2017 [98].
- Gamage, P. P. T., **Khalili, F.**, Azad, MD. Khurshid, Mansy, H. A. "Modeling Inspiratory Flow in a Porcine Lung Airway", Journal of Biomechanical Engineering, Accepted Manuscript, 2017 [186].
- **Khalili, F.**, Gamage, P. P. T., Mansy, H. A., "A coupled CFD-FEA study of sound generated in a stenosed artery and transmitted through tissue layers", IEEE SoutheastCon 2018, St. Petersburg, FL, April 2018 [187].
- **Khalili, F.**, Gamage, P. P. T., Mansy, H. A., "Verification of Turbulence Models for Flow in a Constricted Pipe at Low Reynolds Number", 3rd Thermal and Fluids Engineering Conference (TFEC), Fort Lauderdale, FL, March 2018 [69].
- **Khalili, F.**, Gamage, P. P. T., Mansy, H. A., "Prediction of Turbulent Shear Stresses through Dysfunctional Bileaflet Mechanical Heart Valves using Computational Fluid Dynamics", 3rd Thermal and Fluids Engineering Conference (TFEC), Fort Lauderdale, FL, March 2018 [178].
- **Khalili, F.**, Gamage, P. P. T., Mansy, H. A., "The Influence of the Aortic Root Geometry on Flow Characteristics of a Bileaflet Mechanical Heart Valve", 3rd Thermal and Fluids Engineering Conference (TFEC), Fort Lauderdale, FL, March 2018 [177].
- Gamage, P. P. T., **Khalili, F.**, Mansy, H. A., "Computational Analysis of Inspiratory and Expiratory Flow in the Lung Airway", 3rd Thermal and Fluids Engineering Conference (TFEC), Fort Lauderdale, FL, March 2018 [188].

- Gamage, P. P. T., **Khalili, F.**, Mansy, H. A., "Numerical Modeling of Pulse Wave Propagation in a Stenosed Artery using Two-Way Coupled Fluid Structure Interaction (FSI)", 3rd Thermal and Fluids Engineering Conference (TFEC), Fort Lauderdale, FL, March 2018 [189].
- **Fardin Khalili**, Hansen Mansy, "Blood Flow through a Dysfunctional Mechanical Heart Valve", 38th Annual International Conference IEEE Engineering in Medicine & Biology Society, Orlando, FL, 2016 [190].
- **Fardin Khalili**, Hansen A. Mansy, "Analysis of Pulsatile Blood Flow Through a Bileaflet Mechanical Heart Valve with Moving Leaflets", 2016 Graduate Research Forum, 14th Annual Showcase of Diverse Student Research, University of Central Florida, Orlando, FL, 2016.

APPENDIX II: SIMPLIFIED BERNOULLI EQUATION

A constriction in a tube accelerates fluid which passes through it. This acceleration is called convective, since it is caused by the convection of the fluid from one point in space with one velocity to another point in space with a different velocity. Additional acceleration is caused by changes in blood flow velocity during diastole, especially at the time of heart valve opening and closure. Acceleration of a mass required a force. A small fluid element of volume $\Delta\Psi$ may be regarded as a body with mass $\rho.\Delta\Psi$, where ρ is the density ($1.06 \times 10^3\ kg/m^3$ for blood) of the fluid per unit volume. Acceleration of this element through a stenotic valve is achieved by the pressure drop across the valve. The relation between the pressure drop and the velocity is given by the Bernoulli equation with an added viscous term

$$P_1 - P_2 = \frac{1}{2}\rho(v_2^2 - v_1^2) + \rho\int_1^2 \frac{\overrightarrow{dv}}{dt}\overrightarrow{ds} + R(\vec{v}) \qquad \text{(AI-1)}$$

Where, suffix 1 denotes the position of the fluid element in front of the valve, and suffix 2 in the valve jet; P is the pressure, $\vec{v}$ is the velocity vector of the fluid element along its path, and $\overrightarrow{ds}$ is the path element. The first term of the right-hand side of the equation represents the convective acceleration, the second term represents the acceleration caused by changes of the velocity with time, while the last term represents viscous losses. Estimates of the magnitude of the first and second terms may be given. The atrial velocity, v_1 is ~0.2 m/s. the value of the jet velocity, v_2 will depend on the degree of stenosis, usually being 1-3 m/s. we thus see that $v_2^2 \gg v_1^2$ so that v_1 may be neglected in the convective acceleration term in Eq.1. For the second term we assume that the velocity increases from a zero value in the atrium to the maximum jet velocity v_2 proportionally to the square of the distance. The time dependency of the velocity is assumed to be the same along the whole path of the fluid. This term then takes the form

$$\frac{\rho l}{3}.\frac{dv_2}{dt} \qquad \text{(AI-2)}$$

where, l is the path length of the fluid element from the atrium to the jet. For a stenosis with maximum velocity of 2 m/s, typical values at the valve opening and closure are

$$\frac{dv_2}{dt} = 30 - 40\ m/s^2 \tag{AI-3}$$

$$l = 5 \times 10^{-2}\ m \tag{AI-4}$$

$$\frac{\rho l}{3}.\frac{dv_2}{dt} = 4\ to\ 5\ mmHg \tag{AI-5}$$

We thus see that this term is of the same order as the convective pressure drop during valve opening and closure. When the valve is open; however, $\frac{dv_2}{dt} \sim 1\frac{m}{s^2}$ which gives

$$\frac{\rho l}{3}.\frac{dv_2}{dt} = 0.2\ mmHg \tag{AI-6}$$

Which implies that the convective term dominates the acceleration during diastole. The magnitude of the viscous losses is difficult to estimate. The viscous losses arise from friction between the fluid element and its neighboring fluid, and will thus not only depend on v_2, but on the whole velocity profile. However, the findings suggest that for the fluid element with the maximum velocity in the valve jet, the viscous losses may be neglected. By neglecting the second acceleration term and the viscous losses, the pressure drop can be calculated from v_2 alone. Inserting the value for density in Eq.1, the following simple formula is found

$$P_1 - P_2 = 4v_2^2\ \ mmHg \tag{AI-6}$$

where, v_2 is in units of m/s, while the pressure drop is found in units of mmHg. P_1 is the atrial pressure, and P_2 is the pressure in the jet where v_2 is achieved. P_2 is actually less than the ventricular pressure since a pressure drop working against the flow is needed to retard the large jet velocity to a much smaller ventricular velocity. However, most of the kinetic energy in the jet is lost in turbulence and post-valvular vortices, so that this pressure drop is probably no large.

APPENDIX III: ARDUINO CODE

Here is programming code for the Arduino to control the linear actuator including the comment which explain the operation of each part of the code:

```
int Relay1 = 5;              // Assign relay1 to output port 5 of the Arduino
int Relay2 = 6;              // Define relay2 to output port 6 of the Arduino
int Relay3 = 9;              // Define relay3 to output port 9 of the Arduino
int Relay4 = 10;             // Define relay4 to output port 10 of the Arduino

void setup () {

  Serial.begin(9600); // Data rate in bits per second (baud) for serial data transmission for communicating with the computer

}

void loop() {

//Backward movement of the actuator; only Relay1 and Relay2 are activated which create reverse positive-negative circuit for the backward movement.

digitalWrite(Relay1, HIGH);
digitalWrite(Relay2, HIGH);
digitalWrite(Relay3, LOW);
digitalWrite(Relay4, LOW);
delay(280);

//Stop time of the actuator; all port are deactivated
digitalWrite(Relay1, LOW);
digitalWrite(Relay2, LOW);
digitalWrite(Relay3, LOW);
digitalWrite(Relay4, LOW);
delay(240);

for (int i=0; i<=67;i++){
// Forward movement of the actuator; only Relay3 and Relay3 are activated which create right positive-negative circuit for the backward movement.

digitalWrite(Relay1, LOW);
digitalWrite(Relay2, LOW);
digitalWrite(Relay3, HIGH);
digitalWrite(Relay4, HIGH);
delay(2);
digitalWrite(Relay1, LOW);
digitalWrite(Relay2, LOW);
digitalWrite(Relay3, LOW);
```

```
digitalWrite(Relay4, LOW);
delay(1);
}

for (int j=0; j<=30;j++){
// Forward movement of the actuator; only Relay3 and Relay3 are activated which create right positive-negative circuit for the backward movement.

digitalWrite(Relay1, LOW);
digitalWrite(Relay2, LOW);
digitalWrite(Relay3, HIGH);
digitalWrite(Relay4, HIGH);
delay(1);
digitalWrite(Relay1, LOW);
digitalWrite(Relay2, LOW);
digitalWrite(Relay3, LOW);
digitalWrite(Relay4, LOW);
delay(1);
}
```

REFERENCES

[1] WHO, 2017, “Fact Sheet: Cardiovascular Diseases (CVDs).,” World Heal. Organ., (May) [Online]. Available: http://www.who.int/mediacentre/factsheets/fs317/en/.

[2] Mohammadi, H., Jahandardoost, M., and Fradet, G., 2015, “Elliptic St. Jude Bileaflet Mechanical Heart Valves,” Cardiovasc. Syst., 3(1), p. 1.

[3] Smadi, O., Hassan, I., Pibarot, P., and Kadem, L., 2010, “Numerical and Experimental Investigations of Pulsatile Blood Flow Pattern through a Dysfunctional Mechanical Heart Valve,” J. Biomech., 43(8), pp. 1565–1572.

[4] Spühler, J. H., 2017, “Patient-Specific Finite Element Modeling of the Blood Flow in the Left Ventricle of a Human Heart,” KTH Royal Institute of Technology.

[5] Hufnagel, C. A., 1951, “Aortic Plastic Valvular Prosthesis.,” Bull. Georgetown Univ. Med. Cent., 4(5), pp. 128–130.

[6] DeWall, R. A., Qasim, N., and Carr, L., 2000, “Evolution of Mechanical Heart Valves,” Ann. Thorac. Surg., 69(5), pp. 1612–1621.

[7] Emery, R. W., and Nicoloff, D. M., 1979, “St. Jude Medical Cardiac Valve Prosthesis: In Vitro Studies.,” J. Thorac. Cardiovasc. Surg., 78(2), pp. 269–276.

[8] Gott, V. L., Alejo, D. E., and Cameron, D. E., 2003, “Mechanical Heart Valves: 50 Years of Evolution,” Ann Thorac Surg, 76, pp. 2230–9.

[9] Emery, R. W., Krogh, C. C., Arom, K. V, Emery, A. M., Benyo-Albrecht, K., Joyce, L. D., and Nicoloff, D. M., 2005, “The St. Jude Medical Cardiac Valve Prosthesis: A 25-Year Experience with Single Valve Replacement.,” Ann. Thorac. Surg., 79(3), pp. 776-82–3.

[10] Fatemi, R., and Chandran, K. B., 1989, “An in Vitro Comparative Study of St. Jude Medical and Edwards-Duromedics Bileaflet Valves Using Laser Anemometry.,” J. Biomech. Eng., 111(4), pp. 298–302.

[11] Dasi, L. P., Simon, H. A., Sucosky, P., and Yoganathan, A. P., 2009, “Fluid Mechanics of Artificial Heart Valves,” Clin. Exp. Pharmacol. Physiol., 36(2), pp. 225–237.

[12] Nobili, M., Morbiducci, U., Ponzini, R., Del Gaudio, C., Balducci, A., Grigioni, M., Maria Montevecchi, F., and Redaelli, A., 2008, “Numerical Simulation of the Dynamics of a Bileaflet Prosthetic Heart Valve Using a Fluid-Structure Interaction Approach,” J. Biomech., 41(11), pp. 2539–2550.

[13] Woo, Y.-R., and Yoganathan, A. P., 1986, “In Vitro Pulsatile Flow Velocity and Shear Stress Measurements in the Vicinity of Mechanical Mitral Heart Valve Prostheses,” J. Biomech., 19(1), pp. 39–51.

[14] Hasenkam, J. M., 1990, “Studies of Velocity Fields and Turbulence Downstream of Aortic Valve Prostheses in Vitro and in Vivo.,” Dan. Med. Bull., 37(3), p. 235.

[15] Min Yun, B., Aidun, C. K., and Yoganathan, A. P., 2014, “Blood Damage Through a

Bileaflet Mechanical Heart Valve: A Quantitative Computational Study Using a Multiscale Suspension Flow Solver," J. Biomech. Eng., 136(10), p. 101009.

[16] Dumont, K., Vierendeels, J., Kaminsky, R., Van Nooten, G., Verdonck, P., and Bluestein, D., 2007, "Comparison of the Hemodynamic and Thrombogenic Performance of Two Bileaflet Mechanical Heart Valves Using a CFD/FSI Model," J. Biomech. Eng., 129(4), pp. 558–565.

[17] Bottio, T., Caprili, L., Casarotto, D., and Gerosa, G., 2004, "Small Aortic Annulus: The Hydrodynamic Performances of 5 Commercially Available Bileaflet Mechanical Valves," J. Thorac. Cardiovasc. Surg., 128(3), pp. 457–462.

[18] Shipkowitz, T., Ambrus, J., Kurk, J., and Wickramasinghe, K., 2002, "Evaluation Technique for Bileaflet Mechanical Valves.," J. Heart Valve Dis., 11(2), pp. 275–82.

[19] Borazjani, I., Ge, L., and Sotiropoulos, F., 2008, "Curvilinear Immersed Boundary Method for Simulating Fluid Structure Interaction with Complex 3D Rigid Bodies," J. Comput. Phys., 227(16), pp. 7587–7620.

[20] King, M. J., David, T., and Fisher, J., 1997, "Three-Dimensional Study of the Effect of Two Leaflet Opening Angles on the Time-Dependent Flow through a Bileaflet Mechanical Heart Valve," Med. Eng. Phys., 19(3), pp. 235–241.

[21] King, M. J., David, T., and Fisher, J., 1994, "An Initial Parametric Study on Fluid Flow through Bileaflet Mechanical Heart Valves Using Computational Fluid Dynamics," Proc. Inst. Mech. Eng. Part H J. Eng. Med., 208(2), pp. 63–72.

[22] Shipkowitz, T., Ambrus, J., Kurk, J., and Wickramasinghe, K., 2002, "Evaluation Technique for Bileaflet Mechanical Valves.," J. Heart Valve Dis., 11(2), pp. 275–82.

[23] Bluestein, D., Einav, S., and Hwang, N. H. C., 1994, "A Squeeze Flow Phenomenon at the Closing of a Bileaflet Mechanical Heart Valve Prosthesis," J. Biomech., 27(11), pp. 1369–1378.

[24] Hanle, D. D., Harrison, E. C., Yoganathan, A. P., Allen, D. T., and Corcoran, W. H., 1989, "In Vitro Flow Dynamics of Four Prosthetic Aortic Valves: A Comparative Analysis," J. Biomech., 22(6–7), pp. 597–607.

[25] Walker, D. K., Brendzel, A. M., and Scotten, L. N., 1999, "The New St. Jude Medical Regent Mechanical Heart Valve: Laboratory Measurements of Hydrodynamic Performance.," J. Heart Valve Dis., 8(6), pp. 687–696.

[26] Chambers, J., and Ely, J. L., 1998, "Early Postoperative Echocardiographic Hemodynamic Performance of the On-X Prosthetic Heart Valve: A Multicenter Study.," J. Heart Valve Dis., 7(5), pp. 569–573.

[27] Lim, W. L., Chew, Y. T., Chew, T. C., and Low, H. T., 1998, "Steady Flow Dynamics of Prosthetic Aortic Heart Valves: A Comparative Evaluation with PIV Techniques," J. Biomech., 31(5), pp. 411–421.

[28] Chew, Y. T., Low, H. T., Lee, C. N., and Kwa, S. S., 1993, "Laser Anemometry Measurements of Steady Flow Past Aortic Valve Prostheses," J Biomech Eng, 115(3), pp. 290–298.

[29] Healy, T. M., Fontaine, a. a., Ellis, J. T., Walton, S. P., and Yoganathan, a. P., 1998, "Visualization of the Hinge Flow in a 5:1 Scaled Model of the Medtronic Parallel Bileaflet Heart Valve Prosthesis," Exp. Fluids, 25(5–6), pp. 512–518.

[30] Emery, R. W., Mettler, E., and Nicoloff, D. M., 1979, "A New Cardiac Prosthesis: The St. Jude Medical Cardiac Valve: In Vivo Results," Circulation, 60(2 Pt 2), pp. 48–54.

[31] Shahriari, S., Maleki, H., Hassan, I., and Kadem, L., 2012, "Evaluation of Shear Stress Accumulation on Blood Components in Normal and Dysfunctional Bileaflet Mechanical Heart Valves Using Smoothed Particle Hydrodynamics," J. Biomech., 45(15), pp. 2637–2644.

[32] Deviri, E., Sareli, P., Wisenbaugh, T., and Cronje, S. L., 1991, "Obstruction of Mechanical Heart Valve Prostheses: Clinical Aspects and Surgical Management.," J. Am. Coll. Cardiol., 17(3), pp. 646–50.

[33] Ellis, J. T., Travis, B. R., and Yoganathan, A. P., 2000, "An In Vitro Study of the Hinge and Near-Field Forward Flow Dynamics of the St. Jude Medical® Regent™ Bileaflet Mechanical Heart Valve," Ann. Biomed. Eng., 28(5), pp. 524–532.

[34] Klusak, E., Bellofiore, A., Loughnane, S., and Quinlan, N. J., 2015, "High-Resolution Measurements of Velocity and Shear Stress in Leakage Jets From Bileaflet Mechanical Heart Valve Hinge Models.," J. Biomech. Eng., 137(11), p. 111008.

[35] Min Yun, B., Aidun, C. K., and Yoganathan, A. P., 2014, "Blood Damage Through a Bileaflet Mechanical Heart Valve: A Quantitative Computational Study Using a Multiscale Suspension Flow Solver," J. Biomech. Eng., 136(10), p. 101009.

[36] Hung, T. C., Hochmuth, R. M., Joist, J. H., and Sutera, S. P., 1976, "Shear-Induced Aggregation and Lysis of Platelets," ASAIO J., 22(1), pp. 285–290.

[37] Bruss, K. H., Reul, H., Van Gilse, J., and Knott, E., 1983, "Pressure Drop and Velocity Fields at Four Mechanical Heart Valve Prostheses," Life Support Syst., 1, pp. 3–22.

[38] Sutera, S. P., and Mehrjardi, M. H., 1975, "Deformation and Fragmentation of Human Red Blood Cells in Turbulent Shear Flow," Biophys. J., 15(1), pp. 1–10.

[39] Mohandas, N., Hochmuth, R. M., and Spaeth, E. E., 1974, "Adhesion of Red Cells to Foreign Surfaces in the Presence of Flow," J. Biomed. Mater. Res., 8(2), pp. 119–136.

[40] Blackshear, P. L., 1972, "Hemolysis at Prosthetic Surfaces," Chem. biosurfaces, 2, pp. 523–561.

[41] Sallam, a M., and Hwang, N. H., 1984, "Human Red Blood Cell Hemolysis in a Turbulent Shear Flow: Contribution of Reynolds Shear Stresses.," Biorheology, 21(6), pp. 783–797.

[42] Lu, P. C., Lai, H. C., and Liu, J. S., 2001, "A Reevaluation and Discussion on the Threshold Limit for Hemolysis in a Turbulent Shear Flow," J. Biomech., 34(10), pp. 1361–1364.

[43] Woo, Y.-R., and Yoganathan, A. P., 1986, "In Vitro Pulsatile Flow Velocity and Shear Stress Measurements in the Vicinity of Mechanical Mitral Heart Valve Prostheses," J. Biomech., 19(1), pp. 39–51.

[44] Baumgartner, H., Schima, H., Tulzer, G., and Kühn, P., 1993, "Effect of Stenosis Geometry

on the Doppler-Catheter Gradient Relation in Vitro: A Manifestation of Pressure Recovery," J. Am. Coll. Cardiol., 21(4), pp. 1018–1025.

[45] McQueen, D. M., and Peskin, C. S., 1985, "Computer-Assisted Design of Butterfly Bileaflet Valves for the Mitral Position.," Scand. J. Thorac. Cardiovasc. Surg., 19(2), pp. 139–148.

[46] De Vita, F., de Tullio, M. D., and Verzicco, R., 2016, "Numerical Simulation of the Non-Newtonian Blood Flow through a Mechanical Aortic Valve: Non-Newtonian Blood Flow in the Aortic Root," Theor. Comput. Fluid Dyn., 30(1–2), pp. 129–138.

[47] Barannyk, O., and Oshkai, P., 2015, "The Influence of the Aortic Root Geometry on Flow Characteristics of a Prosthetic Heart Valve," J. Biomech. Eng., 137(5), p. 51005.

[48] Taebi, A., and Mansy, H. A., 2017, "Time-Frequency Distribution of Seismocardiographic Signals: A Comparative Study," Bioengineering, 4(2), p. 32.

[49] Taebi, A., Solar, B. E., and Mansy, H. A., 2018, "An Adaptive Feature Extraction Algorithm for Classification of Seismocardiographic Signals," SoutheastCon 2018, IEEE, IEEE, pp. 1–5.

[50] Klepetko, W., Moritz, A., Mlczoch, J., Schurawitzki, H., Domanig, E., and Wolner, E., 1989, "Leaflet Fracture in Edwards-Duromedics Bileaflet Valves.," J. Thorac. Cardiovasc. Surg., 97(1), pp. 90–94.

[51] Dimitri, W. R., and Williams, B. T., 1990, "Fracture of the Duromedics Mitral Valve Housing with Leaflet Escape.," J. Cardiovasc. Surg. (Torino)., 31(1), pp. 41–46.

[52] Kafesjian, R., Howanec, M., Ward, G. D., Diep, L., Wagstaff, L. S., and Rhee, R., 1994, "Cavitation Damage of Pyrolytic Carbon in Mechanical Heart Valves.," J. Heart Valve Dis., 3 Suppl 1, pp. S2-7.

[53] Deviri, E., Sareli, P., Wisenbaugh, T., and Cronje, S. L., 1991, "Obstruction of Mechanical Heart Valve Prostheses: Clinical Aspects and Surgical Management.," J. Am. Coll. Cardiol., 17(3), pp. 646–50.

[54] Pibarot, P., and Dumesnil, J. G., 2009, "Prosthetic Heart Valves: Selection of the Optimal Prosthesis and Long-Term Management," Circulation, 119(7), pp. 1034–1048.

[55] Vesey, J. M., and Otto, C. M., 2004, "Complications of Prosthetic Heart Valves," Curr.Cardiol.Rep., 6, pp. 106–111.

[56] Montorsi, P., Cavoretto, D., Alimento, M., Muratori, M., and Pepi, M., 2003, "Prosthetic Mitral Valve Thrombosis: Can Fluoroscopy Predict the Efficacy of Thrombolytic Treatment?," Circulation, 108, p. II79-II84.

[57] Fernandes, V., Olmos, L., Nagueh, S. F., Quiñones, M. A., and Zoghbi, W. A., 2002, "Peak Early Diastolic Velocity rather than Pressure Half-Time Is the Best Index of Mechanical Prosthetic Mitral Valve Function," Am. J. Cardiol., 89(6), pp. 704–710.

[58] Taebi, A., and Mansy, H. A., 2017, "Noise Cancellation from Vibrocardiographic Signals Based on the Ensemble Empirical Mode Decomposition," J. Biotechnol. Bioeng., 2(2), p. 24.

[59] Taebi, A., and Mansy, H. A., 2017, "Grouping Similar Seismocardiographic Signals Using

Respiratory Information," Signal Processing in Medicine and Biology Symposium (SPMB), 2017 IEEE, IEEE, Philadelphia, PA, pp. 1–6.

[60] Taebi, A., and Mansy, H. A., 2017, "Analysis of Seismocardiographic Signals Using Polynomial Chirplet Transform and Smoothed Pseudo Wigner-Ville Distribution," Signal Processing in Medicine and Biology Symposium (SPMB), 2017 IEEE, IEEE, Philadelphia, PA, pp. 1–6.

[61] Ask, P., Hök, B., Loyd, D., and Teriö, H., 1995, "Bio-Acoustic Signals from Stenotic Tube Flow: State of the Art and Perspectives for Future Methodological Development," Med. Biol. Eng. Comput., 33(5), pp. 669–675.

[62] Thompson, W. R., Hayek, C. S., Tuchinda, C., Telford, J. K., and Lombardo, J. S., 2001, "Automated Cardiac Auscultation for Detection of Pathologic Heart Murmurs," Pediatr. Cardiol., 22(5), pp. 373–379.

[63] Hanna, I. R., and Silverman, M. E., 2002, "A History of Cardiac Auscultation and Some of Its Contributors," Am. J. Cardiol., 90(3), pp. 259–267.

[64] Wen, Y. N., Lee, A. P. W., Fang, F., Jin, C. N., and Yu, C. M., 2014, "Beyond Auscultation: Acoustic Cardiography in Clinical Practice," Int. J. Cardiol., 172(3), pp. 548–560.

[65] Bruns, D. L., 1959, "A General Theory of the Causes of Murmurs in the Cardiovascular System," Am. J. Med., 27(3), pp. 360–374.

[66] Lees, R. S., and Dewey, C. F., 1970, "Phonoangiography: A New Noninvasive Diagnostic Method for Studying Arterial Disease.," Proc. Natl. Acad. Sci. U. S. A., 67(2), pp. 935–942.

[67] Mckusick, V. A., 1959, "Cardiovascular Sound in Health and Disease," Am. J. Med. Sci., 238(1), p. 128.

[68] Seo, J. H., Bakhshaee, H., Garreau, G., Zhu, C., Andreou, A., Thompson, W. R., and Mittal, R., 2017, "A Method for the Computational Modeling of the Physics of Heart Murmurs," J. Comput. Phys., 336.

[69] Khalili, F., Gamage, P. P. T., and Mansy, H. A., 2018, "Verification of Turbulence Models for Flow in a Constricted Pipe at Low Reynolds Number," 3rd Thermal and Fluids Engineering Conference (TFEC), pp. 1–10.

[70] Ahmed, S. A., and Giddens, D. P., 1983, "Flow Disturbance Measurements through a Constricted Tube at Moderate Reynolds Numbers," J. Biomech., 16(12), pp. 955–963.

[71] Kirkeeide, R. L., Young, D. F., and Cholvin, N. R., 1977, "Wall Vibrations Induced by Flow through Simulated Stenoses in Models and Arteries," J. Biomech., 10(7).

[72] Jones, S. A., and Fronek, A., 1987, "Analysis of Break Frequencies Downstream of a Constriction in a Cylindrical Tube," J. Biomech., 20(3), pp. 319–327.

[73] Yazicioglu, Y., Royston, T. J., Spohnholtz, T., Martin, B., Loth, F., and Bassiouny, H. S., 2005, "Acoustic Radiation from a Fluid-Filled, Subsurface Vascular Tube with Internal Turbulent Flow due to a Constriction," J. Acoust. Soc. Am., 118(2), pp. 1193–1209.

[74] Ozer, M. B., Acikgoz, S., Royston, T. J., Mansy, H. A., and Sandler, R. H., 2007, "Boundary Element Model for Simulating Sound Propagation and Source Localization within the

Lungs," J. Acoust. Soc. Am., 122(1), pp. 657–671.

[75] Colonius, T., and Lele, S. K., 2004, "Computational Aeroacoustics: Progress on Nonlinear Problems of Sound Generation," Prog. Aerosp. Sci., 40(6), pp. 345–416.

[76] Bailly, C., Bogey, C., and Marsden, O., 2011, "Progress in Direct Noise Computation," Noise Notes, 9(3), pp. 31–48.

[77] Seo, J. H., Moon, Y. J., and Shin, B. R., 2008, "Prediction of Cavitating Flow Noise by Direct Numerical Simulation," J. Comput. Phys., 227(13), pp. 6511–6531.

[78] Seo, J. H., and Lele, S. K., 2009, "Numerical Investigation of Cloud Cavitaiton and Cavitation Noise on a Hydrofoil Section," Proc. 7th Int. Symp. Cavitation.

[79] Duncan, G. W., Gruber, J. O., Dewey Jr, C. F., Myers, G. S., and Lees, R. S., 1975, "Evaluation of Carotid Stenosis by Phonoangiography," N. Engl. J. Med., 293(22), pp. 1124–1128.

[80] Fredberg, J. J., 1977, "Origin and Character of Vascular Murmurs: Model Studies," J. Acoust. Soc. Am., 61(4), pp. 1077–1085.

[81] Wang, J.-Z., Tie, B., Welkowitz, W., Semmlow, J. L., and Kostis, J. B., 1990, "Modeling Sound Generation in Stenosed Coronary Arteries," IEEE Trans. Biomed. Eng., 37(11), pp. 1087–1094.

[82] Borisyuk, A. O., 2003, "Model Study of Noise Field in the Human Chest due to Turbulent Flow in a Larger Blood Vessel," J. Fluids Struct., 17(8), pp. 1095–1110.

[83] Seo, J. H., and Mittal, R., 2012, "A Coupled Flow-Acoustic Computational Study of Bruits from a Modeled Stenosed Artery," Med. Biol. Eng. Comput., 50(10), pp. 1025–1035.

[84] Zhu, C., Seo, J.-H., Bakhshaee, H., and Mittal, R., 2017, "A Computational Method for Analyzing the Biomechanics of Arterial Bruits," J. Biomech. Eng., 139(5), p. 51008.

[85] Zhu, C., Seo, J.-H., and Mittal, R., 2017, "Hemodynamics of Aortic Stenosis and Implications for Non-Invasive Diagnosis via Auscultation," Bull. Am. Phys. Soc., 62.

[86] Fontaine, A. A., Ellis, J. T., Healy, T. M., Hopmeyer, J., and Yoganathan, A. P., 1996, "Identification of Peak Stresses in Cardiac Prostheses. A Comparison of Two-Dimensional versus Three-Dimensional Principal Stress Analyses," ASAIO J., 42(3), pp. 154–163.

[87] Dasi, L. P., Ge, L., Simon, A. H., Sotiropoulos, F., and Yoganathan, P. A., 2007, "Vorticity Dynamics of a Bileaflet Mechanical Heart Valve in an Axisymmetric Aorta," Phys. Fluids, 19(6).

[88] Bluestein, D., Rambod, E., and Gharib, M., 2000, "Vortex Shedding as a Mechanism for Free Emboli Formation in Mechanical Heart Valves.," J. Biomech. Eng., 122(2), pp. 125–134.

[89] Ge, L., Dasi, L. P., Sotiropoulos, F., and Yoganathan, A. P., 2008, "Characterization of Hemodynamic Forces Induced by Mechanical Heart Valves: Reynolds vs. Viscous Stresses," Ann. Biomed. Eng., 36(2), pp. 276–297.

[90] Smadi, O., Fenech, M., Hassan, I., and Kadem, L., 2009, "Flow through a Defective

Mechanical Heart Valve: A Steady Flow Analysis," Med. Eng. Phys., 31(3), pp. 295–305.

[91] Barannyk, O., and Oshkai, P., 2015, "The Influence of the Aortic Root Geometry on Flow Characteristics of a Prosthetic Heart Valve," J. Biomech. Eng., 137(5), p. 51005.

[92] Inc. ANSYS, 2017, "ANSYS FLUENT Theory Guide," Release 18.2.

[93] Jones, W. P., and Launder, B., 1973, "The Calculation of Low-Reynolds-Number Phenomena with a Two-Equation Model of Turbulence," Int. J. Heat Mass Transf., 16(6), pp. 1119–1130.

[94] Khalili, F., Majumdar, P., and Zeyghami, M., 2015, "Far-Field Noise Prediction of Wind Turbines at Different Receivers and Wind Speeds: A Computational Study," ASME International Mechanical Engineering Congress and Exposition, Proceedings (IMECE).

[95] Solari, G., and Piccardo, G., 2001, "Probabilistic 3-D Turbulence Modeling for Gust Buffeting of Structures," Probabilistic Eng. Mech., 16(1), pp. 73–86.

[96] Behzadmehr, A., Saffar-Avval, M., and Galanis, N., 2007, "Prediction of Turbulent Forced Convection of a Nanofluid in a Tube with Uniform Heat Flux Using a Two Phase Approach," Int. J. Heat Fluid Flow, 28(2), pp. 211–219.

[97] Khalili, F., and Mansy, H. A., 2016, "Blood Flow through a Dysfunctional Mechanical Heart Valve," 38th Annual International Conference of the IEEE Engineering in Medicine and Biology Societ, Orlando, USA.

[98] Khalili, F., Gamage, P. P. T., and Mansy, H. A., 2017, "Hemodynamics of a Bileaflet Mechanical Heart Valve with Different Levels of Dysfunction," J. Appl. Biotechnol. Bioeng., 2(5).

[99] Lin, C. L., Tawhai, M. H., McLennan, G., and Hoffman, E. A., 2007, "Characteristics of the Turbulent Laryngeal Jet and Its Effect on Airflow in the Human Intra-Thoracic Airways," Respir. Physiol. Neurobiol., 157(2–3), pp. 295–309.

[100] Hoffman Ruddy, B., Nadun Kuruppumullage, D., Carnaby, G., Crary, M., Lehman, J., and Ilegbusi, O. J., 2017, "Computational Modelling of Cough Function and Airway Penetrant Behavior in Patients with Disorders of Laryngeal Function," Laryngoscope Investig. Otolaryngol., 2(1), pp. 23–29.

[101] GAMAGE, P. T., 2017, "MODELING OF FLOW GENERATED SOUND IN A CONSTRICTED DUCT AT LOW MACH NUMBER," University of Central Florida Orlando, Florida.

[102] Khalili, F., 2014, Three-Dimensional CFD Simulation and Aeroacoustics Analysis of Wind Turbines, Northern Illinois University.

[103] Nicoud, F., and Ducros, F., 1999, "Subgrid-Scale Stress Modelling Based on the Square of the Velocity Gradient Tensor," Flow, Turbul. Combust., 62(3), pp. 183–200.

[104] Thibotuwawa, P. G., Khalili, F., Azad, M., and Mansy, H., 2017, "Modeling Inspiratory Flow in a Porcine Lung Airway.," J. Biomech. Eng.

[105] Taebi, A., and Mansy, H. A., 2016, "Effect of Noise on Time-Frequency Analysis of Vibrocardiographic Signals," J. Bioeng. Biomed. Sci., 6(202), p. 2.

[106] Taebi, A., and Mansy, H. A., 2015, "Time-Frequency Analysis of Vibrocardiographic Signals," 2015 BMES Annu. Meet., 60, p. 3229.

[107] Johnson, D. A., Menter, F. R., and Rumsey, C. L., 1994, "The Status of Turbulence Modeling for Aerodynamics," AIAA Pap., 2226.

[108] Menter, F., and Kuntz, M., 2004, "Adaptation of Eddy-Viscosity Turbulence Models to Un-Steady Separated Flow behind Vehicles," Aerodyn. Heavy Veh. Truck. Buses, Trains, pp. 339–352.

[109] Menter, F. R., Kutz, M., and Kuntz, M., 2002, "Adaptation of Eddy-Viscosity Turbulence Models to Unsteady Separated Flow Behind Vehicles," United Eng. Found. Conf. Aerodyn. Heavy Veh. Truck. Buses Trains, 2002, pp. 339–352.

[110] Shur, M., Spalart, P. R., Strelets, M., and Travin, A., 1999, "Detached-Eddy Simulation of an Airfoil at High Angle of Attack," Eng. Turbul. Model. Exp., 4, pp. 669–678.

[111] Spalart, P. R., Deck, S., Shur, M. L., Squires, K. D., Strelets, M. K., and Travin, A., 2006, "A New Version of Detached-Eddy Simulation, Resistant to Ambiguous Grid Densities," Theor. Comput. Fluid Dyn., 20(3), pp. 181–195.

[112] Lighthill, M. J., 1952, "On Sound Generated Aerodynamically I. General Theory," Proc. R. Soc. Lond. A, 211(1107), pp. 564–587.

[113] Boussinesq, J., 1877, Essai Sur La Théorie Des Eaux Courantes, Impr. nationale.

[114] Wilcox, D. C., 1998, Turbulence Modeling for CFD (Second Edition).

[115] Wilcox, D. C., 2008, "Formulation of the K-W Turbulence Model Revisited," AIAA J., 46(11), pp. 2823–2838.

[116] Huang, P. G., Bradshaw, P., and Coakley, T. J., 1992, "Assessment of Closure Coefficients for Compressible-Flow Turbulence Models," Nasa Tech. Memo., (October 1992).

[117] Menter, F. R., 1992, "Improved Two-Equation K-Omega Turbulence Models for Aerodynamic Flows," NASA Tech. Memo., (103978), pp. 1–31.

[118] Menter, F. R., 1994, "Two-Equation Eddy-Viscosity Turbulence Models for Engineering Applications," AIAA J., 32(8), pp. 1598–1605.

[119] Daly, B. J., 1970, "Transport Equations in Turbulence," Phys. Fluids, 13(11), p. 2634.

[120] Gibson, M. M., and Launder, B. E., 1978, "Ground Effects on Pressure Fluctuations in the Atmospheric Boundary Layer," J. Fluid Mech., 86(3), pp. 491–511.

[121] Chou, P. Y., 1945, "ON VELOCITY CORRELATIONS AND THE SOLUTIONS OF THE EQUATIONS OF TURBULENT FLUCTUATION*," Quart. Appl. Math., 3, pp. 38–54.

[122] Speziale, C. G., Sarkar, S., and Gatski, T. B., 1991, "Modelling the Pressure Strain Correlation of Turbulence: An Invariant Dynamical Systems Approach," J. Fluid Mech., 227, pp. 245–272.

[123] Lien, F. S., and Leschziner, M. A., 1994, "Assessment of Turbulence-Transport Models Including Non-Linear Rng Eddy-Viscosity Formulation and Second-Moment Closure for Flow over a Backward-Facing Step," Comput. Fluids, 23(8), pp. 983–1004.

[124] Launder, B. E., and Shima, N., 1989, "Second-Moment Closure for the near-Wall Sublayer. Development and Application," AIAA J., 27(10), pp. 1319–1325.

[125] Frisch, U., 1995, Turbulence: The Legacy of AN Kolmogorov, Cambridge university press.

[126] Kolmogorov, A. N., 1941, "The Local Structure of Turbulence in Incompressible Viscous Fluid for Very Large Reynolds Numbers," Dokl. Akad. Nauk SSSR, pp. 299–303.

[127] Kolmogorov, A. N., 1941, "Dissipation of Energy in Locally Isotropic Turbulence," Dokl. Akad. Nauk SSSR, pp. 16–18.

[128] Chapelier, J. B., Wasistho, B., and Scalo, C., 2018, "A Coherent Vorticity Preserving Eddy-Viscosity Correction for Large-Eddy Simulation," J. Comput. Phys., 359, pp. 164–182.

[129] Smagorinsky, J., 1963, "General Circulation Experiments Wiht the Primitive Equations I. The Basic Experiment," Mon. Weather Rev., 91(3), pp. 99–164.

[130] SCHLICHTING, H., and GERSTEN, K., 2000, "Boundary-Layer Theory."

[131] Balaras, E., and Benocci, C., 1994, In Application of Direct and Large Eddy Simulation to Transition and Turbulence.

[132] Khalili, F., De Paoli, F., and Guldiken, R., 2015, "Impact Resistance of Liquid Body Armor Utilizing Shear Thickening Fluids: A Computational Study," Volume 7B: Fluids Engineering Systems and Technologies, p. V07BT09A029.

[133] Spalart, P. R., Jou, W. H., Strelets, M., Allmaras, S. R., and others, 1997, "Comments on the Feasibility of LES for Wings, and on a Hybrid RANS/LES Approach," Adv. DNS/LES, 1, pp. 4–8.

[134] Mockett, C., 2009, "A Comprehensive Study of Detached-Eddy Simulation," PhD Thesis TU Berlin.

[135] Spalart, R., 2001, "Young-Person's Guide Simulation Grids Detached-Eddy," NASA Tech. Note, 211032(July), pp. 1003–1008.

[136] Morton, S., Forsythe, J., Mitchell, A., and Hajek, D., 2002, "Detached-Eddy Simulations and Reynolds-Averaged Navier-Stokes Simulations of Delta Wing Vortical Flowfields," J. Fluids Eng., 124(4), pp. 924–932.

[137] Spalart, P. R., 2000, "Strategies for Turbulence Modelling and Simulations," International Journal of Heat and Fluid Flow, pp. 252–263.

[138] Ahmed, S. A., 1998, "An Experimental Investigation of Pulsatile Flow through a Smooth Constriction," Exp. Therm. Fluid Sci., 17(4), pp. 309–318.

[139] RHIE, C. M., and CHOW, W. L., 1983, "Numerical Study of the Turbulent Flow Past an Airfoil with Trailing Edge Separation," AIAA J., 21(11), pp. 1525–1532.

[140] Salim, S. M., and Cheah, S. C., 2009, "Wall Y + Strategy for Dealing with Wall-Bounded Turbulent Flows," Int. MultiConference Eng. Comput. Sci., II, pp. 1–6.

[141] Ariff, M., Salim, S. M., and Cheah, S. C., 2009, "Wall Y + Approach for Dealing With Turbulent Flow Over a Surface Mounted Cube : Part 1 – Low Reynolds Number," Seventh Int. Conf. CFD Miner. Process Ind. CSIRO, (December), pp. 1–6.

[142] Ariff, M., Salim, S. M., and Cheah, S. C., 2009, "Wall Y + Approach for Dealing With Turbulent Flow Over a Surface Mounted Cube : Part 2 – High Reynolds Number," Seventh Int. Conf. CFD Miner. Process Ind. Process Ind., (December), pp. 1–6.

[143] 2017, "Laser Doppler Anemometry Measurement Principles," Dantec Dyn. A/S [Online]. Available: https://www.dantecdynamics.com/measurement-principles-of-lda.

[144] Borisyuk, A. O., 2010, "Experimental Study of Wall Pressure Fluctuations in Rigid and Elastic Pipes behind an Axisymmetric Narrowing," J. Fluids Struct., 26(4), pp. 658–674.

[145] Houser, S., Okafor, I., Raghav, V., and Yoganathan, A., 2018, "Flow Visualization of the Non-Parallel Jet-Vortex Interaction," J. Vis., pp. 1–10.

[146] Saaid, H., Segers, P., Novara, M., Claessens, T., and Verdonck, P., 2018, "Single Calibration Multiplane Stereo-PIV: The Effect of Mitral Valve Orientation on Three-Dimensional Flow in a Left Ventricle Model," Exp. Fluids, 59(3).

[147] Skoczyńska, A., Wojakowska, A., Nowacki, D., Bobak, Ł., Turczyn, B., Smyk, B., Szuba, A., and Trziszka, T., 2015, "Unsaturated Fatty Acids Supplementation Reduces Blood Lead Level in Rats," Biomed Res. Int., 2015.

[148] Wegener, J. W., Loga, F., Stegner, D., Nieswandt, B., and Hofmann, F., 2014, "Phospholipase D1 Is Involved in α1-Adrenergic Contraction of Murine Vascular Smooth Muscle," FASEB J., 28(3), pp. 1044–1048.

[149] Schweighöfer, H., Rummel, C., Mayer, K., and Rosengarten, B., 2014, "Brain Function in iNOS Knock out or iNOS Inhibited (L-NIL) Mice under Endotoxic Shock," Intensive Care Med. Exp., 2(1), p. 24.

[150] 2018, "PA-15 LINEAR ACTUATOR," Progress. Autom. Inc.

[151] Serata, S., 1979, "Borehole Stress Property Measuring System."

[152] Roeck, W. De, 2007, Hybrid Methodologies for the Computational Aeroacoustics Analysis of Confined Subsonic Flows.

[153] Simon, H. A., Leo, H. L., Carberry, J., and Yognathan, A. P., 2004, "Comparison of the Hinge Flow Fields of Two Bileaflet Mechanical Heart Valves under Aortic and Mitral Conditions," Ann. Biomed. Eng., 32(12), pp. 1607–1617.

[154] Gross, J. M., Shu, M. C. S., Dai, F. F., Ellis, J., and Yoganathan, A. P., 1996, "A Microstructural Flow Analysis within a Bileaflet Mechanical Heart Valve Hinge.," J. Heart Valve Dis., 5(6), pp. 581–90.

[155] Ellis, J. T., Healy, T. M., Fontaine, A. A., Weston, M. W., Jarret, C. A., Saxena, R., and Yoganathan, A. P., 1996, "An in Vitro Investigation of the Retrograde Flow Fields of Two Bileaflet Mechanical Heart Valves.," J. Heart Valve Dis., 5(6), pp. 600–606.

[156] Vallana, F., Rinaldi, S., Galletti, P. M., Nguyen, A., and Piwnica, A., 1992, "Pivot Design in Bileaflet Valves," ASAIO J., 38(3), pp. M600-6.

[157] Ellis, J. T., Travis, B. R., and Yoganathan, A. P., 2000, "An In Vitro Study of the Hinge and Near-Field Forward Flow Dynamics of the St. Jude Medical® Regent™ Bileaflet Mechanical Heart Valve," Ann. Biomed. Eng., 28(5), pp. 524–532.

[158] Grigioni, M., Daniele, C., D'Avenio, G., and Barbaro, V., 2001, "The Influence of the Leaflets' Curvature on the Flow Field in Two Bileaflet Prosthetic Heart Valves," J. Biomech., 34(5), pp. 613–621.

[159] Lloyd-Jones, D., Adams, R. J., Brown, T. M., Carnethon, M., Dai, S., De Simone, G., Ferguson, T. B., Ford, E., Furie, K., Gillespie, C., Go, A., Greenlund, K., Haase, N., Hailpern, S., Ho, P. M., Howard, V., Kissela, B., Kittner, S., Lackland, D., Lisabeth, L., Marelli, A., McDermott, M. M., Meigs, J., Mozaffarian, D., Mussolino, M., Nichol, G., Roger, V. L., Rosamond, W., Sacco, R., Sorlie, P., Stafford, R., Thom, T., Wasserthiel-Smoller, S., Wong, N. D., and Wylie-Rosett, J., 2010, "Heart Disease and Stroke Statistics-2010 Update: A Report from the American Heart Association," Circulation, 121(7), pp. e46–e215.

[160] McDonald, D. A., 1974, "Blood Flow in Arteries."

[161] Yoganathan, A. P., He, Z., and Casey Jones, S., 2004, "Fluid Mechanics of Heart Valves," Annu. Rev. Biomed. Eng., 6(1), pp. 331–362.

[162] Nestola, M. G. C., Faggiano, E., Vergara, C., Lancellotti, R. M., Ippolito, S., Antona, C., Filippi, S., Quarteroni, A., and Scrofani, R., 2017, "Computational Comparison of Aortic Root Stresses in Presence of Stentless and Stented Aortic Valve Bio-Prostheses," Comput. Methods Biomech. Biomed. Engin., 20(2), pp. 171–181.

[163] Iung, B., Baron, G., Butchart, E. G., Delahaye, F., Gohlke-Bärwolf, C., Levang, O. W., Tornos, P., Vanoverschelde, J. L., Vermeer, F., Boersma, E., Ravaud, P., and Vahanian, A., 2003, "A Prospective Survey of Patients with Valvular Heart Disease in Europe: The Euro Heart Survey on Valvular Heart Disease," Eur. Heart J., 24(13), pp. 1231–1243.

[164] Taebi, A., and Mansy, H. A., 2016, "Time-Frequency Description of Vibrocardiographic Signals," 38th Annual International Conference of the IEEE Engineering in Medicine and Biology Society, Orlando, FL.

[165] Taebi, A., and Mansy, H. A., 2015, "Time-Frequency Analysis of Vibrocardiographic Signals," 2015 BMES Annual Meeting.

[166] Taebi, A., and Mansy, H. A., 2017, "Noise Cancellation from Vibrocardiographic Signals Based on the Ensemble Empirical Mode Decomposition," J. Appl. Biotechnol. Bioeng., 2(2), p. 24.

[167] Bahlmann, E., Nienaber, C. A., Cramariuc, D., Gohlke-Baerwolf, C., Ray, S., Devereux, R. B., Wachtell, K., Kuck, K. H., Davidsen, E., and Gerdts, E., 2011, "Aortic Root Geometry in Aortic Stenosis Patients (a SEAS Substudy)," Eur. J. Echocardiogr., 12(8), pp. 585–590.

[168] Underwood, M. J., Khoury, G. El, Deronck, D., Glineur, D., and Dion, R., 2000, "The Aortic Root: Structure, Function, and Surgical Reconstruction," Heart, 83, pp. 376–380.

[169] Nistri, S., Basso, C., Marzari, C., Mormino, P., and Thiene, G., 2005, "Frequency of Bicuspid Aortic Valve in Young Male Conscripts by Echocardiogram," Am. J. Cardiol., 96(5), pp. 718–721.

[170] Schoen, F. J., and Levy, R. J., 2005, "Calcification of Tissue Heart Valve Substitutes: Progress toward Understanding and Prevention," Ann. Thorac. Surg., 79(3), pp. 1072–1080.

[171] Oechtering, T. H., Frydrychowicz, A., and Sievers, H. H., 2017, "Malrotated Sinus Vortices in Straight Graft Valve-Sparing Aortic Root Treatment: A Matter of Concern?," J. Thorac. Cardiovasc. Surg., 154(3), pp. 794–797.

[172] Jahandardoost, M., Fradet, G., and Mohammadi, H., 2016, "Hemodynamic Study of the Elliptic St. Jude Medical Valve: A Computational Study," Proc. Inst. Mech. Eng. Part H J. Eng. Med., 230(2), pp. 85–96.

[173] Chandran, K. B., and Yearwood, T. L., 1981, "Experimental Study of Physiological Pulsatile Flow in a Curved Tube," J. Fluid Mech., 111, pp. 59–85.

[174] Reul, H., Vahlbruch, A., Giersiepen, M., Schmitz-Rode, T., Hirtz, V., and Effert, S., 1990, "The Geometry of the Aortic Root in Health, at Valve Disease and after Valve Replacement," J. Biomech., 23(2).

[175] Yen, J. H., Chen, S. F., Chern, M. K., and Lu, P. C., 2014, "The Effect of Turbulent Viscous Shear Stress on Red Blood Cell Hemolysis," J. Artif. Organs, 17(2), pp. 178–185.

[176] Hellmeier, F., Nordmeyer, S., Yevtushenko, P., Bruening, J., Berger, F., Kuehne, T., Goubergrits, L., and Kelm, M., 2017, "Hemodynamic Evaluation of a Biological and Mechanical Aortic Valve Prosthesis Using Patient-Specific MRI-Based CFD," Artif. Organs.

[177] Khalili, F., Gamage, P. P. T., and Mansy, H. A., 2018, "The Influence of the Aortic Root Geometry on Flow Characteristics of a Bileaflet Mechanical Heart Valve," 3rd Therm. Fluids Eng. Conf.

[178] Khalili, F., Gamage, P. P. T., and Mansy, H. A., 2018, "Prediction of Turbulent Shear Stresses through Dysfunctional Bileaflet Mechanical Heart Valves Using Computational Fluid Dynamics," 3rd Thermal and Fluids Engineering Conference (TFEC), Fort Lauderdale, FL, USA, pp. 1–9.

[179] Taebi, A., Bomar, A. J., Sandler, R. H., and Mansy, H. A., 2018, "Heart Rate Monitoring During Different Lung Volume Phases Using Seismocardiography," SoutheastCon 2018, IEEE, IEEE, pp. 1–5.

[180] Solar, B. E., Taebi, A., and Mansy, H. A., 2017, "Classification of Seismocardiographic Cycles into Lung Volume Phases," Signal Processing in Medicine and Biology Symposium (SPMB), 2017 IEEE, IEEE, Philadelphia, PA, pp. 1–2.

[181] Taebi, A., Sandler, R. H., Kakavand, B., and Mansy, H. A., 2017, "Seismocardiographic Signal Timing with Myocardial Strain," Signal Processing in Medicine and Biology Symposium (SPMB), 2017 IEEE, IEEE, Philadelphia, PA, pp. 1–2.

[182] Varghese, S. S., Frankel, S. H., and Fischer, P. F., 2007, "Direct Numerical Simulation of Stenotic Flows. Part 2. Pulsatile Flow," J. Fluid Mech., 582, pp. 281–318.

[183] Varghese, S. S., Frankel, S. H., and Fischer, P. F., 2007, "Direct Numerical Simulation of Stenotic Flows. Part 1. Steady Flow," J. Fluid Mech., 582, pp. 253–280.

[184] Mittal, R., Simmons, S. P., and Najjar, F., 2003, "Numerical Study of Pulsatile Flow in a Constricted Channel," J. Fluid Mech., (485), pp. 337–378.

[185] Miller, A., Lees, R. S., Kistler, J. P., and Abbott, W., 1980, “Effects of Surrounding Tissue on the Sound Spectrum of Arterial Bruits in Vivo,” Stroke, 11(4), pp. 394–398.

[186] Gamage, P. P. T., Khalili, F., Azad, M. D. K., and Mansy, H. A., 2017, “Modeling Inspiratory Flow in a Porcine Lung Airway,” J. Biomech. Eng.

[187] Khalili, F., Gamage, P. P. T., and Mansy, H. A., 2018, “A Coupled CFD-FEA Study of Sound Generated in a Stenosed Artery and Transmitted through Tissue Layers,” IEEE SoutheastCon 2018, IEEE, St. Petersburg.

[188] Gamage, P. P. T., Khalili, F., Azad, M. K., and Mansy, H. A., 2018, “Computational Analysis of Inspiratory and Expiratory Flow in the Lung Airway,” 3rd Thermal and Fluids Engineering Conference (TFEC), Fort Lauderdale.

[189] Gamage, P. P. T., Khalili, F., and Mansy, H. A., 2018, “Numerical Modeling of Pulse Wave Propagation in a Stenosed Artery Using Two-Way Coupled Fluid Structure Interaction (FSI),” 3rd Thermal and Fluids Engineering Conference (TFEC), Fort Lauderdale, FL, USA.

[190] Khalili, F., and Mansy, H. A., 2016, “Blood Flow through a Dysfunctional Mechanical Heart Valve,” 38th Annual International Conference of the IEEE Engineering in Medicine and Biology Societ, Orlando, USA.